Chaotic Modeling and Simulation (CMSIM) 1: 3–18, 2013

Evidence of chaos in the Belief Propagation for LDPC codes

Jean-Christophe Sibel[1], Sylvain Reynal[2], and David Declercq[2]

[1] INRIA / ETIS / ENSEA / Univ. of Cergy-Pontoise / CNRS UMR 8051, 95014 Cergy-Pontoise, France
(E-mail: jean-christophe.sibel@ensea.fr)
[2] ETIS / ENSEA / Univ. of Cergy-Pontoise / CNRS UMR 8051, 95014 Cergy-Pontoise, France
(E-mail: reynal@ensea.fr)
[3] ETIS / ENSEA / Univ. of Cergy-Pontoise / CNRS UMR 8051, 95014 Cergy-Pontoise, France
(E-mail: declercq@ensea.fr)

Abstract. In this paper, we investigate the behaviors of the Belief Propagation algorithm considered as a dynamic system. In the context of LDPC (Low Density Parity-Check) codes, we use the noise power of the transmission channel as a potentiometer to evaluate the different motions that the BP can follow. The computations of dynamic quantifiers as the bifurcation diagram, the Lyapunov exponent and the reconstructed trajectory enable to bring out four main behaviors. In addition, we propose a novel measure that is the hyperspheres method, which provides the knowledge of the time evolution of the attractor size. The information collected from these different quantifiers helps to better understand the BP evolution and to focus on the noise power values for which the BP suffers from chaos.
Keywords: LDPC, iterative map, chaos, Lyapunov exponent, bifurcation diagram.

1 Introduction

The channel coding is a research field whose purpose is to protect an information to transmit from environmental disturbances. The first step is the encoding of the information, a procedure in which the information, modeled as a sequence of k bits $u_1, \ldots, u_k$, is mapped to a larger sequence of N bits $x_1, \ldots, x_N$. The map consists in artificial correlations called constraints or parity-check equations. In [1] are introduced the Low-Density Parity-Check (LDPC) codes which are a widespread technique to encode the information. Such a code can be represented by a Tanner graph [2], a graphical representation which turns out to be very useful in the second step, the decoding. In this part, the bits transmitted though a random noisy channel are iteratively handled by a decoding algorithm to create an associated output sequence of

Reviced: 29 November 2012 / Accepted: 20 January 2013

ISSN 2241-0503

N bits that verify the whole set of parity-check equations and that must be as close as possible to the input sequence. One of the most famous decoding algorithm is the Belief Propagation (BP) [3] used to solve inference in graphical models. Extensively studied in [5,6], it is deemed to be the optimal message-passing algorithm in the case the Tanner graph of the LDPC code is loopfree. However, in most cases the Tanner graph is not loopfree [7] that involves that the BP becomes suboptimal. Moreover, the BP presents some complex behaviors in terms of the noise power of the transmitted channel, as periodic and chaotic motions [9]. Along the whole paper, we present some measures to bring out these different behaviors. The paper is organized as follows: in the second section are presented preliminaries about the LDPC codes and the BP, in the third section we present the dynamic environment of the BP, the measures to identify the behaviors and the associated results.

2 Preliminaries

2.1 Graphical Model – LDPC codes

We consider a set of N hidden binary random variables $\mathbf{X} = \{X_1, \ldots, X_N\}$ whose global state is denoted by $\mathbf{x} = [x_1, \ldots, x_N]$. To each variable X_i is associated an observation y_i that provides a prior information on the state of X_i given that the a posteriori distribution on X_i is proportional to the likelihood:

$$p(x_i|y_i) \propto p(y_i|x_i)$$

In the digital communications area, the hidden variables play the role of bits to transmit through a noisy channel, the observations represent the data collected at the output at the channel. These data are used to compute $\hat{\mathbf{x}} = [\hat{x}_1, \ldots, \hat{x}_N]$ the estimate of the input sequence $\mathbf{x}$, as it is shown on the figure 1.

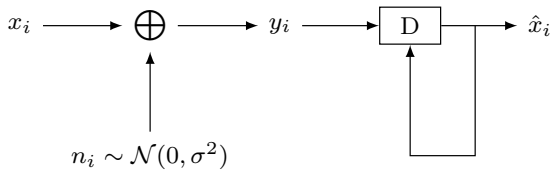

Fig. 1. Digital communication pattern: the channel is an additive Gaussian channel of power σ^2, D is the esttimation block that provides $\hat{\mathbf{x}}$

To ensure reliable communications is included the use of an LDPC code. An LDPC code is built by a set of M constraints $\mathbf{C} = \{C_1, \ldots, C_M\}$ usually called parity-check equations. The value of the constraint C_j is computed by the set of variables mapped by C_j, namely its neighborhood $\mathcal{N}_j$ such that:

$$c_j = \sum_{X_i \in \mathcal{N}_j} x_i$$

where the sum is computed over the Galois field GF(2). The variables and the parity-check equations are respectiveley associated to the variable nodes and the check nodes of the graphical representation of the LDPC code, called the Tanner graph $\mathbf{G} = (\mathbf{X} \cup \mathbf{C}, \{e_{ij}\})$. The check node C_j and the variable node X_i are linked by an edge e_{ij} if $X_i \in \mathcal{N}_j$. We define the neighborhood $\mathcal{N}_i$ of the variable node X_i as the set of check nodes that map X_i. An example of a Tanner graph is displayed on the figure 2.

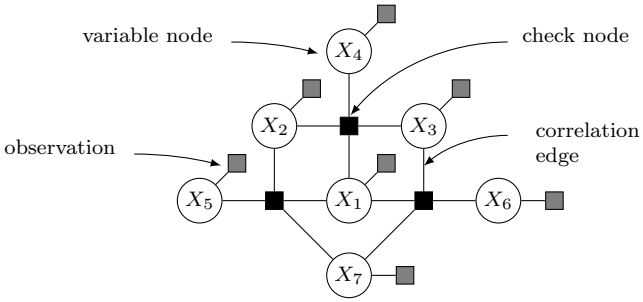

Fig. 2. Tanner graph of the Hamming code ($N = 7$)

2.2 Message-passing

The BP is an algorithm that helps to solve inference in graphical models. More accurately, it provides estimates $\{b_i(x_i)\}_i$ of the posterior marginal distributions of the variables, called beliefs. From these trial distributions can be extracted an estimate of $\mathbf{x}$ such that:

$$\hat{\mathbf{x}} = \bigcup_{i=1}^{N} \arg\max_{x_i} b_i(x_i)$$

To obtain the beliefs, the BP passes messages iteratively between the variable nodes and the check nodes, according to their neighborhood dependence. An edge e_{ij} carries two different messages, each oriented in a specific way:

- the message from C_j to X_i is: $n_{ji}^{(k)}(x_i) = f_{ji}(\{m_{xy}^{(k-1)}\}_{(x,y)})$
- the message from C_i to C_j is: $m_{ij}^{(k)}(x_i) = g_{ij}(\{n_{yx}^{(k)}\}_{(x,y)}, l_i(x_i))$

where f_{ij} and g_{ji} are update functions whose expressions are detailed in [2], and $l_i(x_i)$ is the likelihood computed from the observation y_i. To give an idea of the analytic expressions of these functions, a message from a node A to a node B, whatever their nature, is somehow the geometric average of the messages incoming on A. The output of the BP is a set of beliefs that are computed from the same principle [2]: $b_i(x_i)$ is someway the geometric average of the messages incoming on the variable node X_i in the state x_i.

2.3 Topological troubles

The BP has been introduced by Pearl [3] as an algorithm to solve inference on trees and polytrees. For such graphical model, this algorithm is surely optimal. Though, the most of the LDPC codes have basically non tree-like topology, their Tanner graphs are full of loopy structures. This drawback is unavoidable because the check nodes need to be interwoven to make the LDPC code robust against the channel noise. Accordingly, the BP turns out to be suboptimal in most cases. In [7] and [8] the BP is investigated to bring out some convergence conditions depending on the topology of the Tanner graph, it was found that short loops are the most harmful and that the convergence of the BP must be unreachable if the LDPC code contains at least two loops. This conclusion brings the fact that mots LDPC codes cannot been decoded perfectly by the BP. As a result are shown on the figure 3 two Bit Error Rates (BER) according to the Signal-to-Noise Ratio (SNR) on loopy codes of the same length N: one contains only large loops and the other only short loops.

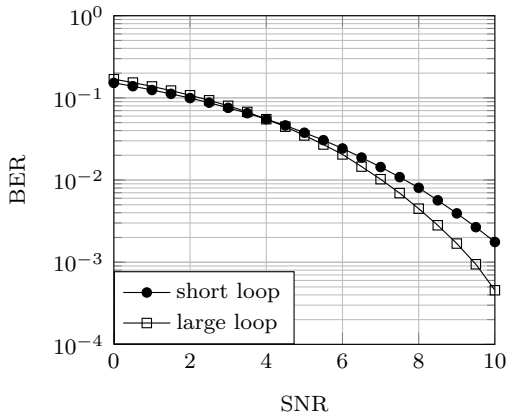

Fig. 3. BER of the BP – Difference between short loops and large loops

The BER of the code with large loops is less damaged than the one wih short loops, that confirms the previous conclusion. This can be easily understood given that the BP is a message-passing algorithm: short loops have short term effects because only a small number of iterations is necessary to develop their harmful effect, contrary to the large loops.

Despite the practical interest of such an estimator, the BER does not bring the whole information about the behavior of the BP in case of loopy LDPC codes. On the figure 4 is displayed the evolution of the BER along the iterations according to four SNR values given a particular noise realization on the Tanner code [10] of length $N = 155$. It appears obvious that the BP suffers from great divergence depending on the SNR. The rationale behind these results is that the BP does not behave trivially as it could be wrongly thought given the BER.

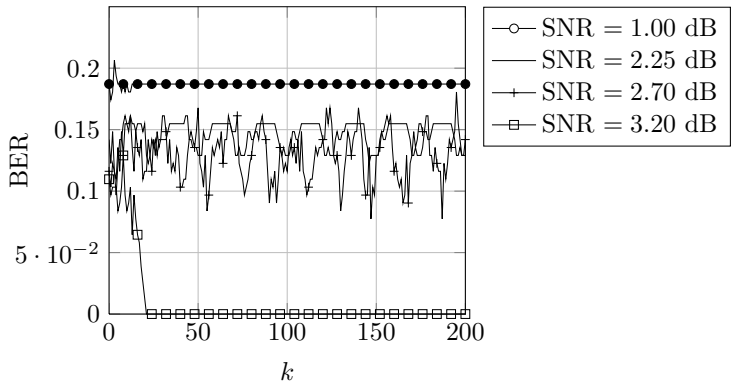

Fig. 4. BER of the BP on the Tanner code for four SNR values

In other terms, the SNR plays the role of a parameter that wields great influence on the behavior of the BP. Therefore, it appears necessary to investigate the BP as a dynamical system, a work presented in the next section.

3 Dynamics

In this section is presented an experimental study that brings out the dynamics of the BP algorithm according to the evolution of the SNR. To this end is introduced a toolbox including four estimators, each one carrying relevant information on the system. For each of them is presented the computation method, then a few results and finally the properties it reveals concerning the BP. The goal is to get information about:

- the SNR values that correspond to blatant changes in the behavior of the BP,
- the description of the different attractors the BP encounters,
- the size of these attractors.

Introducing the term attractor implies the definition of a state space. In the current study, such a space is built in such a way that each message n_{ji} defines a state variable. However, such a state space is of very high number of dimensions, given that a Tanner graph in practice could contain tens of thousands edges. Fortunately, experiments show that it is quite equivalent to consider the beliefs as pseudo-state variables, reducing dramatically the number of dimensions. Finally, in the following, all estimators are measured in the pseudo-state space such that each state variable is associated to a unique belief.

3.1 Bifurcation diagram

First of all, it appears necessary to go a little more deeply in the study of the figure 4. One would note that the BERs suffer from a threshold phenomenon,

especially for SNR = 2.25 dB. This is actually an unfortunate consequence of the decoding process D, see figure 1, that thresholds the beliefs such that:

$$\forall X_i \in \mathbf{X}, \quad b_i(x_i) \in [0,1] \longmapsto \hat{x}_i \in \{0,1\}$$

To extract relevant information concerning the BP, it is recommended to consider estimators that faithfully render the conduct of the BP. To this end, it appears well suited to replace the BER by a smoother function, namely the mean square beliefs introduced in [9]:

$$\forall k \in \{1,\dots,K\}, \quad E(k) = \sqrt{\frac{1}{N}\sum_{i=1}^{N}\left(b_i^{(k)}(x_i)\right)^2} \tag{1}$$

where the values $\{x_i\}_i$ are assumed to be the right ones and K is an arbitrary number of iterations. Its properties are partly equivalent to the BER ones in the sense that:

- $E(k) = 1$: the BP has perfectly decoded,
- $E(k) = 0.25$: the BP does not provide any relevant knowledge on the variables,
- $E(k) = 0$: the BP completely failed.

Experiments show that $E(k)$ lives between the two first situations, furthermore its evolution along the iterations is indeed softer than the BER, see figure 5.

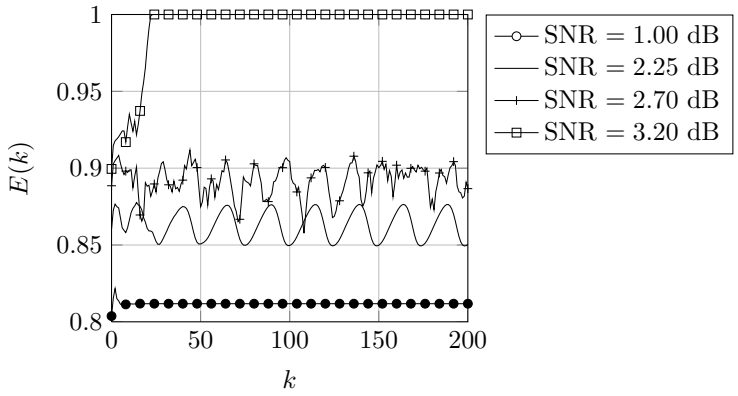

Fig. 5. Mean square beliefs of the BP on the Tanner code for four SNR values

On this figure appears the strong dependency of the BP dynamics on the SNR, the algorithm does not converge for all values. It is either stuck in steady states for SNR $\in \{1.00 \text{ dB}, 3.20 \text{ dB}\}$ or divergent for SNR $\in \{2.25 \text{ dB}, 2.92 \text{ dB}\}$. To draw an evolution of the mean square beliefs according to the SNR comes out the use of the bifurcation diagram. Instead of displaying the whole evolution of $E(k)$ along the iterations we only pick up its final value $E(K)$. Theoretically, in [9], at K the BP is expected to have reached a steady state. In practice, as

shown by the figure 5, it is absolutely not systematic. For computation time's sake, the steady state is redefined as the permanent evolution after an arbitrary number of iterations. On the figure 6 are displayed the bfurcation diagrams of the BP for four noise realizations that we call Error Events (EE).

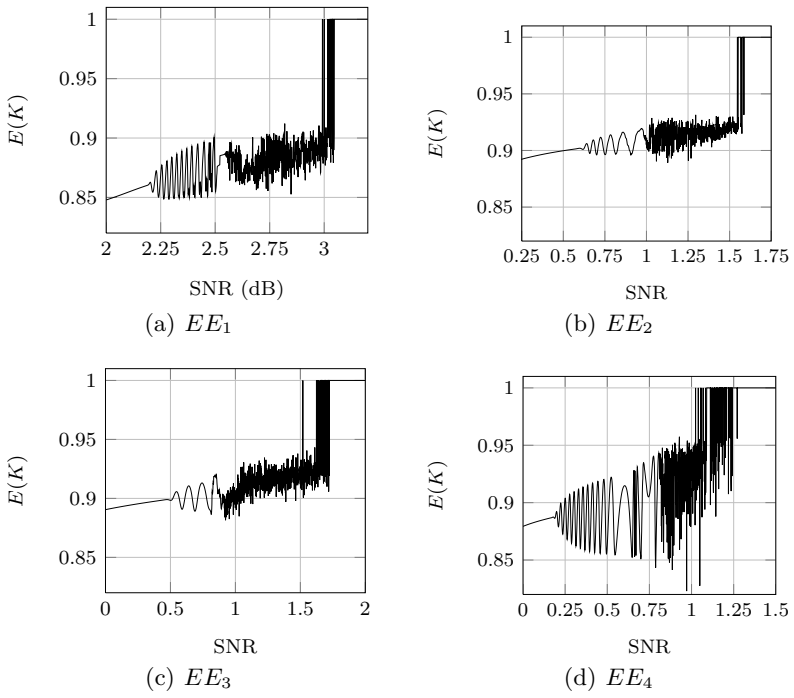

Fig. 6. Bifurcation diagrams of the BP

The bifurcation diagrams reveal critical SNR values that blatantly change the BP conduct. It appears five particular behaviors of $E(K)$:

- (B1) smooth increasing,
- (B2) oscillations,
- (B3) erratic evolution,
- (B4) convergence jumps,
- (B5) convergence.

At this point appears a clue about the chaotic behavior of the BP (B3), even though are needed other observations to confirm it. Despite the order pattern is common to the error events, the critical SNR values are not the same. Actually it is strongly possible that most noise realizations lead to quite similar SNR critical values, the current difference we observe should correspond to the variance of the estimator, given that the number of simulations is quite small. A suited method to solve this problem would consist in average on a set of numerous noise realizations to obtain a mean bifurcation diagram with relevant

variance. However, it appears quite impossible to conduct such a process. The reason comes out of the efficiency of the BP in terms of error correction, the error events that lead to non trivial behaviors of the BP along the SNR corresponds to rare events. Other regular error events imply very fast convergence of the BP to the perfect estimate. On the figure 7 is displayed the BER of the Tanner code decoded by the BP.

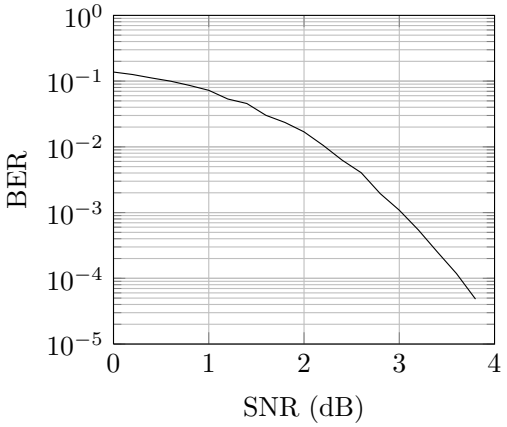

Fig. 7. BER of the Tanner code decoded by the BP

This figure makes appear that around SNR = 2.50 dB, for example, only one error event among a thousand will lead to wrong decoding by the BP, making the average computation of the bifurcation diagram quite untractable. Despite this drawback, a very important point raised up from extensive and numerous experiments is that the order of the five behaviors brought out previously is always the same, whatever the error event provided that it implies non trivial behaviors, and whatever the LDPC code. Therfore it is also always possible to extract four critical SNR values that share the whole range in five intervals corresponding with the behaviors B1, B2, B3, B4 and B5.

3.2 Lyapunov exponents

Given the critical SNR values, the next step is to find out the kind of the behaviors that were brought out, even though a few clues are given by the bifurcation diagram. To this end, we investigate the sensitivity of the BP to very small changes in the initial conditions, *i.e.* the likelihoods, by the use of the famous Lyapunov exponent. The computation of this estimator is made according to the method exposed in [12,11]. First of all we evaluate at each iteration $k \leq K$ the Euclidean distance d_k between two initially close trajectories. Then we estimate the Lypaunov exponent λ as the slope of the least square regression line of $\ln d_k$ along the iterations. Actually this method comes from the observation that for strongly divergent behavior, d_k follows an exponential law whose parameter is λ, as we can see on the figure 8.

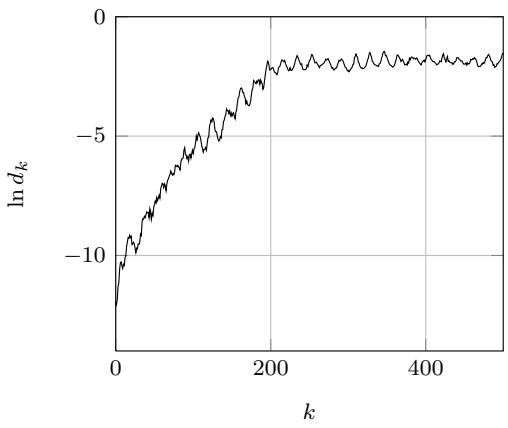

Fig. 8. Evolution of the log-distance between initially close trajectories for the BP, SNR = 2.90 dB, EE_1. The evolution is exponential in $k \in [0, 200]$. For $k \geq 200$ appears a stair due to the compacity of the state space.

On the figure 9 are displayed the Lyapunov exponents averages around the four error events introduced previously according to the Euclidean distance. The sign of λ reveals the behavior of the system around the corresponding initialization of the trajectories: $\lambda \geq 0$ means the trajectories have moved away one from the other, which is an evidence of a chaotic behavior,$\lambda \leq 0$ means the trajectories have got closer, which is an evidence of a convergent behavior to a small sized volume of the state space. This volume is reduced to a fixed point if and only if $\lambda \to \infty$. When λ crosses the x-axis the system suffers from a bifurcation meaning that the algorithm has changed of conduct, as it was observed about the bifurcation diagram. To each SNR interval we obtain conclusions from λ:

- (B1) $\lambda = 0$: the trajectories are quite close but never merge
- (B2) $\lambda = \text{cst} > 0$: the trajectories are moving away at a constant rate
- (B3) $\lambda > 0, \lambda \neq \text{cst}$: erratic evolutions of the trajectories, evidence of chaos
- (B4) λ getting lower: the trajectories begin to move closer
- (B5) $\lambda \to -\infty$: the trajectories merge

It is commonly accepted that the Lyapunov exponent provides a reliable signature of the behavior of any dynamical system. Therefore we can assert that the BP encounters chaos in the SNR interval B3 that is not of neglectible length. In addition, it appears that this chaos appears and disappears quite suddenly in terms of the SNR, looking at the slope of λ. It means that practically we can easily define a chaotic interval of the SNR for any LDPC code.

3.3 Reduced trajectory

The previous estimators revealed properties of the BP according to the SNR. A convenient approach to enforce these observations is to visualize the dynamical system in its state space.

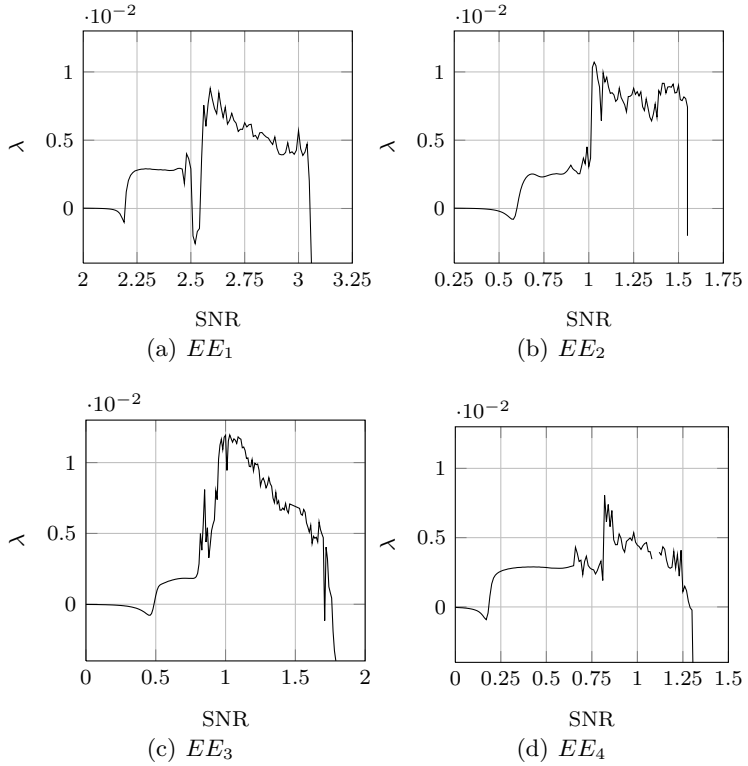

Fig. 9. Lyapunov exponents of the BP on the Tanner code

However, our human skills prevent us from directly observing a system whose number of dimensions is several hundreds or even thousands, that is the case currently. To circumvent this undesired problem, we define a reduced 3-dimensional pseudo-state space and then a reduced pseudo-trajectory. To this end we make use of the state space reconstruction [11]. It consists in constructing a state space of arbitrary number of dimensions given a one dimensional map computed from the state variables. In this investigation, a known map of such property is the mean square beliefs. Firstly, the method aims to compute $E(k)$ at each iteration k to get a sequence $\mathbf{E} = [E(k)]_{0 \leq k \leq K}$. Secondly we map this one dimensional sequence to a three dimensional sequence:

$$\mathbf{E} \longmapsto \tilde{\mathbf{E}} = \begin{bmatrix} E(0) & E(1) & E(2) \\ \vdots & \vdots & \vdots \\ E(K-2) & E(K-1) & E(K) \end{bmatrix}$$

On the figure 10 are displayed a few reduced trajectories of the BP for typical values of the SNR deduced from the previous bifurcation diagram. On the first figure is exhibited at SNR = 2.10 dB a convergence of the trajectory toward a small size attractor, as it was expected according to the corresponding λ.

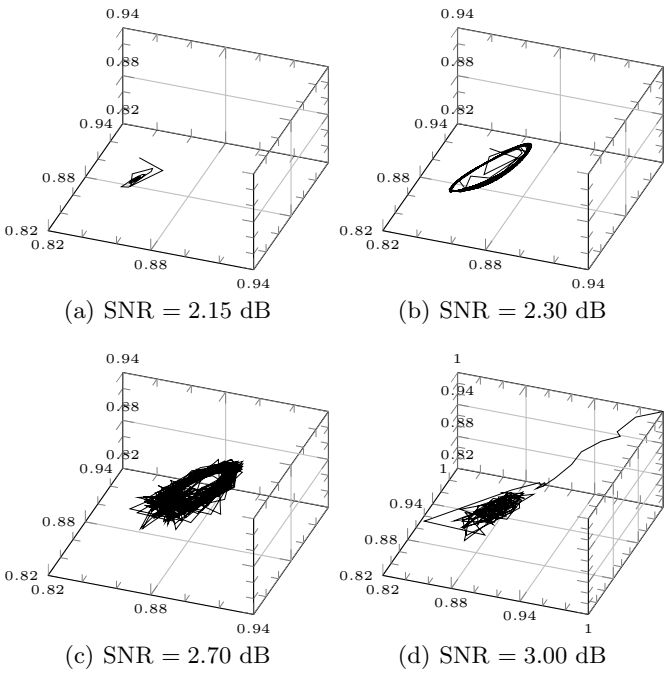

Fig. 10. Reduced trajectories for the BP on the Tanner code for the error event EE_1

By increasing the SNR between 2.19 dB and 2.49 dB the trajectory transforms to a limit cycle. The thickness of the trajectory along this limit cycle increases as the SNR is getting greater up to 2.50 dB. At the same time this limit cycle interleaves with other limit cycles, the BP encounters a sequence of period doubling bifurcations, displayed on the figure 11 with two interleft cycles.

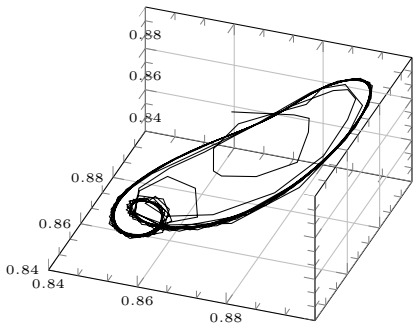

Fig. 11. Reduced trajectory for the BP on the Tanner code with SNR = 2.40 dB

Such a phenomenon is a typical route to chaos [11], a behavior observable from SNR = 2.51 dB. There is not any periodic evolution or fixed point convergence anymore, as it is displayed for 2.70 dB. When the SNR reaches 2.99 dB the

trajectory collapses to a single point, meaning that the BP has correctly converged. Such behaviors are similar to the results of other experiments led on other error events, that enforces the common dynamics between different noise realizations.

3.4 Hyperspheres method

Telling an attractor is chaotic is not enough to describe the situation of the BP. The assumed chaotic attractor can have different shapes and sizes. These properties are really important because they are the signaure of the practical unstability. A small chaotic attractor would be less troublesome than a large one, because the corresponding beliefs would be less eventful. In other terms, we need to reveal the chaos intensity of the BP, somehow given by the size of an attractor in the pseudo-state space.

Computing such a quantity turns out to be a quite hard task because it depends on the shape of the attractor. Assumed that we find this shape, nothing ensures that it is part of our knowledge, contrary to the regular forms whose analytic expressions of the volumes are known, as the spheres, the ellipsoids, the hypercubes... To circumvent this problem, we establish a procedure that provides the hypersphere circumbscribed to the pseudo-trajectory. Obviously the whole trajectory is not taken into account partly because it is important to get rid of the transcient.

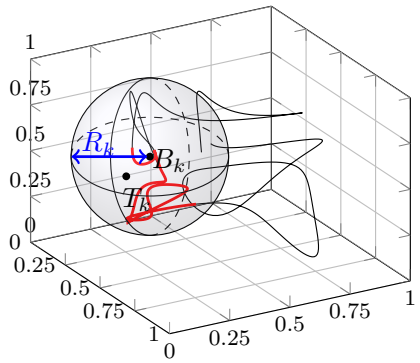

Fig. 12. Hyperspheres of radius R_k centered on B_k, the mean point of the pseudo-trajectory $\{T_{k-\frac{W}{2}}, \ldots, T_{k+\frac{W}{2}}\}$. The red points are inside the hypershere.

As shown on the figure 12, the method consists in:

- drag a temporal window $I_W(k)$ of arbitrary length W along the trajectory according to the iteration k,
- for each k extracting B_k the mean point of the pseudo-trajectory in $I_W(k)$,
- searching for T_k the furthest point of B_k inside $I_W(k)$.

The vector $\overrightarrow{B_kT_k}$ is of length r_k the radius of the hypersphere circumscribed to the pseudo-trajectory inside $I_W(k)$. A part of the estimator is the evolution

of r_k along the iterations. The difficulty lies in the experimental search for the length W such that the attractor is absorbed into the hypersphere. For the moment, only numerous experimental attempts help to find the well suited W. We present on figure 13 the evolution of r_k for the BP subjected to strong chaos according to the previous estimators.

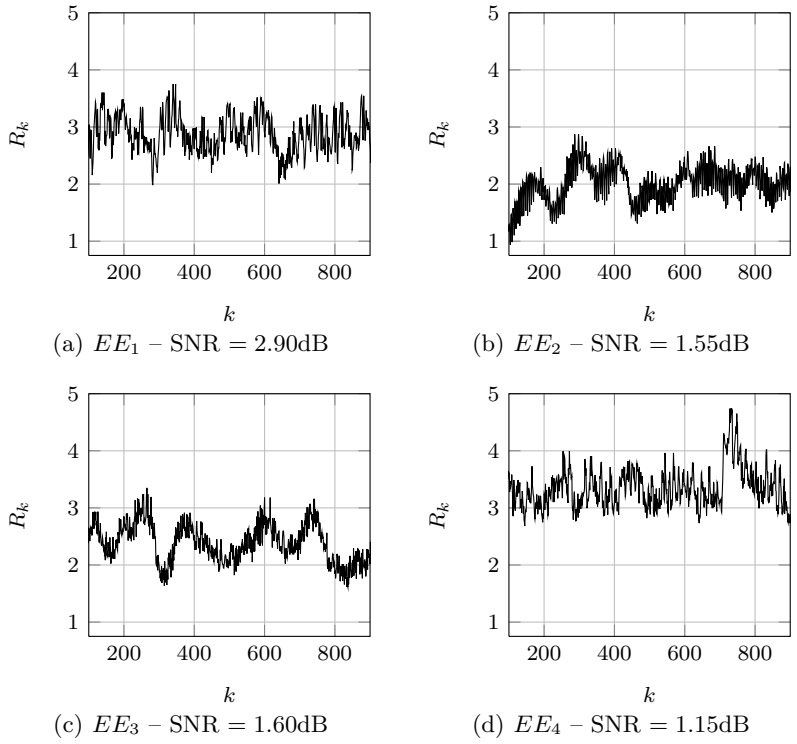

(a) EE_1 – SNR = 2.90dB (b) EE_2 – SNR = 1.55dB

(c) EE_3 – SNR = 1.60dB (d) EE_4 – SNR = 1.15dB

Fig. 13. Hypersphere radius R_k for chaotic attractors according to k

We see that the values of the radii are of the same magnitude, even though they are not strictly equal. Nevertheless, in the current pseudo-state space of $N = 155$ dimensions, the hypervolume of the hypersphere is proportionnal to R_k^N. Then even a small difference between two radii involves a non neglectible difference, a fact that we will see later. Another observation is the fact that these radii are not constant, meaning that the hyperspheres shake. Due to this phenomenon the radius is often almost doubled as for EE_2 about $k \in \{209, 298\}$. This is a consequence of the BP unstability. To get a global overview of the attractor size inside the state space we display on figure 14 the average steady value $\hat{R}_K$ for each error event according to the SNR. According to the previous estimators, it appears that the maxima of the radii are reached when the BP is trapped into chaotic attractors, and the minima are reached as soon as the algorithm left these attractors. In addition, a quite interesting observation is that $\hat{R}_K$ is smoothly increased while the SNR lies within the

limit cycle interval, meaning that these limit cycles are getting larger as the SNR is increased.

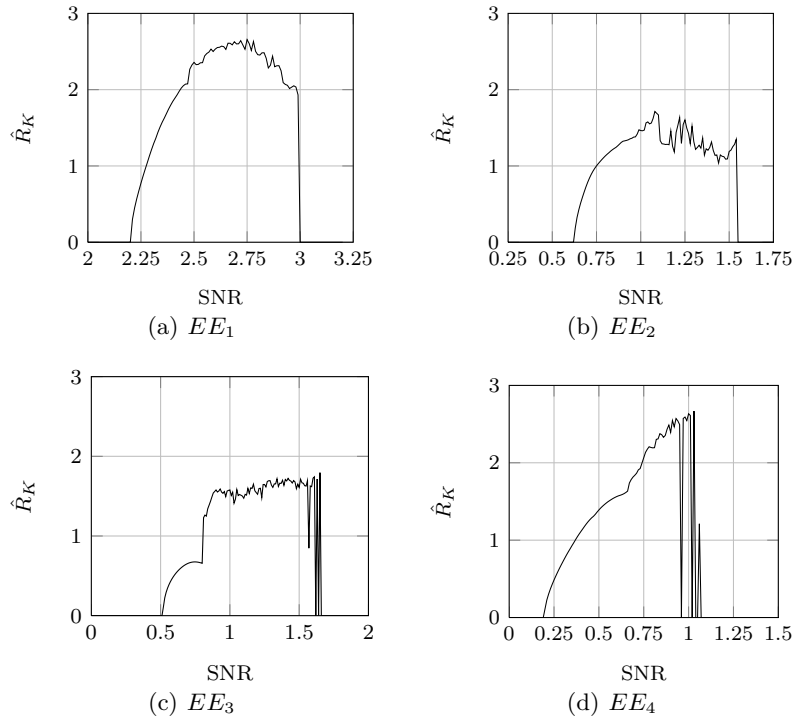

Fig. 14. Average hypersphere radius $\hat{R}_K$ for chaotic attractors according to the SNR

In the mean time, the Lyapunov exponent highlighted the information that initially close trajectories were moving away at a constant rate. Therefore as the limit cycle is growing, the stability of the BP does not really change provided the SNR is less than the critical values that leads to chaos. In other terms the divergence speed of two initially close trajectories is not changed even if the radius of the limit cycle increases, that is a quite surprising observation.

Finally it appear suitable to compare the values of the hyperspheres volumes so as to highlight their difference. In the table 3.4 are given the ratios between the maximum radii and the associated ratios between their corresponding hypervolumes, given that :

- $R_1 \triangleq \max \hat{R}_k(EE_1) = 2.6561$ reached at SNR $= 2.75$ dB,
- $R_2 \triangleq \max \hat{R}_k(EE_2) = 1.7139$ reached at SNR $= 1.08$ dB,
- $R_3 \triangleq \max \hat{R}_k(EE_3) = 1.7954$ reached at SNR $= 1.65$ dB,
- $R_4 \triangleq \max \hat{R}_k(EE_4) = 2.6684$ reached at SNR $= 1.03$ dB.

These tables raise the dramatical difference between the size of the chaotic attractors.

(a) Ratios between hyperspheres radii

	EE_1	EE_2	EE_3	EE_4
EE_1	.	$\frac{R_1}{R_2} = 1.5497$	$\frac{R_1}{R_3} = 1.4794$	$\frac{R_1}{R_4} = 0.9954$
EE_2	$\frac{R_2}{R_1} = 0.6453$	.	$\frac{R_2}{R_3} = 0.9546$	$\frac{R_2}{R_4} = 0.6423$
EE_3	$\frac{R_3}{R_1} = 0.6759$	$\frac{R_3}{R_2} = 1.0476$	.	$\frac{R_3}{R_4} = 0.6728$
EE_4	$\frac{R_4}{R_1} = 1.0046$	$\frac{R_4}{R_2} = 1.5569$	$\frac{R_4}{R_3} = 1.4862$	.

(b) Ratios between hyperspheres volumes

	EE_1	EE_2	EE_3	EE_4
EE_1	.	$\frac{V_1}{V_2} = 3.0788 \times 10^{29}$	$\frac{V_1}{V_3} = 2.3082 \times 10^{26}$	$\frac{V_1}{V_4} = 0.4894$
EE_2	$\frac{V_2}{V_1} = 3.2588 \times 10^{-30}$	.	$\frac{V_2}{V_3} = 7.4528 \times 10^{-4}$	$\frac{V_2}{V_4} = 1.5826 \times 10^{-30}$
EE_3	$\frac{V_3}{V_1} = 4.2833 \times 10^{-27}$	$\frac{V_3}{V_2} = 1.3499 \times 10^{3}$	.	$\frac{V_3}{V_4} = 2.1005 \times 10^{-27}$
EE_4	$\frac{V_4}{V_1} = 2.0368$	$\frac{V_4}{V_2} = 6.3156 \times 10^{29}$	$\frac{V_4}{V_3} = 4.6987 \times 10^{26}$	.

As an example, EE_4 involves a radius only 1.5569 times larger than the radius involved by EE_2 but $V_4 \approx 10^{29} V_2$ which is a very large difference. On the contrary error events whose radii are very close, as EE_1 and EE_4 do not differenciate much in terms of their corresponding hypervolumes. Finally, it appears a quite large diversity of chaotic attractors for the BP. This diversity lies within the intensity of the chaos, represented by the hypervolumes. This observation indicates that for example EE_2 entails a *less* chaotic attractor than EE_4, and that EE_1 implies a much *more* chaotic attractor than EE_2. Such comparisons provide somehow a reliability coefficient on the noise realizations, that is of very important practical interest.

4 Conclusion

In this paper, we address the dynamics issue of the BP by the use of known and new estimators from an experimental point of view. We brough out that the BP follows a systematic pattern when the decoding is not trivial: convergence to a small-sized attractor, locking in a limit cycle, chaos and convergence to a fixed-point. Such a property turns out to be practically relevant because it is common to all LDPC codes. In addition it provides the critical values of the SNR for which the BP could present complex behaviors. We investigated the chaos by the use of new estimators to highlight the diversity of the chaotic attractors that the BP would encounter. By the use of the hyperspheres method we introduced the notion of chaos intensity that highlighted a novel notion of reliability on the channel noise realizations, and to some extent on the SNR values and the LDPC codes. Finally we have introduced a quite efficient toolbox for the study of the BP that can be adapted to any decoding algorithm provided its output can be computed as probability distributions.

References

1.R.G. Gallager. Low-Density Parity-Check Codes. *PhD Thesis, MIT*, 1963.
2.F.R. Kschischang, B. J. Frey eand H.A. Loeliger. Factor Graphs and the Sum-Product Algorithm. *IEEE Trans. on Inf. Theory*, 47.2, 2001.
3.J. Pearl. Probablistic Reasoning in Intelligent Systems: Networks of Plausible Inference. *Morgan Kaufmann publisher*, 1988.
4.H.A. Bethe. Statistical Theory of Superlattices. *Proc. Roy. Soc. London*, 1935.
5.T.J. Richardson. Error floors of LDPC codes. *Proc. 41st Annual Allerton Conf. on Comm. Cont. and Comp.*, 2003.
6.S.Y Chung, T.J. Richardson and R.L. Urbanke. Analysis of Sum-Product Decoding of Low-Density Parity-Check Codes Using a Gaussian Approximation. *IEEE Trans. on Inf. Theory*, 47.2, 2001.
7.K.P. Murphy, Y. Weiss and M.I. Jordan. Loopy belef propagation for approximate inference: an empirical study. *Proc. Uncertainty in AI*, 1999.
8.T. Heskes. Convexity arguments for efficient minimization of the Bethe and Kikuchi free energies. *Journal of Artificial Intelligence Research*, 26:154–190, 2006.
9.X. Zheng, F.C.M. Lau, C.K. Tse and S.C. Wong. Study of bifurcation behavior of LDPC decoders. *Int. Journal of Bifurcation and Chaos*, 16:3435–3449, 2005.
10.R.M. Tanner, R. Michael, D. Sridhara and T. Fuja. A Class of Group-Structured LDPC Codes. 2001.
11.R. Hilborn. Chaos and Nonlinear Dynamics: An Introduction for Scientists and Engineers. *Oxford University Press publisher*, 2000.
12.M.T. Rosenstein, J.J. Collins and C.J. De Luca. A practical method for calculating largest Lyapunov exponents from small data sets. *Physica D*, 65:117–134, 1993.

Chaotic Modeling and Simulation (CMSIM) 1: 19–30, 2013

Pattern Formation in Volumetrically Heated Fluids

Gregory Cartland Glover[1] Kaoru Fujimura[2] and Sotos Generalis[3]

[1] Marie Curie IE Fellow, Mathematics, Aston University, Birmingham B4 7ET, UK
(E-mail: g.cartland-glover@aston.ac.uk)
[2] Applied Mathematics and Physics, Tottori University, Tottori 680-8552, Japan
(E-mail: kaoru@damp.tottori-u.ac.jp)
[3] Mathematics, Aston University, Birmingham B4 7ET, UK
(E-mail: s.c.generalis@aston.ac.uk)

Abstract. Finite element simulations have been performed along side normal mode analysis on the linear stability that examined the development of volumetrically heated flow patterns in a horizontal layer controlled by the Prandtl number, Pr, and the Grashof number, Gr. The fluid was bounded by an isothermal plane above an adiabatic plane. In the simulations performed here, a number of convective polygonal planforms occurred, as Gr increased above the critical Grashof number, Gr_c at $Pr = 7$, while roll structures were observed for $Pr < 1$ at $2Gr_c$.
Keywords: Non-linear, bifurcation, stability, volumetric heating, asymmetric boundaries.

1 Introduction

This work is concerned with the numerical simulation of the early stage transition regime of an internally heated fluid layer situated between a conducting upper boundary and an insulating lower boundary. The study described here is motivated by earlier studies [4,6,8] and the importance such flow structures have in the development of flows that are found in many engineering and geophysical applications.

Examples of volumetric heating cover thermal convection driven by the radioactive decay of fluid components. Asfia and Dhir [2] who studied thermal convection in a pool that mimicked the motion caused by fission product decay in the molten fuel elements that collect in the lower head of a nuclear reactor during a severe accident. Briant and Weinberg [3] devised the molten salt nuclear reactor concept, where the fissile material is dissolved in the coolant and thus provides volumetric heating to the fluid phase. Geophysical flows in the Earth's mantle are driven by radioactive decay [5,10,15,16]. Tritton and Zarraga [20], Tasaka *et al.* [18], Takahashi *et al.* [17] have studied the

Received: 29 November 2012 / Accepted: 22 January 2013

ISSN 2241-0503

phenomena experimentally using various approaches to generate fluid motion and record the structures observed.

Several numerical studies of thermal convection driven by internal heating have been performed using a variety of techniques to resolve the evolving circulation cells via the application of mean field approximations ([14]), expansions in orthogonal functions of finite amplitudes used in pseudospectral techniques ([8], [10], [15], [16], [9], [22], [19]) and finite volume or element approaches ([6], [11]).

Cartland Glover and Generalis [6] (hereafter indicated as CCG) focussed on domains with aspect ratios of $\left\{1 : 4\sqrt{3} : 12\right\}$ suggested by Ichikawa *et al.* [11]. Several types of circulation cells were observed by CGG [6], as the Grashof number, Gr, was increased, which corresponded to observatiosn of Roberts [14] at transition and to Tveiteried and Palm [22] at higher Gr. There were two key factors that affected the development of the circulation cells in CGG [6]. These were how the internal heating conditions were defined and the influence of the periodic conditions on the flow field. CGG [6] assumed an equivalent constant temperature difference of the applied heating and varied the depth between the parallel plates to control Gr and the internal heating supplied, which is not consistent with experimentation [20,18,17].

Thus, the motivation for this new study is two-fold: we are interested in reducing the error from the simulations in the wavenumber, which were observed around the critical transition and we would like to compare the numerical results obtained with the experimental results [20,18,17]. Note that in the finite element simulations performed here, the variation of the internal heating condition was driven by the varying temperature difference rather than modifying the depth between the parallel planes, the former of which is more consistent with experimental methods of Tasaka *et al.* [18] and Takahashi *et al.* [17] for example. To try to reduce the influence of the periodic boundary conditions and the any effect that the domain aspect ratio has on the formation of structures, the extent of the domain was also increased from $\left\{1 : 4\sqrt{3} : 12\right\}$ to $\{1 : 12 : 12\}$.

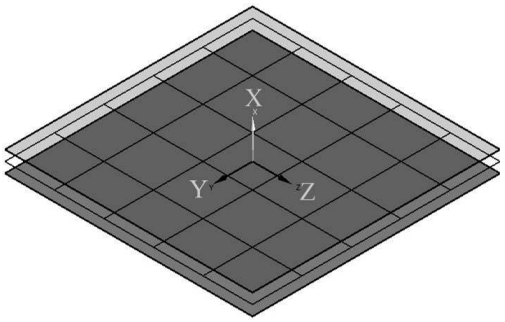

Fig. 1. Diagram of the homogeneous layer with an isothermal surface above an adiabatic surface. The coordinate axis is at the origin and the midplane surface is also indicated by the coarse grid.

2 Theory

We consider a volumetrically heated viscous incompressible fluid in a horizontal layer of width L bounded by plates of infinite extent (Figure 1). The upper plate is a conducting surface and the lower plate is an insulating surface. The cartesian coordinate system is located on the midplane of the layer (Figure 1). We start by following the Navier-Stokes equations for the velocity vector $\boldsymbol{u}$ and the pressure, p, and a transport equation for the temperature, T, from the environment

$$\nabla \cdot \boldsymbol{u} = 0,$$

$$\rho \frac{\partial \boldsymbol{u}}{\partial t} + \rho \left(\boldsymbol{u} \cdot \nabla \right) \boldsymbol{u} = -\nabla p + \mu \nabla^2 \boldsymbol{u} - \boldsymbol{g} \rho \beta \left(T - T_r \right),$$

$$\rho \frac{\partial T}{\partial t} + \rho \left(\boldsymbol{u} \cdot \nabla \right) T = \rho k \nabla^2 T + S_i,$$

where $\boldsymbol{g}$ is the acceleration due to gravity, k is the thermal conductivity, S_i is the volumetric heat source, T_r is the reference temperature of the fluid modelled and β is the thermal expansion coefficient.

2.1 Conditions Applied

We apply L, L^2/ν and $\Delta T_i = \left(Gr\mu^2 \right) / \left(g\rho^2\beta \ L^3 \right)$, as the units of length, time and temperature to non-dimensionalise the system. This gives $\boldsymbol{\upsilon}$, ϖ and θ as the non-dimensionalised velocity vector, pressure and temperature, respectively.

We obtain two non-dimensional numbers, which control the volumetric heating supplied to the horizontal layer and the influence of the thermal diffusivity. These are the Grashof number with the form $Gr = \left(g\rho^2\beta S_i L^5 \right) / \left(2\mu^2 k \right)$ and the Prandtl number, $Pr = \left(c_p \mu \right) / k$. The fluid properties are defined by the specific heat capacity at constant pressure, c_p, dynamic viscosity, μ and the density, ρ. Several Gr over the range $1 \leq \varepsilon \leq 12$ were selected in order to vary the temperature difference at $Pr = 7$ and therefore the heat flux applied, where $\varepsilon = Gr/Gr_c$. Then Pr was varied to observe the influence of thermal diffusion on the resolved flow states. The product of Grashof number and the Prandtl number gives the Rayleigh number.

The boundary conditions are $\theta|_{x=1} = 0$, $\partial_x \theta|_{x=0} = 0$, $\boldsymbol{\upsilon}|_{x=0} = \boldsymbol{\upsilon}|_{x=1} = 0$ and the initial conditions are $\theta = 0$ and $\boldsymbol{\upsilon} = 0$. We assume the Boussinesq approximation applies to the definition of the fluid phases and the volumetrically applied heating.

The treatment (described below) of the non-dimensional numbers and the initial and boundary conditions differs between the numerical simulations by means of the finite element method and the linear stability analysis.

2.2 Linear stability analysis

To perform the linear stability analysis we start with the non-dimensional form of the governing equations:

$$\nabla \cdot \boldsymbol{\upsilon} = 0,$$

$$\frac{\partial \boldsymbol{\upsilon}}{\partial t} + (\boldsymbol{\upsilon} \cdot \nabla)\, \boldsymbol{\upsilon} = -\nabla \varpi + \nabla^2 \boldsymbol{\upsilon} - \frac{\boldsymbol{g}}{g}\theta,$$

$$\frac{\partial \theta}{\partial t} + (\boldsymbol{\upsilon} \cdot \nabla)\, \theta = \frac{1}{Pr}\left(\nabla^2 \theta + 2Gr\right),$$

The basic field in the conduction state without macroscopic flow is due to a static balance of the pressure with the buoyancy force. Under the imposed boundary conditions the basic temperature, $\bar{\theta}$, is given by $Gr(x^2 + 2x - 3)/2$ [14], where x is non-dimensionalised by L and t by L^2/ν.

Let us denote the deviation of $\boldsymbol{\upsilon}$, ϖ, and θ from the basic field by $\hat{\boldsymbol{\upsilon}}$, $\hat{\varpi}$, and $\hat{\theta}$. We linearize the governing equations for the disturbance, and assume the normal mode such that

$$\begin{pmatrix} \hat{\boldsymbol{\upsilon}} \\ \hat{\varpi} \\ \hat{\theta} \end{pmatrix} \propto \begin{pmatrix} \boldsymbol{\Upsilon}(x) \\ \mathit{\Pi}(x) \\ \Theta(x) \end{pmatrix} e^{\sigma t + \imath(\alpha_y y + \alpha_z z)}$$

We substitute this expression into the linearized governing equations. The resulting ODEs for the 'amplitude functions of the normal mode', $\boldsymbol{\Upsilon}(x)$, $\mathit{\Pi}(x)$, and $\Theta(x)$, form a linear eigenvalue problem under non-slip boundary conditions, $\boldsymbol{\Upsilon} = 0$ at $x = 0$ and 1 and the thermal boundary conditions $\Theta = 0$ at x = 1 and $\Theta' = 0$ at $x = 0$.

At this stage, we introduced the toroidal-poloidal decomposition to eliminate $\mathit{\Pi}(x)$. See [8,12] for details. We discretize the amplitude functions by means of an expansion in Chebyshev polynomials. Applying the collocation method together with tau method, we reduce the linear eigenvalue problem corresponding to two-point boundary value problem to an algebraic linear eigenvalue problem of the form $A\boldsymbol{x} = \sigma B\boldsymbol{x}$, which is solved numerically by means of the QZ algorithm. Twenty polynomials are used to resolve the neutral curves presented here.

At the end of this subsection, we note that since the basic field has Euclidean symmetry E(2) on the yz-plane, there is no preferred direction there. This implies that a wave vector (α_y, α_z) on two-dimensional wave plane does not appear in the eigenvalue problem. Instead, the wavenumber $\alpha = \sqrt{\alpha_y^2 + \alpha_z^2}$ is involved.

2.3 Simulation method

As the solver used in the finite element method used dimensional equations [1], it is necessary to specify $S_i = (2k\Delta T_i)/L^2$ in terms of Gr (see below) and $L = 0.007$ m, which was defined according to the experimental studies of Tasaka *et al.* [18]. Periodic conditions are applied to the vertical surfaces of

the domain Figure 1. Please refer to CGG [6] for a thorough description of the specifications required to perform the finite element method simulations. Key exceptions from CGG [6] are the domain used, which was a square layer with an aspect ratio of $\{1:12:12\}$ that had the respective node resolution of $\{30:180:180\}$ and the assumed physical time-scale, $c_p\rho L^2/k$, to control the rate of convergence.

3 Results

The resultant solutions for convection caused by volumetrically heating a horizontal layer show the deviations from the conductive laminar state. At $Pr = 7$, the transition from conductive to convective flow occurs at Gr_c= 198, which corresponds to $Ra_c = 1386$ ([14], [11], [22]). The structures are indicated by the change in characteristic parameters, which are plotted between Figure 2 and Figure 5. Figure 2 presents the neutral curves obtained by the linear analysis. Contour plots of the temperature and the vertical velocity component for $Pr = 7$, where $\varepsilon = 1$, 2, 3, 6 and 12 are illustrated in Figure 3. The change of velocity components and the temperature with ε are plotted in Figure 4. Contour plots of the temperature and the vertical velocity component for Pr = 0.005, 0.705, 0.883 and 8.933 are given in Figure 5.

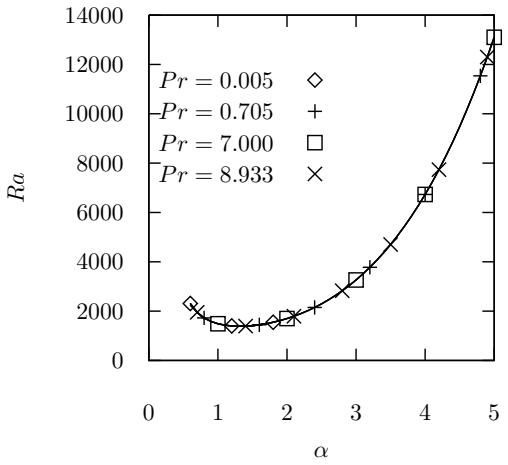

Fig. 2. Neutral curves of stability (solid lines) obtained from the linear normal mode analysis, where α is the wavenumber.

3.1 Fluids with Pr=7

The neutral curves obtained from the linear normal mode analysis are given in Figure 2, where the curves indicate the highest value allowed by the linear analysis for the basic state to retain its laminar form.

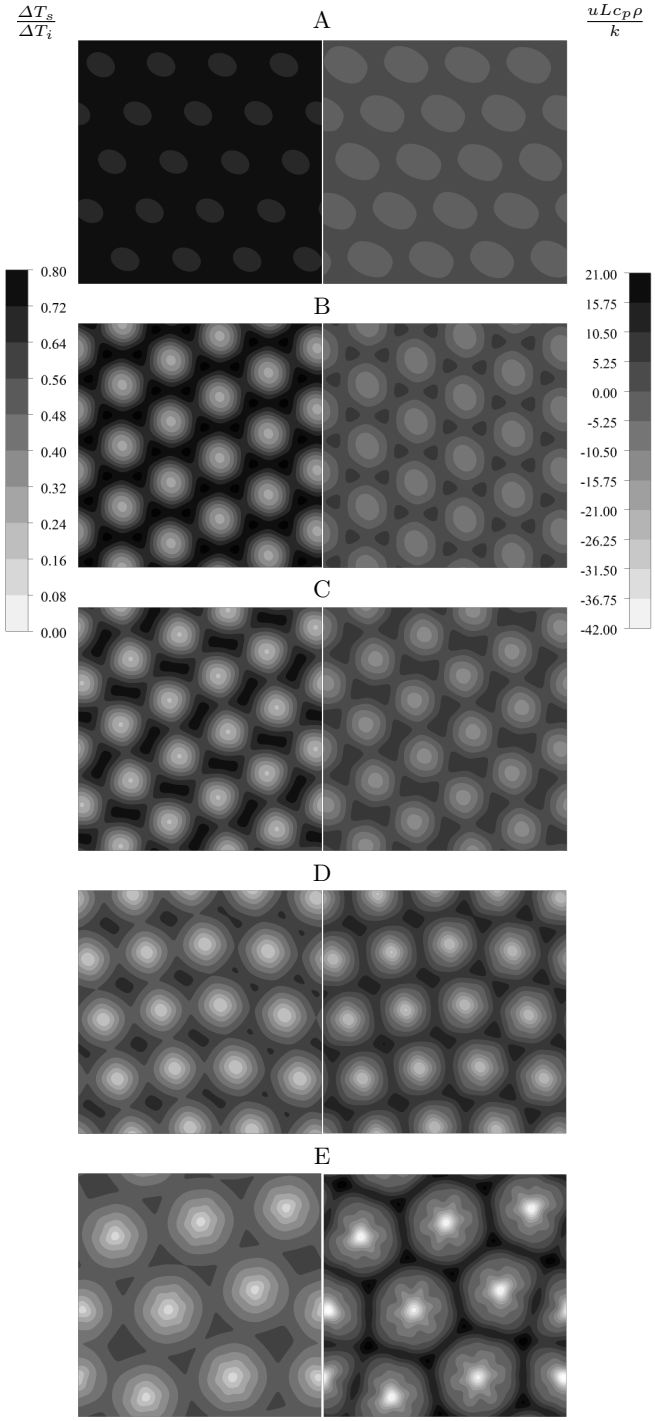

Fig. 3. Non-dimensional temperature (left) and vertical velocity (right) contours on the midplane in Figure 1, for Pr=7 . Here $\Delta T_s/\Delta T_i = |T - T_{\min}|_s / \left(Gr\mu^2\right) / \left(g\rho^2\beta\ L^3\right)$. A: $\varepsilon = 1$; B: $\varepsilon = 2$; C: $\varepsilon = 3$; D: $\varepsilon = 6$; E: $\varepsilon = 12$.

At ε=1, Figure 3 already shows non-vanishing hexagonal pattern. This is due to the fact that the solution branch of the down-hexagons bifurcates subcritically i.e. ε <1, as reported by Tveitereid and Palm [22]. Indeed, the branch of stable down-hexagons ends up with a limit point (or saddle-node point) at which the stable upper branch is connected with the lower branch of the transcritical bifurcation stemmed subcritically from the bifurcation point ε=1. The stable down-hexagons are generated in the following sequence: hexagons true to the y axis at $\varepsilon = 1$ (Figure 3A), hexagons perpendicular to the y axis (Figure 3B), hexagons aligned at $\sim 50^{\circ}$ to y axis (Figure 3C), polygonal structures (Figure 3D), hexagons with spokes (Figure 3E). Note that the change in the alignment of the hexagons between Figure 3A and 3C indicates that there is no preference in the orientation of the hexagons.

The structures depicted in Figure 3 are qualitatively comparable with the experimental studies of Takahashi *et al.* [17] and Tasaka *et al.* [18], where measurements of the temperature field [18] and the velocity field [17] were made for $\varepsilon \in (3, 6)$. These conditions correspond to cases C and D presented in Figure 3. The increase in the size of the circulation cell is of a similar magnitude in both the experiments and the simulation. The range of vertical velocities observed in the simulations described are similar to those reported by Takahashi *et al.* [17].

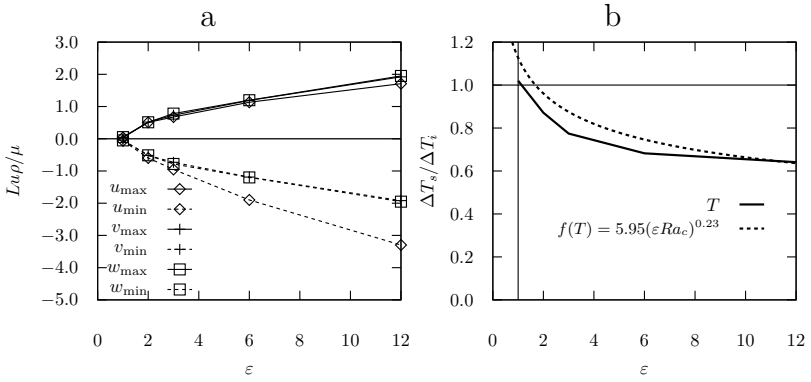

Fig. 4. Profiles against ε obtained from the finite element code. a) The maximum and the minimum values of the velocity components; b) $\Delta T_s/\Delta T_i = T_{\max} - T_{\min}/\left(Gr\mu^2\right)/\left(g\rho^2\beta\ L^3\right)$, where s refers to the temperature extracted from the solved flow field. $f(T) = 5.95(\varepsilon * Ra_c)^{-0.23}$, an empirical profile given by Turcotte *et al.* [21]; horizontal line: conduction condition; vertical line: transition between conduction and convection.

In Figure 4 we show the change of key variables with ε for the simulations using the finite element code. A significant increase in all the velocity components at $\varepsilon = 1$ in Figure 4a. The increases in the velocity are associated with the change in the state of the fluid layer at the critical transition, where we conjecture that isotropic hexagons are formed. The patterns formed are

considered to be isotropic as the minima and maxima of the v and w display similar magnitudes.

The down-welling minimum velocity indicated in Figure 11 of Takahashi *et al.* [17] gave vertical velocities, which were approximately one third less than the vertical velocities in Figure 4a. This difference could be due to methods used to assess the minimum vertical velocity or the influence of the heat flux across the lower boundary used. The minimum vertical velocity of Takahashi *et al.* [17] was determined from the planes defined by the laser sheets used for their PIV measurements, while the velocities in Figure 4a are the minimum and maximum values for the whole of the simulated domain.

The effect of the transition from conductive to convective flow is also shown by the change in the temperature difference relative to the initial or conductive temperature difference (Figure 4b). At higher heat fluxes the temperature difference caused by convection drops below the conductive temperature difference. This is due to the influence that cellular convection has on the layer as energy from the volumetric heat source is used to drive the fluids across the layer [5]. A portion of the internal heating supplied is also lost from the system through the top isothermal boundary [20]. An empirical relation of the decrease in the temperature difference due to convection is also plotted in Figure 4 [21].

3.2 Other fluids

To confirm the secondary flows predicted by the finite element code soon after Gr_c show behaviour consistent with literature, fluids of different Pr were tested for $\varepsilon = 2$ (Figure 5). For $Pr < 1$, the circulation cells take the form of steady ($0.5 < \mathrm{Pr} < 1$) or unsteady ($Pr < 0.1$) two-dimensional rolls. While a mix of polygonal structures occur for $Pr = 8.933$. For $Pr \simeq 0.70$ dislocations in the roll structures are also observed, which may disappear in time-averaged plots obtained from a time-marching solution. For $Pr \simeq 0.85$, where supercritical or high pressure fluids were considered within CFX, large variations in the fluid density can occur for small changes in the temperature [13]. Therefore, in the limit of the Boussinesq approximation (i.e. constant density), the heating condition we applied resulted in small non-measureable differences in the temperature. This lead to the formation of sharply defined differences in the temperature.

4 Conclusions

The main interest in the present work is the hierarchical transition from conductive flow to convective flow and on to the turbulent regime in an asymmetric horizontal layer. We have concentrated on the stability boundary of the basic state in order to compare states found numerically with those observed in experiments ([18],[17]). The present study used both finite element simulations and linear stability analysis to indicate that hexagonal cells are the preferred mode for the evolution of homogeneous systems at around the critical point for $Pr = 7$.

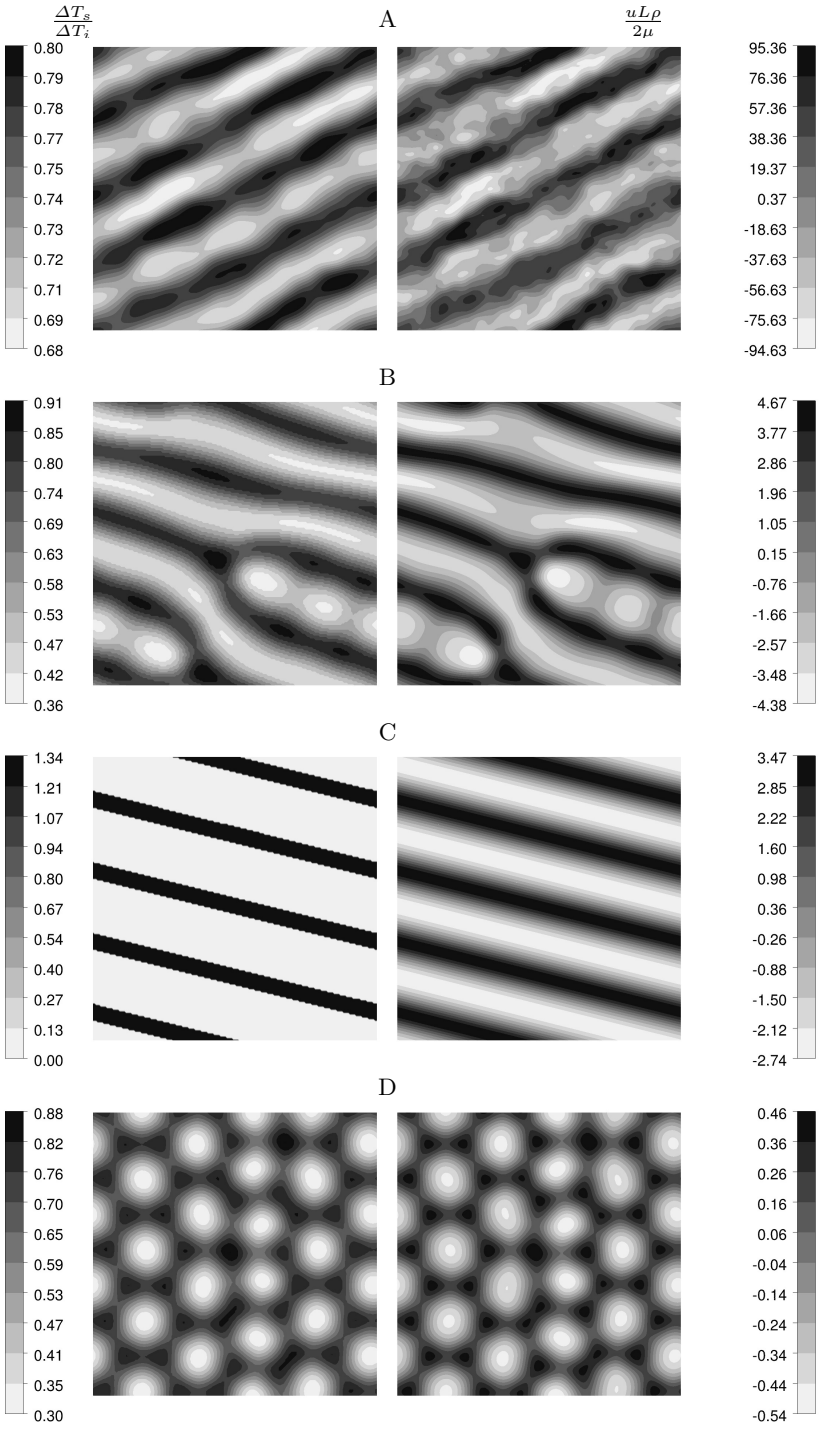

Fig. 5. Non-dimensional temperature (left) and vertical velocity (right) contours on the midplane in Figure 1, for different Pr at $\varepsilon = 2$. Here $\Delta T_s/\Delta T_i = |T - T_{\min}|/\left(Gr\mu^2\right)/\left(g\rho^2\beta\, L^3\right)$. A: $Pr = 0.005$; B: $Pr = 0.705$; C: $Pr = 0.883$; D: $Pr = 8.933$.

Beyond $\varepsilon = 6$ at $Pr = 7$, the finite element code predicts that the secondary structures deform resulting in different possibly rectangular states that are qualitatively comparable with the experimental studies of the Takeda group ([18],[17]). Between $\varepsilon = 1$ and $\varepsilon = 3$ the changes in orientation of the structures indicates that there is no preference in their orientation. Further non-linear analyses are being performed to explore the stability of the flow patterns observed at the transition to convective flow for a homogeneously heated layer with asymmetric boundary conditions.

Acknowledgements

The work presented here was funded by a Marie-Curie Intra-European Fellowship (Project No. 274367) for the European Commission and by the Royal Academy of Engineering Distinguished Visiting Fellowship Scheme. We wish to thank the Institute for Safety Research at the Helmholtz-Zentrum Dresden-Rossendorf for kindly allowing access to the computational cluster upon which the computational fluid dynamic calculations were performed.

Nomenclature

c_p	specific heat capacity at constant pressure, J kg^{-1} K^{-1}
Gr	Grashof number, $Gr = g\beta\rho^2 S_i L^5/2\mu^2 k$
Gr_c	critical Grashof number, Gr_c
$\boldsymbol{g}$	vector of the acceleration due to gravity, m s^{-2}
g	acceleration due to gravity, m s^{-2}
k	thermal conductivity, W m^{-1} K^{-1}
L	characteristic length, 0.007 m
Pr	Prandtl number, $Pr = c_p/\mu k$
p	pressure, kg m^{-1} s^{-2}
Ra	Rayleigh number $Ra = GrPr$
Ra_c	critical Rayleigh number $Ra_c = 1386$
S_i	volumetric heat source $S_i = 2k\Delta T_i/L^2$, kg m^{-1} s^{-3}
$\boldsymbol{S}$	momentum source terms, kg m^{-1} s^3
T	temperature, K
T_r	reference temperature, K
ΔT_i	initial temperature difference, $\Delta T_i = \left(Gr\mu^2\right) / \left(g\rho^2\beta\ L^3\right)$, K
ΔT_s	temperature difference of the solved flow, K
t	time, s
$\boldsymbol{u}$	velocity vector, m s^{-1}
u, v, w	velocity vector components, m s^{-1}
x, y, z	direction vector components, m

Greek symbols

α	wavenumber
β	expansion coefficient, 1/K
ε	reduced Grashof number = Gr/Gr_c

θ	non-dimensional temperature
μ	dynamic viscosity, kg m^{-1} s^{-1}
ϖ	non-dimensional pressure
ρ	density, kg m^{-3}
σ	eigenvalue
$\boldsymbol{\upsilon}$	non-dimensional velocity vector

References

1. ANSYS® CFX 12. *Theory Guide*, Canonsburg, USA, 2009, ANSYS Inc.
2. F. J. Asfia and V. K. Dhir. An experimental study of natural convection in a volumetrically heated spherical pool bounded on top with a rigid wall. *Nucl Eng Des*, 163:333-348, 1996.
3. R. C. Briant and A. M. Weinberg. Molten fluorides as power reactor fuels. *Nucl Sci Eng*, 2:797-803, 1957.
4. F. H. Busse. The stability of finite amplitude cellular convection and its relation to an extremum principle. *J Fluid Mech*, 30(4):625-649, 1967.
5. F. H. Busse. Fundamentals of thermal convection. In W. R. Peltier, editor, *Mantle Convection. Plate Tectonics and Global Dynamics (Fluid mechanics of astrophysics and geophysics vol 4)* pages 23-95, New York, 1989. Gordon and Breach.
6. G. M. Cartland Glover and S. C. Generalis. Pattern competition in homogeneously heated fluid layers. *Eng Appl Computat Fluid Mech*, 3(2):164-174, 2009.
7. R. M. Clever and F. H. Busse. Hexagonal convection cells under conditions of vertical symmetry. *Phys Rev E*, 53(3):2037-2040, 1996.
8. S. Generalis and M. Nagata. Transition in homogeneously heated inclined plane parallel shear flows. *J Heat Tran*, 125:795-803, 2003.
9. G. M. Gershuni, E. M. Zhukhovitsky and A. A. Yakimov. On stability of plane-parallel convective motion due to internal heat sources. *Int J Heat Mass Tran*, 17(7):717-726, 1974.
10. G. Houseman. The dependence of convection planform on mode of heating, Nature 332:346-349, 1988.
11. H. Ichikawa, K. Kurita, Y. Yamagishi and T. Yanagisawa. Cell pattern of thermal convection induced by internal heating. *Phys Fluids*, 18:038101, 2006.
12. M. Nagata and S. Generalis. Transition in convective flows heated internally. *J Heat Tran*, 124:635-642, 2002.
13. NIST. *NIST Chemistry WebBook*, Gaithersburg, USA, 2012, NIST.
14. P. H. Roberts. Convection in horizontal layers with internal heat generation. Theory. *J Fluid Mech*, 30(1):33-49, 1967.
15. J. Schmalzl, G. A. Houseman and U. Hansen. Mixing properties of three-dimensional (3-d) stationary convection. *Phys Fluids*, 7(5):1027-1033, 1995.
16. G. Schubert, G. A. Glatzmaier and B. Travis. Steady, three-dimensional, internally heated convection. *Phys Fluids*, 5(8):1928-1932, 1993.
17. J. Takahashi, Y. Tasaka, Y. Murai, Y. Takeda and T. Yanagisawa. Experimental study of cell pattern formation induced by internal heat sources in a horizontal fluid layer. *Int J Heat Mass Tran*, 53(7-8):1483-1490, 2010.
18. Y. Tasaka, Y. Kudoh, Y. Takeda and T. Yanagisawa. Experimental investigation of natural convection induced by internal heat generation. *J Phys Conf Ser*, 14:168-179, 2005.
19. Y. Tasaka and Y. Takeda. Effects of heat source distribution on natural convection induced by internal heating. *Int J Heat Mass Tran*, 48:1164-1174, 2005.

20. D. J. Tritton and M. N. Zarraga. Convection in horizontal layers with internal heat generation. *J Fluid Mech*, 30(1):21-31, 1967.
21. D. L. Turcotte, J. Schubert and G. Schubert. *Geodynamics*, second edition, pp. 280, Cambridge University Press, Cambridge, 2001.
22. M. Tveitereid and E. Palm. Convection due to internal heat sources. *J Fluid Mech*, 76:481-499, 1976.

Chaotic Modeling and Simulation (CMSIM) 1: 31–38, 2013

Complex Dynamics and Phase Transitions Caused by Fuzzy Rationality

Ihor Lubashevsky[1] and Dmitry Parfenov[2]

[1] University of Aizu, Ikki-mach, Aizu-Wakamatsu, Fukushima, 965-8580, Japan
(E-mail: i-lubash@u-aizu.ac.jp)
[2] General Physics Institute, Russian Academy of Sciences, Vavilov str. 38, Moscow, 119991, Russia
(E-mail: narytyan@gmail.com)

Abstract. The notion of dynamical traps is proposed to allow for effect caused by the bounded capacity of human cognition in ordering events or actions according to their preference. As a result, in the vicinity of an optimal behavior a decision-maker has no stimulus to change his current behavior. By way of example, one dimensional system of coupled oscillators with dynamical traps is studied numerically. The model assumes the dynamical traps to form a "low" dimensional region in the corresponding phase space where the system motion is stagnated. It is demonstrated that the dynamical traps and possible noise individually can cause the given system to exhibit complex dynamics and to undergo various phase transitions.
Keywords: Human behavior, Fuzzy rationality, Dynamical traps, Complex dynamics, Phase transitions.

1 Introduction

During the last decades there has been considerable progress in describing social systems based on physical formalism developed in statistical physics and applied mathematics (for a review see articles in Encyclopedia [1]). In particle, the notion of energy and the based on it master equation were employed to simulate opinion dynamics, the dynamics of culture and languages (e.g., [2–4]); the social force model inheriting the basic concepts from Newtonian mechanics was used to simulate traffic flow, pedestrian motion, the motion of bird flocks, fish schools, swarms of social insects (e.g., [2,5–7]). Continuing the list of examples, we note the application of the Lotka-Volterra model and the related reaction-diffusion systems to stock market, income distribution, population dynamics [8]. The replicator equations developed initially in the theory of species evolution were applied to the moral dynamics [9]. The notion of a fixed-point attractor as a stable equilibrium point in the system dynamics that corresponds to some local minimum in a certain potential relief, the collection

Received: 6 April 2012 / Accepted: 4 October 2012

ISSN 2241-0503

of point type attractors forming a basin, the notion of latent attractors, periodic attractors representing limit cycles, and deterministic chaos are widely met in social psychology [10]. In addition, the concept of synchronization of interacting oscillators was used to model social coordination [11].

In spite of these achievements we have to note that the mathematical theory of social systems is currently at its initial stage of development. Indeed, animate beings and objects of the inanimate world are highly different in their basic features, in particular, such notions as willingness, learning, prediction, motives for action, moral norms, personal and cultural values are just inapplicable to inanimate objects. This enables us to pose a question as to what *individual* physical notions and mathematical formalism should be developed to describe social systems in addition to the available ones inherited from modern physics.

The present paper discusses one of such notions, namely, the fuzzy rationality [12] introduced here to describe the bounded capacity of human cognition in evaluating events, actions, etc. according to their preference. When, for example, two actions are close to each other in quality from the standpoint of a person making a decision their choice may be random because he ought to consider them equivalent. The notion of dynamical traps accounts for this feature. In particular, dealing with a dynamical system its stationary point $\mathbf{r}_{\mathsf{st}}$ being initially stable is replaced by a certain neighborhood $\mathbf{Q}_{\mathsf{tr}}$ called the dynamical trap region such that when the system goes into $\mathbf{Q}_{\mathsf{tr}}$ its dynamics is stagnated. This mimics vain actions of an operator in directing the system motion towards the point $\mathbf{r}_{\mathsf{st}}$ precisely. Indeed, when the system under the operator control gets any point in $\mathbf{Q}_{\mathsf{tr}}$ the operator may consider the current situation perfect because he just does not "see" $\mathbf{r}_{\mathsf{st}}$ and until the system leaves $\mathbf{Q}_{\mathsf{tr}}$ he has no reason to keep the control active. The goal of the present work is to demonstrate that the fuzzy rationality can be responsible for complex emergent phenomena in such systems.

2 Lazy bead model

The following model captures the basic features of such human behavior. Let us consider a chain of N "lazy" beads (Fig. 1). Each of these beads can move in the vertical direction and its dynamics is described in terms of the deviation $x_i(t)$ from the equilibrium position and the motion velocity $v_i(t) = dx_i/dt$ depending on time t, here the bead index i runs from 1 to N. The equilibrium position $x_i = 0$ is specified assuming the formal initial ($i = 0$) and terminal ($i = N + 1$) beads to be fixed. Each bead i "wishes" to get the "optimal" middle position with respect to its nearest neighbors. So one of the stimuli for it to accelerate or decelerate is the difference

$$\eta_i = x_i - \frac{1}{2}(x_{i-1} + x_{i+1})$$

provided its relative velocity

$$\vartheta_i = v_i - \frac{1}{2}(v_{i-1} + v_{i+1})$$

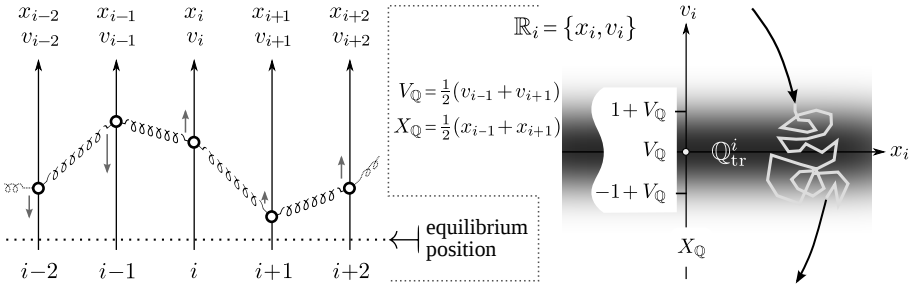

Fig. 1. The chain of N beads under consideration and the structure of their individual phase space $\mathbf{R}_i = \{x_i, v_i\}$ $(i = 1, 2, \ldots, N)$. The formal initial $i = 0$ and terminal $i = N + 1$ beads are assumed to be fixed, specifying the equilibrium bead position.

with respect to the pair of the nearest beads is sufficiently low. Otherwise, especially if bead i is currently located near the optimal position, it has to eliminate the relative velocity ϑ_i, representing the other stimulus for bead i to change its state of motion. The model to be formulated below combines both of these stimuli within one cumulative impetus $\propto (\eta_i + \sigma\vartheta_i)$, where σ is the relative weight of the second stimulus.

When, however, the relative velocity ϑ_i becomes less then a threshold θ, i.e., $|\vartheta_i| \lesssim \theta$, bead i is not able to recognize its motion with respect to the nearest neighbors. Since a bead cannot "predict" the dynamics of its neighbors, it has to regard them as moving uniformly with the current velocities. So from its standpoint, under such conditions the current situation cannot become worse, at least, rather fast. In this case bead i just "allows" itself to do nothing, i.e., not to change the state of motion and to retard the correction of its relative position. This feature is the reason why such beads are called "lazy". Below we will use dimensionless units in which, in particular, the perception threshold is equal to unity $\theta = 1$.

Under these conditions the equation governing the system dynamics is written in the following form

$$\frac{dv_i}{dt} = -\Omega(\vartheta_i)[\eta_i + \sigma\vartheta_i + \sigma_0 v_i] + \epsilon\xi_i(t)\,. \tag{1}$$

If the cofactor $\Omega(\vartheta_i)$ were equal to unity, the given system would be no more then a chain of beads connected by elastic springs characterized by the friction coefficient σ. The term $\sigma_0 v_i$ with the coefficient $\sigma_0 \ll 1$ that can be treated as a certain viscous friction of the beads moving via a medium into which the given system is embedded has been introduced to prevent the beads from attaining extremely high velocities. The factor $\Omega(\vartheta_i)$ is due to the effect of dynamical traps and the ansatz

$$\Omega(\vartheta) = \frac{\Delta + \vartheta^2}{1 + \vartheta^2}\,, \tag{2}$$

is used, where the parameter $\Delta \in [0, 1]$ quantifies the intensity of dynamical traps. If $\triangle = 1$, the dynamical traps do not exist at all, in the opposite case,

$\triangle \ll 1$, their influence is pronounced inside the neighborhood $\mathbf{Q}^i_{\mathsf{tr}}$ of the axis $v_i = (v_{i-1} + v_{i+1})/2$ (the trap region) whose thickness is about unity (Fig. 1). Model (1) allows for random factors in terms of white noise $\xi_i(t)$ affecting the motion of bead i with intensity ϵ so that

$$\langle \xi_i(t) \rangle = 0 \quad \text{and} \quad \langle \xi_i(t) \xi_{i'}(t') \rangle = \delta_{ii'} \delta(t - t') \,. \tag{3}$$

For the terminal fixed beads, $i = 0$ and $i = N + 1$, we set

$$x_0(t) = 0 \,, \qquad x_{N+1}(t) = 0 \,, \tag{4}$$

which play the role of the "boundary" conditions for equation (1).

It should be noted that the emergent phenomena in a similar system mimicking car following dynamics were considered for the first time in Refs [13,14]. In addition, the first experimental evidence of the dynamical traps caused by the human fuzzy rationality seems to be obtained in hybrid human-computer experiments of balancing a damped virtual stick [15].

3 Results of simulation

The dynamics of the given system was studied numerically. Initially all the beads were located at the equilibrium positions $\{x_i|_{t=0} = 0\}$ and perturbations were introduced into the system via ascribing random independent values to their velocities. Equation (1) was integrated using the E2 high order stochastic Runge-Kutta method [16]. The integration time step of 0.001 was used; the obtained results were checked to be stable with respect to decreasing the integration time step tenfold. The integration time was equal to 10^5–10^6, which enabled us to deal with the steady state dynamics. The other parameters used in simulation were taken equal to $\Delta = 10^{-3}$ and $\sigma_0 = 0.01$. Besides, to simply the data visualization the bead coordinates are shown with some individual shifts, namely, $x_i \to x_i + 50 \cdot i$.

In order to analyze the dynamical trap effect on its own the noise absence case was studied first. The system dynamics was found to depend on the intensity of "dissipation" quantified by the parameter σ. We remind that the parameter σ specifies the relative weight of the stimuli to take the middle "optimal" position and to eliminate the relative velocity; the larger the parameter σ, the more significant the latter stimulus. When the parameter σ is not too small the system tends to get the regime of regular dynamics represented by a collection of limit cycles of individual bead motion. It should be noted that these limit cycles could be of complex form when the number of beads is not too large, namely, $N \lesssim 10$ [17]. Nevertheless for systems with large number of beads the resulting phase portrait takes a rather universal form shown in Fig. 2(left frame). However, the "time to formation" T_N, i.e. the mean time required for a given bead chain to get the steady state regular dynamics grows exponentially as the number of beads increases. For example, for beads with $\sigma = 1$ this time can be approximated by the function

$$T_N \approx T_c \cdot \exp\{N/N_c\} \qquad \text{with } T_c \sim 60 \text{ and } N_c \sim 13 \tag{5}$$

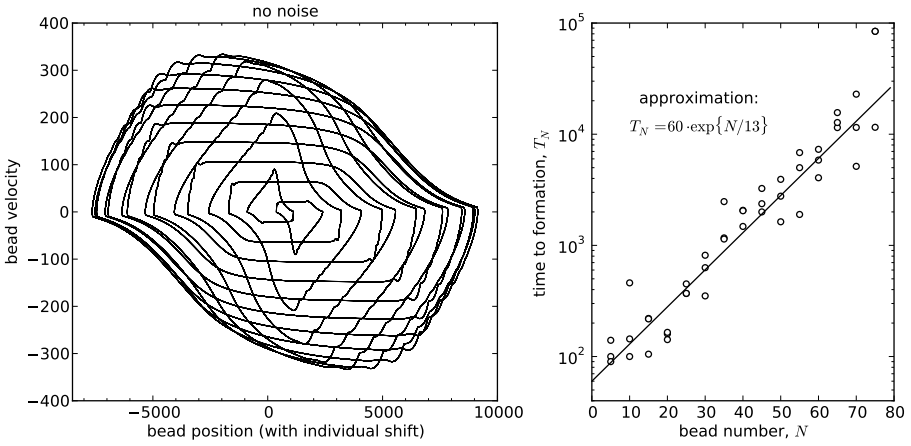

Fig. 2. The characteristic phase portrait of the steady state dynamics exhibited by systems without noise and not too weak "dissipation" (left frame). The chain of 30 beads with $\sigma = 1$ was used in constructing the shown pattern where the limit cycles of each second bead are visualized. The right frame depicts the characteristic time T_N required for such a system to get the steady state dynamics vs the number N of beads. The scatted points are the data obtained for each value of N on three trials, $\sigma = 1$ was used in simulation.

(see Fig. 2(right frame)). On one hand, this strong dependence explains that for chains of oscillators with not too weak "dissipation" only chaotic motion was found when the number of beads becomes sufficiently large, $N \gtrsim 100$ [17]. On the other hand, it enables us to pose a question about regarding the chaotic dynamics of such systems for $N \to \infty$ as a certain phase state.

In the case of weak "dissipation" the system dynamics exhibits sharp transition to a stable chaotic regime as the coefficient σ decreases. It is demonstrated in Fig. 3 showing the transition from the regular dynamics for $\sigma = 0.1$ to a chaotic motion when $\sigma = 0.09$. As seen in Fig. 3 the chaotic portrait can be conceived of as a highly chaotic kernel surrounded by fragments of the regular limit cycle destroyed by instability.

Noise forces these systems to undergo two phase transitions as its intensity ϵ increases. The first one can be categorized as the transition from the regular bead motion to a cooperative chaotic bead motion. The latter means that the beads correlate substantially with one another in motion but individual trajectories are rather irregular and the magnitude of this irregularity cannot be due to the present noise only. The second transition is determined by the formation of highly irregular mutually independent oscillations in the bead position. To illustrate the first phase transition Figure 4 depicts two phase portraits of the middle bead motion for different values of ϵ. As seen, for $\epsilon = 0.01$ the phase portrait looks like a regular limit cycle disturbed by small noise. In contrast, when the noise intensity increases by two times, i.e., $\epsilon = 0.02$, the corresponding phase portrait becomes rather complex in form and the volume of the phase space layer containing the shown trajectory as a whole

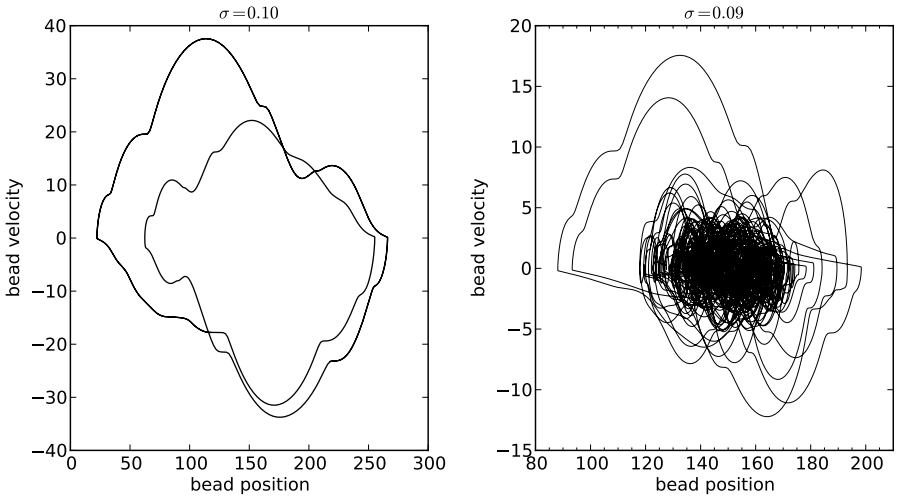

Fig. 3. The phase portraits of the middle bead motion of the 5-bead chain for the "dissipation" parameter σ taking the values 0.1 (left frame) and 0.09 (right frame). The period of the shown limit cycle is about 200; the chaotic phase portrait was obtained by visualizing the system motion within time interval about 5×10^5.

sharply grows. Exactly the two features has enabled us to classify the found effect as a phase transitions. It should be noted, that this phase transition from regular motion to stochastic chaos, in contrast to the second transition to highly irregular motion, does not manifest itself in the one-particle distributions of all the variables x, v, η, ϑ ascribed to the beads individually, so, it could be categorized as a "weak" phase transition.

4 Conclusion

The notion of dynamical traps was introduced to describe possible effects caused by the bounded capacity of human cognition in ordering events or actions according to their preference. Its particular implementation is that human beings as active elements of a certain system cannot individually control all the governing parameters within the accuracy required for stabilizing the system dynamics perfectly. Therefore one chooses a few crucial parameters and mainly focuses attention on them. When the equilibrium with respect to these crucial parameters is attained the human activity slows down, retarding in turn the system dynamics as a whole.

By way of example, we considered emergent phenomena in chains of coupled oscillators with dynamical traps. The motion of oscillating particles (beads) in the phase space $\{x_i, v_i = \dot{x}_i\}$ is assumed to be governed by their interaction via effective elastic springs with viscous friction outside the dynamical trap region $\mathbf{Q}_{\mathsf{tr}}$. For a given bead i the dynamical trap effect is reduced to depressing its interaction with the nearest neighbors $i-1$ and $i+1$ as the relative velocity

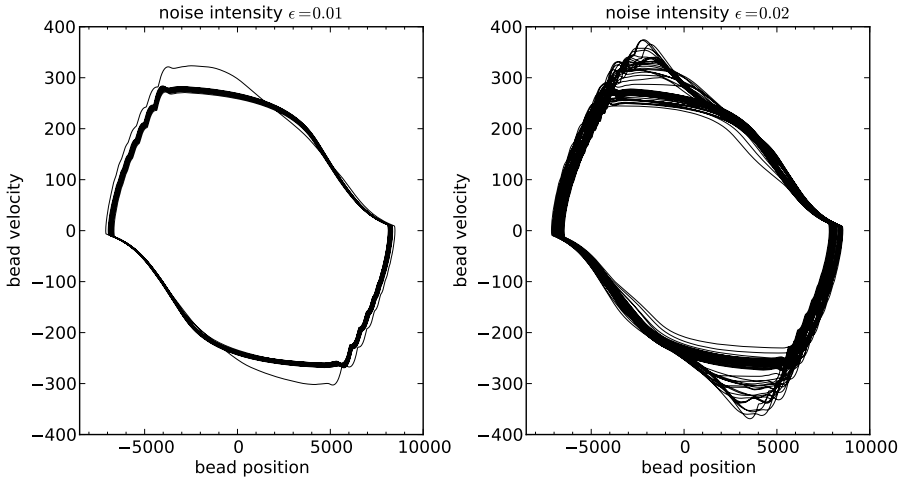

Fig. 4. The phase portraits of the middle bead motion of the 30-bead chain with $\sigma = 1$ for two values of the noise intensity $\epsilon = 0.01$ and 0.02. In plotting these portraits bead trajectories of motion during time interval about 2×10^4 were used.

$\vartheta_i = v_i - (v_{i-1} + v_{i+1})/2$ becomes small in comparison with some threshold. The introduction of additive white noise of intensity ϵ allows for possible uncontrollable factors also affecting the bead motion.

This system was studied numerically. As demonstrated, without noise the system dynamics tends to the regime of regular bead motion if the friction coefficient is not too small. However, the characteristic time required for a given system to get this regime grows exponentially with the number N of beads. It enables us to pose a question about regarding the chaotic transient processes as a certain phase state in the limit $N \to \infty$. When the friction coefficient becomes sufficiently small the steady state dynamics of such systems can undergo transition to chaotic bead motion even for chains with small number of beads. Depending on its intensity noise can induce the formation of three characteristic phases, highly irregular individual oscillations of the beads, the cooperative chaotic bead motion, and the synchronized regular bead motion. It should be noted that the transition between the regimes of regular and cooperative chaotic bead motion manifests itself only the sharp growth of the volume of the phase space layer containing the bead trajectories, whereas all the one-particle distribution functions does not change their forms remarkably.

Acknowledgments

The work was supported in part by the JSPS "Grants-in-Aid for Scientific Research" Program, Grant # 245404100001.

References

1.R. A. Meyers (ed), *Encyclopedia of Complexity and Systems Science*, Springer-Science+Buisiness Media, LLC., New York, 2009.
2.C. Castellano, S. Fortunato, and V. Loreto. Statistical physics of social dynamics. *Rev. Mod. Phys.*, 81:591–646, 2009.
3.F. Slanina. Social Processes, Physical Models of. In Ref. [1], pages 8379–8405.
4.D. Stauffer. Opinion Dynamics and Sociophysics. In Ref. [1], pages 6380–6388.
5.D. Helbing and A. Johansson. Pedestrian, Crowd and Evacuation Dynamics. In Ref. [1], pages 6476–6495.
6.A. Schadschneider, W. Klingsch, H. Klüpfel, T. Kretz, C. Rogsch, and A. Seyfried. Evacuation Dynamics: Empirical Results, Modeling and Applications. In Ref. [1], pages 3142–3176.
7.D. Helbing. Traffic and related self-driven many-particle systems. *Rev. Mod. Phys.*, 73:1067–1141, 2001.
8.G. Yaari, D. Stauffer, and S. Solomon. Intermittency and Localization, in Ref. [1], pages 4920–4930.
9.R. Hegselmann. Moral Dynamics, In Ref. [1], pages 5677–5692.
10.R. R. Vallacher. Social Psychology, Applications of Complexity to. In Ref. [1], pages 8420–8435
11.O. O. Olivier and J. A. S. Kelso. Social Coordination, from the Perspective of Coordination Dynamics. In Ref. [1], pages 8198–8213.
12.K. K. Dompere. *Fuzzy Rationality*, Springer-Verlag, Berlin, 2009.
13.I. A. Lubashevsky, R. Mahnke, M. Hajimahmoodzadeh, and A. Katsnelson. Long-lived states of oscillator chains with dynamical traps, *Eur. Phys. J. B*, 44:63–70, 2005.
14.I. Lubashevsky, M. Hajimahmoodzadeh, A. Katsnelson, and P. Wagner. Noise-induced phase transition in an oscillatory system with dynamical traps. *Eur. Phys. J. B*, 36:115–118, 2003.
15.A. Zgonnikov, I. Lubashevsky, and M. Mozgovoy. Computer simulation of stick balancing: action point analysis. In V. Klyuev and A. Vazhenin (eds), *Proceedings of the 2012 Joint International Conference on Human-Centered Computer Environments (HCCE'12)*, ACM New York, NY, USA, 2012, pages 162–164.
16.P. M. Burrage. *Numerical methods for stochastic differential equations*. Ph.D. thesis, University of Queensland, Brisbane, Queensland, Australia, 1999.
17.I. Lubashevsky. Dynamical traps caused by fuzzy rationality as a new emergence mechanism. Advances in Complex Systems, 15:1250045(1-25), 2012.

Chaotic Modeling and Simulation (CMSIM) 1: 39–50, 2013

Multifractals Tied to Extensions of Panjer's Iterative Procedures

Maria de Fátima Brilhante[1], Maria Ivette Gomes[2], and Dinis Pestana[3]

[1] Universidade dos Açores (DM) and CEAUL, Ponta Delgada, Portugal
(E-mail: fbrilhante@uac.pt)
[2] DEIO, FUL and CEAUL, Universidade de Lisboa, Lisboa, Portugal
(E-mail: ivette.gomes@fc.ul.pt)
[3] CEAUL — Centro de Estatística e Aplicações da Universidade de Lisboa, Lisboa, Portugal
(E-mail: dinis.pestana@fc.ul.pt)

Abstract. Binomial, Poisson and Negative Binomial are the basic count models whose probability mass function satisfies a simple recursive relation. This has been used by Panjer [8] to iteratively compute the density of randomly stopped sums, namely in the context of making provision for claims in insurance. Pestana and Velosa [9] used probability generating functions of randomly stopped sums whose subordinator is a member of Panjer's family to discuss more involved recursive relations, leading to refinements of infinite divisibility and self-decomposability in count models. After discussing multifractal measures generated by the geometric and by the Poisson laws, as guidelines to define multifractals generated by general count measures with denumerably infinite support, the complex recursivity of Pestana and Velosa [9] classes of randomly stopped sums is exhibited, hinting that randomness can bring in deeper meaning to multifractality, that, as Mandelbrot argues, is a vague concept that remains without an agreed mathematical definition. A simple random extension of binomial and multinomial multifractals, considering that each multiplier of a cascade is the outcome of some stochastic count model, is also discussed in depth.
Keywords: Count models, probability generating functions, multifractal measures, random multipliers.

1 Introduction

Simple introductory texts on multifractals, v.g. Ervertsz and Mandelbrot [2], use binary splitting and multiplicative cascades generating binomial measures as a straightforward and intuitive example. Mandelbrot [6] (p. 83–84 and 89–91) also uses the binomial measure to exhibit the complications that arise

Reviced: 4 November 2012 / Accepted: 18 January 2013

ISSN 2241-0503

when self-similarity and self-affinity are applied to measures rather than to sets, restricting the probability p to take values in the interval $[0, \frac{1}{2}]$.[1]

Ervertsz and Mandelbrot [2], under the heading "Beyond Multinomial Measure" (p. 937–938), briefly mention multifractal measures generated by a countably infinite support probability mass function. In Section 2 we detail the construction of such measures starting either from a geometric distribution or from a Poisson distribution.

On the other hand, Mandelbrot [6] (p. 14) states that "*the terms* fractal *and* multifractal *remain without an agreed mathematical definition*", although the fact that self-similarity, self-affinity and the ensuing mild or wild variability play an essential role in their theory. Binomial, negative binomial and Poisson count measures probability mass functions satisfy some sort of self-similarity, in the sense that $p_{n+1} = (a+\frac{b}{n+1})\, p_n,\ n = 0, 1, \ldots$, a recursive expression that has been successfully used by Panjer [8] to iteratively compute densities of randomly stopped sums whose subordinator is one of the above mentioned count models, and our first choice has been to exploit implications and extensions of this extended kind of self-similarity. Observe that the simplest cases are $N \frown Poisson(b)$ for $a = 0$ and $N \frown Geometric(1-a)$ for $b = 0$, leading to simple forms of extended self-similarity, and that for this reason are the topic of Section 2.

In Section 3 we briefly mention the basic count models whose probability mass function satisfies some sort of mitigated self-similarity, extending Panjer's [8] class, and we use probability generating functions investigated in [9] to discuss multiple self-similarity, extending results in [1].

In Section 4 we discuss other pathways to multifractality, extending the construction of binomial/multinomial measures to accommodate the case of countably infinite support discrete generators, using randomness as a device to operate this alternative extension of multifractality.

[1] In fact, for $p = 1/2$ the procedure leads to the uniform measure in (0,1), a straightforward consequence of the binary representation of real numbers in the interval (0,1)

$$\sum_{k=1}^{\infty} \frac{X_k}{2^k}, \quad X_k \frown Bernoulli\left(\frac{1}{2}\right), \text{ independent}$$

and of Borel's pioneering construction of continuous probability. As Mandelbrot [6] (p. 45) states, "*The definition of multifractality used in this book and almost everywhere else in the literature* [...] *is limited to singular non-negative measures constructed using continuous non-decreasing generators.*"

Feller [3] (p. 141–142), on the same issue, denoting F_p the distribution of

$$Y_p = \sum_{k=1}^{\infty} \frac{X_k}{2^k}, \quad \text{where} \quad X_k \frown Bernoulli(p), \text{ independent},$$

observes that $Y_{\frac{1}{2}}$ is the standard uniform random variable, and that Y_p is a singular random variable for each $p \neq 1/2$. He further comments that "*A little reflection* [...] *reveals that a decision* [on the fairness of a coin] *after finitely many trials is due to the fact that* F_p *is singular with respect to* $F_{\frac{1}{2}}$ *(provided* $p \neq 1/2$*). The existence of singular distributions is therefore essential to statistical practice.*"

2 Geometric and Poisson generated measures

Let $X \frown Exponential\,(1/\delta)$, and define the countably discrete random variable

$$N = \begin{cases} k = 0, 1, \dots \\ p_k = \mathbb{P}[N = k] = \mathbb{P}[k \le X < k + 1] = (1 - \mathrm{e}^{-\delta})(\mathrm{e}^{-\delta})^k \end{cases}$$

i.e., $N = \lfloor X \rfloor \frown Geometric(1 - \mathrm{e}^{-\delta})$ ($\lfloor x \rfloor$ denotes the integer part of x).

On the other hand, from the probability integral transform,

$$1 - \mathrm{e}^{-\delta X} \stackrel{\mathrm{d}}{=} \mathrm{e}^{-\delta X} \stackrel{\mathrm{d}}{=} U \frown Uniform[0, 1].$$

Thus, starting from the interval [0,1], in the first step [0,1] is splitted in countably many subintervals,

$$[0, 1] = \bigcup_{k=0}^{\infty} \left(\mathrm{e}^{-(k+1)}, \mathrm{e}^{-k}\right] = \bigcup_{k=0}^{\infty} \mathcal{I}_{k(1)}$$

to which we attach probabilities $m_k = (1 - \mathrm{e}^{-\delta})(\mathrm{e}^{-\delta})^k,\ k = 0, 1, \dots$.

In step 2, each $\mathcal{I}_k$ is treated as a reduction of the original [0,1] interval, i.e., using self-explaining standard notations for the translation and scaling of sets,

$$\mathcal{I}_{k(1)} = \bigcup_{j=0}^{\infty} \left\{\mathrm{e}^{-(k+1)} + \left(\mathrm{e}^{-k} - \mathrm{e}^{-(k+1)}\right)\left(\mathrm{e}^{-(j+1)}, \mathrm{e}^{-j}\right]\right\} = \bigcup_{j=0}^{\infty} \mathcal{I}_{j_k(2)},$$

so that $[0, 1] = \bigcup_{k=0}^{\infty}\Big(\bigcup_{j=0}^{\infty} \mathcal{I}_{j_k(2)}\Big)$, and to each interval $\mathcal{I}_{j_k(2)}$ we attach the probability $m_k m_j$.

In step 3, the subintervals $\mathcal{I}_{j_k(2)}$ are treated as the $\mathcal{I}_k$ intervals in step 2, and similarly in the countably infinite steps that follow to build up a multifractal generated by a Geometric initial measure. Notations soon become cumbersome, but the principles used in the build up of the multiplicative cascade $m_{k_1} m_{k_2} \cdots$ are simple. In Figure 1 we show the initial four steps of the construction of the geometric measure with the parameter $1 - e^{-1}$.

The procedure described above is intuitive in view of the geometric discretization of the exponential measure, but it can in fact be used with an initial generator whose support is $\mathbb{N}$, namely $N \frown Poisson(\lambda)$.

$N_G \frown Geometric(p)$ may be looked at as the "unit" of the class of $Negative\ Binomial(r, p)$ random variables, in the same sense that $N_B \frown Bernoulli(p)$ is the unit of $Binomial(n, p)$ random variables. On the other hand the sum of independent Poisson random variables is Poisson, and hence we may consider that $N_P \frown Poisson(1)$ is the unit of the class of $Poisson(\lambda)$ random variables. Observe also that the Poisson is a yardstick in the perspective of dispersion, since its dispersion index $\mathrm{Var}[N_P]/\mathbb{E}[N_P] = 1$, while $Binomial(n, p)$ random variables are underdispersed and $NegativeBinomal(r, p)$ random variables are overdispersed.

Fig. 1. Construction of the geometric measure with parameter $1 - a = 0.63$ (i.e. $\delta = 1$) — the initial four steps

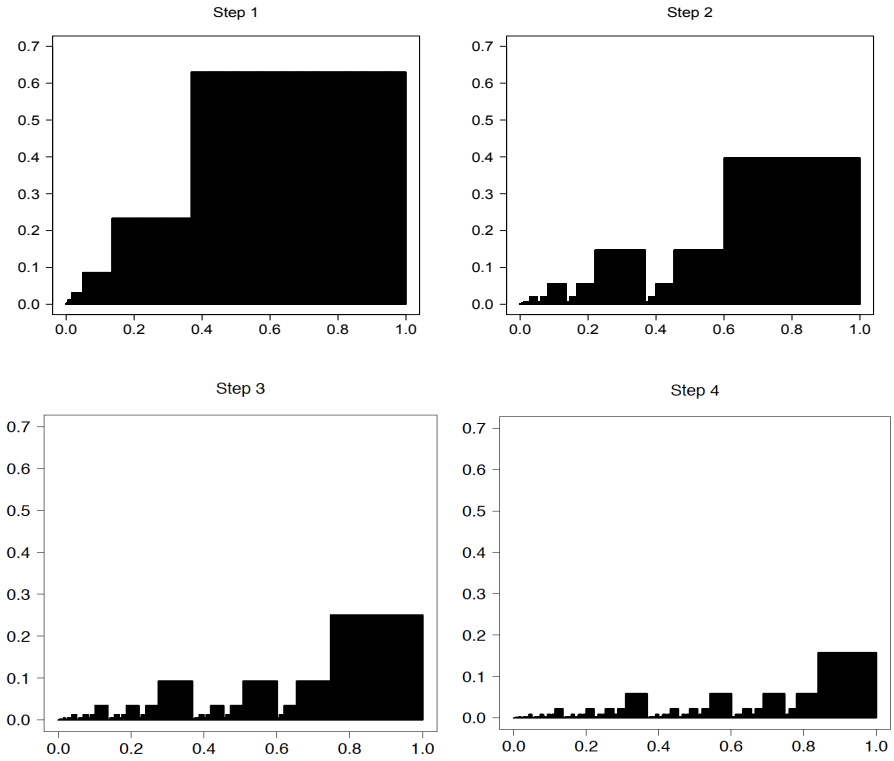

Observe also that Binomials, Poissons and NegativeBinomials are the only discrete classes of natural exponential families whose variance is at most a quadratic function of the mean value (Morris [7]), who writes "*Much theory is unified for these* [...] *natural exponential families by appeal to their quadratic variance property, including* [...] *large deviations*", one of the tools routinely used to investigate dimensionality issues in multifractals. Without pursuing the matter further herein, we remark that a differential simile of Panjer's difference iteration is $f'/f = a + b/x$, where f denotes the density function of a positive absolutely continuous random variable, and hence f must be the density of a $Gamma(b+1, -\frac{1}{a})$ random variable, for $b > -1$ and $a < 0$. The gamma random variables are the sole Morris continuous random variables with positive support.

3 Extended self-similarity of basic count models

Let

$$N = \begin{cases} k = 0, 1, 2, \dots \\ \\ p_k = \mathbb{P}[N = k] \end{cases}$$

be a count random variable. Panjer [8] made an important breakthrough in insurance theory by showing that the only non-degenerate random variables whose probability mass function satisfies the recurrence relation

$$p_{n+1} = p_n \left(\alpha + \frac{\beta}{n+1} \right), \ n = 0, 1, \dots$$

are the Poissons, the Binomals and the Negative Binomials, and that the above recurrence relation can be used to deduce an iterative procedure to compute the density of randomly stopped sums

$$\sum_{k=0}^{N} X_k, \ X_k \text{ independent random variables, independent of } N,$$

often used as models for aggregate claims, cf. [5] or [10]. Further generalizations may be constructed relaxing the iterative expression to hold for $n \geq k_0$, see Hess *et al.* [4] construction of what they call basic count models.

A further generalization can be developed as follows:

Consider discrete random variables $N_{\alpha,\,\beta,\,\gamma}$ whose probability mass functions (p.m.f.) $\left\{p_n = f_{N_{\alpha,\,\beta,\,\gamma}}(n)\right\}_{n\in\mathbb{N}}$ satisfy the relation

$$\frac{f_{N_{\alpha,\,\beta,\,\gamma}}(n+1)}{f_{N_{\alpha,\,\beta,\,\gamma}}(n)} = \alpha + \beta \, \frac{\mathbb{E}(U_0^n)}{\mathbb{E}(U_\gamma^n)} = \alpha + \frac{\beta}{\sum_{k=0}^{n} \gamma^k}, \ \alpha, \, \beta \in \mathbb{R}, \ n = 0, 1, \dots$$

where $U_\gamma \frown Uniform(\gamma, 1), \ \gamma \in (-1, 1)$. As

$$\mathbb{E}(U_\gamma^n) = \frac{1}{n+1} \frac{1-\gamma^{n+1}}{1-\gamma} \underset{\gamma\to 1}{\longrightarrow} 1,$$

Panjer's class corresponds to the degenerate limit case, letting $\gamma \longrightarrow 1$ so that $U_\gamma \underset{\gamma\to 1}{\longrightarrow} U_1$, the degenerate random variable with unit mass at 1.

The probability generating function $\mathcal{G}_{\alpha,\,\beta,\,\gamma}(s) = \sum_{n=0}^{\infty} f_{N_{\alpha,\,\beta,\,\gamma}}(n)\, s^n$ must then satisfy

$$\mathcal{G}_{\alpha,\,\beta,\,\gamma}(s) = \mathcal{G}_{\alpha,\,\beta,\,\gamma}(\gamma^{n+1}s) \prod_{k=0}^{n} \frac{1-\alpha\gamma^{k+1}s}{1-[\alpha+\beta(1-\gamma)]\gamma^k s}.$$

Observing that

$$\frac{\mathcal{G}_{\alpha,\,\beta,\,\gamma}(s)}{\mathcal{G}_{\alpha,\,\beta,\,\gamma}(1)} = \frac{\mathcal{G}_{\alpha,\,\beta,\,\gamma}(\gamma^{n+1}s)}{\mathcal{G}_{\alpha,\,\beta,\,\gamma}(\gamma^{n+1})} \prod_{k=0}^{n} \frac{\frac{1-\alpha\gamma^{k+1}s}{1-[\alpha+\beta(1-\gamma)]\gamma^k s}}{\frac{1-\alpha\gamma^{k+1}}{1-[\alpha+\beta(1-\gamma)]\gamma^k}},$$

and letting $n \to \infty$,

$$\mathcal{G}_{\alpha,\beta,\gamma}(s) = \prod_{k=0}^{\infty} \frac{1-\alpha\gamma^{k+1}s}{1-\alpha\gamma^{k+1}} \, \frac{1-[\alpha+\beta(1-\gamma)]\gamma^k}{1-[\alpha+\beta(1-\gamma)]\gamma^k s} \, . \tag{1}$$

If $\gamma \in [0,1)$, $\alpha < 0$ and $\beta \in \left\{-\frac{\alpha}{1-\gamma}, \, \frac{1-\alpha}{1-\gamma}\right\}$, we recognize in (1) the probability generating function of an infinite sum of independent random variables, the k-th summand being the result of randomly adding 1, with probability $\alpha\gamma^{k+1}/\big(\alpha\gamma^{k+1}-1\big)$, to an independent $Geometric(1-[\alpha+\beta(1-\gamma)]\gamma^k)$ random variable. Each summand exhibits its own scale of extended self-similarity, a characteristic feature observed, in what concerns self-similarity and self-affinity, in strict sense (in Madelbrot's perspective) multifractals.

The limiting case $\gamma = 1$ may be approached as follows: observing that

$$\frac{\mathcal{G}_{\alpha,\beta,\gamma}(s) - \mathcal{G}_{\alpha,\beta,\gamma}(\gamma s)}{\alpha s[\mathcal{G}_{\alpha,\beta,\gamma}(s) - \mathcal{G}_{\alpha,\beta,\gamma}(\gamma s)] + (1-\gamma)s[\beta\mathcal{G}_{\alpha,\beta,\gamma}(s) + \alpha\mathcal{G}_{\alpha,\beta,\gamma}(\gamma s)]} = 1,$$

dividing the numerator and the denominator by $(1-\gamma)s$ and letting $\gamma \to 1$, we get

$$\frac{\mathcal{G}'_{\alpha,\beta,1}(s)}{\alpha s\mathcal{G}'_{\alpha,\beta,1}(s) + \beta\mathcal{G}_{\alpha,\beta,1}(s) + \alpha\mathcal{G}_{\alpha,\beta,1}(s)} = 1 \Longleftrightarrow \frac{\mathcal{G}'_{\alpha,\beta,1}(s)}{\mathcal{G}_{\alpha,\beta,1}(s)} = \frac{\alpha+\beta}{1-\alpha s},$$

the expression we obtain working out the probability generating function in Panjer's iterative expression

$$p_{\alpha,\beta}(n+1) = \left(\alpha + \frac{\beta}{n+1}\right) p_{\alpha,\beta}(n), \quad \alpha, \, \beta \in \mathbb{R}, \; n = 0, 1, \ldots \, .$$

So, while Panjer's recurrence relation and Hess *et al.* extension for the basic count models exhibit a single scaling, (1) exhibits multi-scaling as typical of multifractals.

4 A simple generalization of the binomial/multinomial measure

There are many pathways to expand the notion of a multiplicative cascade. One is to consider that each multiplier is the outcome of some stochastic rule. These kind of multiplicative iterative schemes are usually called random multiplicative cascades.

In Section 2 we introduced the geometric and Poisson generated measures. In this section we shall expand differently the notion of random multiplicative cascades by allowing the number of subdivisions that each interval undergoes, at each step of the measure construction, to be determined by the outcome of a discrete random variable N, where $\mathbb{P}[N \geq 2] = 1$. This procedure has some similar aspects with the binomial and multinomial measures. However, at step k, $k = 1, 2, \ldots$, the outcome of N will dictate the number of subdivisions that

each interval suffers. In this new scenario the multipliers used at each step will also depend on the outcome of N, i.e., $m_i = m_i^{(N)}$.

Starting with the interval [0,1], having uniformly distributed unit mass, the new measure is formally constructed as follows:

Step 1: Generate an observation n_1 from the random variable N. Split the interval [0,1] into the n_1 equally length subintervals

$$[in_1^{-1}, (i+1)n_1^{-1}], \quad i = 0, 1, \ldots, n_1 - 1, \tag{2}$$

with uniformly distributed masses $m_i^{(n_1)}$, $i = 0, 1, \ldots, n_1 - 1$, respectively;

Step 2: Generate a second observation n_2 from N, independent from n_1. Split each interval in (2) into n_2 equally length subintervals and use the multipliers $m_i^{(n_2)}$, $i = 0, 1, \ldots, n_2 - 1$, to uniformly distribute the parent interval's mass by these subintervals. After this step is completed the subintervals formed are $[i(n_1n_2)^{-1}, (i+1)(n_1n_2)^{-1}]$, $i = 0, 1, \ldots, n_1n_2 - 1$;

Step *k*: Generate an observation n_k from N, independent from the previous $k-1$ observations of N. Split each interval from the previous step into n_k subintervals of equal length and use the multipliers $m_i^{(n_k)}$, $i = 0, 1, \ldots, n_k - 1$, to uniformly distribute the parent interval's mass by these subintervals. The subintervals formed after this step are $[i(n_1n_2 \ldots n_k)^{-1}, (i+1)(n_1n_2 \ldots n_k)^{-1}]$, $i = 0, 1, \ldots, n_1n_2 \ldots n_k - 1$.

The new measure μ results from applying the previous procedure infinitely.

An example of a family of multipliers that can be used in this type of measure construction is

$$m_i^{(n)} = \frac{2(i+1)}{n(n+1)} \quad i = 0, 1, \ldots, n-1\,, \tag{3}$$

when $N = n$. (Note that with the multipliers defined in (3) we do not get $m_0 = m_1 = 1/2$ if $N = 2$ is observed.)

In order to illustrate how the measure is obtained we give a simple example. Suppose that the random variable N has support on $\{2, 3\}$ with p.m.f. $\mathbb{P}[N = 2] = 1/4$ and $\mathbb{P}[N = 3] = 3/4$. Let us further assume that we observe for the first two steps of the measure's construction the sequence of divisors $(N_1, N_2) = (3, 2)$, where N_1 and N_2 are independent replicas of N. Using the multipliers defined in (3), we get

$$m_0^{(2)} = \frac{1}{3} \quad \text{and} \quad m_1^{(2)} = \frac{2}{3}\,,$$

and

$$m_0^{(3)} = \frac{1}{6}, \quad m_1^{(3)} = \frac{1}{3} \quad \text{and} \quad m_2^{(3)} = \frac{1}{2}.$$

At step one we obtain the subintervals $[0, \frac{1}{3}]$, $[\frac{1}{3}, \frac{2}{3}]$ and $[\frac{2}{3}, 1]$, with masses 1/6, 1/3 and 1/2, respectively, and after step two the subintervals $[0, \frac{1}{6}]$, $[\frac{1}{6}, \frac{1}{3}]$, $[\frac{1}{3}, \frac{1}{2}]$, $[\frac{1}{2}, \frac{2}{3}]$, $[\frac{2}{3}, \frac{5}{6}]$ and $[\frac{5}{6}, 1]$, with masses 1/18, 1/9, 1/9, 2/9, 1/6 and 1/3, respectively. We should point out that when a measure of this type is being formed,

one actually does not know which generator sequence of divisors $(N_1, N_2, \dots)$ is being used in the construction, and consequently which multipliers are being used at each step.

In Figure 2 we show the measure obtained after 10 steps for two different generator sequences, when working with the above random variable N. The patterns clearly reveal that the first divisor was 2 in the left plot and 3 in the right plot. In Figure 3 we show the effect of some permutations of a sequence of divisors of length 10 on the measure's construction (note that in this case there are a total of $2^{10} = 1024$ possible permutations for the sequence of digits). As we can see all four plots have different patterns.

Fig. 2. The measure obtained after 10 steps for two different generator sequences

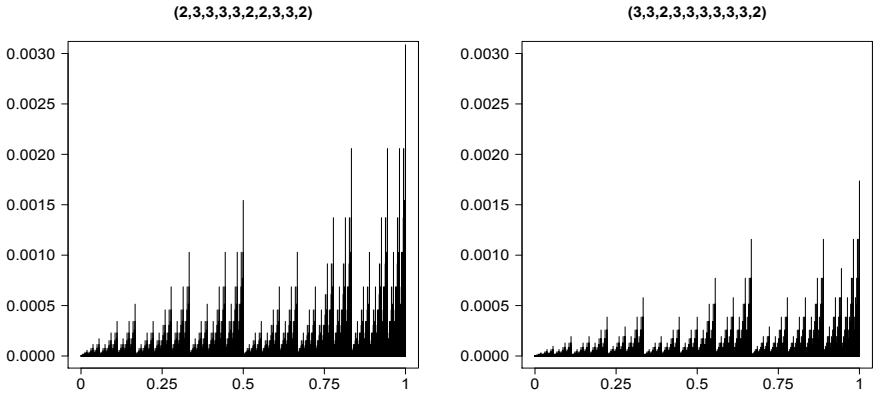

In the binomial and multinomial measures the multipliers used throughout all steps are fixed in value and in number. In this new scenario each multiplier should be regarded as a random variable, since the magnitude and number of the multipliers used are directly determined by the distribution of N.

Let us go back to the example to see how this is the case. For the multipliers defined in (3) we can have $m_0 = 1/3$ or $m_0 = 1/6$, with probability $1/4$ and $3/4$, respectively, and for this example there are 3 random multipliers that need to be defined. If M_i denotes the random variable that represents the value of the i-th random multiplier,

$$M_0 = \begin{cases} \frac{1}{3} & \frac{1}{6} \\ \frac{1}{4} & \frac{3}{4} \end{cases}, \quad M_1 = \begin{cases} \frac{2}{3} & \frac{1}{3} \\ \frac{1}{4} & \frac{3}{4} \end{cases} \quad \text{and} \quad M_2 = \begin{cases} 0 & \frac{1}{2} \\ \frac{1}{4} & \frac{3}{4} \end{cases}. \tag{4}$$

The expected values for the multipliers given in (4) are $\mathbb{E}[M_0] = 5/24$, $\mathbb{E}[M_1] = 5/12$ and $\mathbb{E}[M_2] = 3/8$. For an arbitrarily random variable N, the number of random multipliers M_i will depend on the number of points where N has non null mass.

Fig. 3. The measure obtained after 10 steps for four different permutations of a generator sequence

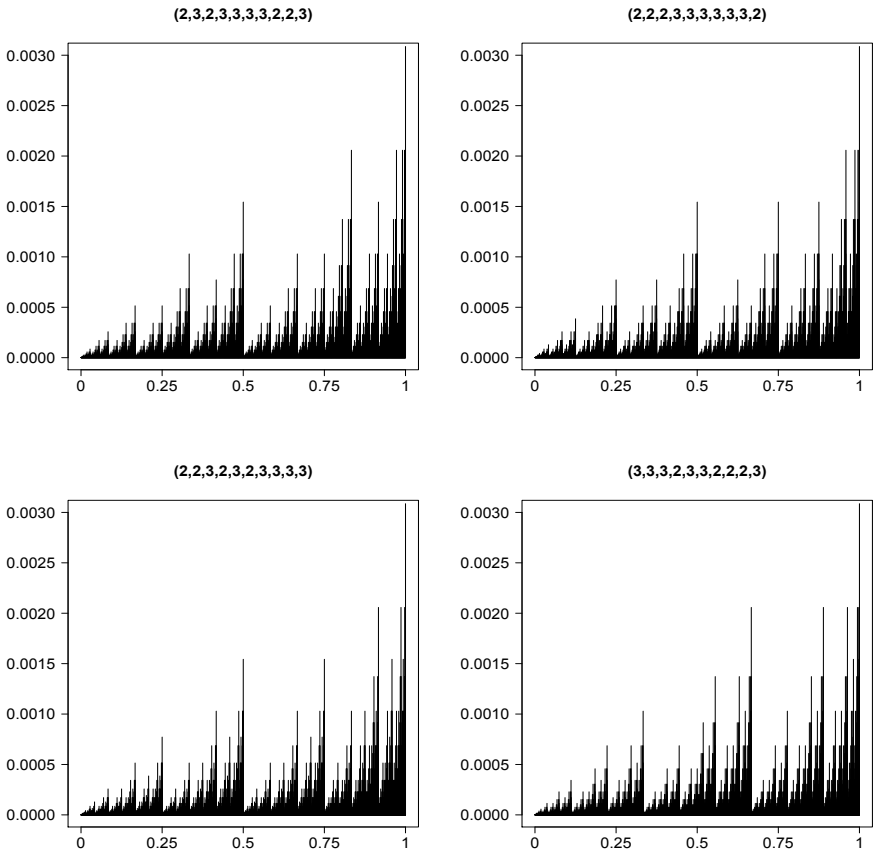

In each step of this new multiplicative cascade we can also attach an address (location) to each interval generated, as is done in the binomial and multinomial measures (for more details on this subject see e.g. Ervertsz and Mandelbrot [2]). However, given the way the measure is constructed, we can have different intervals for the same address. In order to illustrate this situation we indicate in Table 1 the intervals and corresponding addresses and masses for the first two steps of all possible cases for (N_1, N_2) (in brackets we indicate the probability of observing each sequence of length 2).

From Table 1 we observe that there is no one-to-one correspondence between address and interval, contrarily to what happens with the binomial and multinomial measures. We also observe that intervals with the same address do not have necessarily the same mass. Thus the definitions of coarse and local

Table 1. Intervals, addresses and masses for all possible sequences (N_1, N_2)

	$(N_1,N_2)=(2,2)\quad(\frac{1}{16})$			
Interval	$[0,\frac{1}{4}]$	$[\frac{1}{4},\frac{1}{2}]$	$[\frac{1}{2},\frac{3}{4}]$	$[\frac{3}{4},1]$
Address	0.00	0.01	0.10	0.11
$\boldsymbol{\mu}$	1/9	2/9	2/9	4/9

	$(N_1,N_2)=(2,3)\quad(\frac{3}{16})$					
Interval	$[0,\frac{1}{6}]$	$[\frac{1}{6},\frac{1}{3}]$	$[\frac{1}{3},\frac{1}{2}]$	$[\frac{1}{2},\frac{2}{3}]$	$[\frac{2}{3},\frac{5}{6}]$	$[\frac{5}{6},1]$
Address	0.00	0.01	0.02	0.10	0.11	0.12
$\boldsymbol{\mu}$	1/18	1/9	1/6	1/9	2/9	1/3

	$(N_1,N_2)=(3,2)\quad(\frac{3}{16})$					
Interval	$[0,\frac{1}{6}]$	$[\frac{1}{6},\frac{1}{3}]$	$[\frac{1}{3},\frac{1}{2}]$	$[\frac{1}{2},\frac{2}{3}]$	$[\frac{2}{3},\frac{5}{6}]$	$[\frac{5}{6},1]$
Address	0.00	0.01	0.10	0.11	0.20	0.21
$\boldsymbol{\mu}$	1/18	1/9	1/9	2/9	1/6	1/3

	$(N_1,N_2)=(3,3)\quad(\frac{9}{16})$								
Interval	$[0,\frac{1}{9}]$	$[\frac{1}{9},\frac{2}{9}]$	$[\frac{2}{9},\frac{1}{3}]$	$[\frac{1}{3},\frac{4}{9}]$	$[\frac{4}{9},\frac{5}{9}]$	$[\frac{5}{9},\frac{2}{3}]$	$[\frac{2}{3},\frac{7}{9}]$	$[\frac{7}{9},\frac{8}{9}]$	$[\frac{8}{9},1]$
Address	0.00	0.01	0.02	0.10	0.11	0.12	0.20	0.21	0.22
$\boldsymbol{\mu}$	1/36	1/18	1/12	1/18	1/9	1/6	1/12	1/6	1/4

Hölder exponents given in the literature can not be applied directly to this type of measure.

We recall that the coarse Hölder exponent is defined as

$$\alpha_k(x) = \frac{\log(\mu(\mathrm{I}_{0.\beta_1\beta_2\ldots\beta_k}))}{\log\epsilon}\,, \quad k=1,2,\ldots, \tag{5}$$

where $\mu(\mathrm{I}_{0.\beta_1\beta_2\ldots\beta_k})$ indicates the measure of the interval $x=\mathrm{I}_{0.\beta_1\beta_2\ldots\beta_k}$ having address $0.\beta_1\beta_2\ldots\beta_k$ and size (length) ϵ, with $\beta_i=0,1,\ldots,b-1$ and $b\geq 2$. On the other hand, the local Hölder exponent is defined as

$$\alpha(x) = \lim_{k\to\infty}\alpha_k(x) \tag{6}$$

(i.e. for $\epsilon\to 0$), if the limit exists.

However, expressions (5) and (6) can be generalized to accommodate this new measure. All we have to do is to consider that the measure associated with an address is the mean value of the masses of the intervals which can have the address. This becomes clearer by examining Table 2 for the working example. It is also clear from Table 2 that addresses that are permutations of one another have the same mean mass (this remains true at any step).

The question now is how to determine the measure of a particular address $0.\beta_1\beta_2\ldots\beta_k$, $\beta_i=0,1,\ldots$, $i=1,2,\ldots,k$, which can have a multitude

Table 2. Masses for all possible addresses obtained after 2 steps

Address	(2,2)	(2,3)	(3,2)	(3,3)	Mean mass
0.00	1/9	1/18	1/18	1/36	25/576
0.01	2/9	1/9	1/9	1/18	25/288
0.10	2/9	1/9	1/9	1/18	25/288
0.11	4/9	2/9	2/9	1/9	25/144
0.02	0	1/6	0	1/12	5/64
0.20	0	0	1/6	1/12	5/64
0.12	0	1/3	0	1/6	5/32
0.21	0	0	1/3	1/6	5/32
0.22	0	0	0	1/4	9/64

of intervals attached to it, if one does not know which generator sequence $(N_1, N_2, \ldots, N_k)$ was used? As Table 2 suggests, we use the random multipliers expectations. We can prove that the address $0.\beta_1\beta_2\ldots\beta_k$ has expected measure

$$\mu_E(0.\beta_1\beta_2\ldots\beta_k) = \mathbb{E}(M_{\beta_1})\mathbb{E}(M_{\beta_2})\ldots\mathbb{E}(M_{\beta_k}),$$

which does not depend on the generator sequence. We remark that the only kind of dependence that exists between the generator sequence and the expected measure is through the influence of N on the random multipliers M_i. For example, both addresses 0.01 and 0.10 have expected measure $\mathbb{E}(M_0)\mathbb{E}(M_1) = 25/288$.

The generalization of the definitions (5) and (6) to this new measure is now straightforward. For the generalized coarse Hölder exponent we have

$$\alpha_k(0.\beta_1\beta_2\ldots\beta_k) = \frac{\log(\mu_E(0.\beta_1\beta_2\ldots\beta_k))}{\log\left(\mathbb{E}\left[\left(\prod_{i=1}^k N_i\right)^{-1}\right]\right)} \approx -\frac{\log(\mu_E(0.\beta_1\beta_2\ldots\beta_k))}{k\log(\mathbb{E}[N])}$$

and for the generalized local Hölder exponent,

$$\alpha = \lim_{k\to\infty} \alpha_k(0.\beta_1\beta_2\ldots\beta_k) \approx -\lim_{k\to\infty} \frac{\log(\mu_E(0.\beta_1\beta_2\ldots\beta_k))}{k\log(\mathbb{E}[N])},$$

if the limit exists. Note that $\left(\prod_{i=1}^k N_i\right)^{-1}$ represents the (random) length of the intervals at step k.

On the other hand, if at step k we randomly select an address $0.\beta_1\beta_2\ldots\beta_k$,

$$\mathbb{P}[\beta_i = j | N = n] = \frac{1}{n}, \quad j = 0, 1, \ldots, n-1,$$

and from applying the law of total probability, it follows that

$$\mathbb{P}[\beta_i = j] = \sum_{n=2}^{\infty} \mathbb{P}[\beta_i = j | N = n]\mathbb{P}[N = n], \quad j = 0, 1, \ldots . \tag{7}$$

Therefore, randomly selecting an address in this case corresponds to generating a sequence $\beta_1\beta_2 \ldots \beta_k$, where the β_i's satisfy (7). Considering again the example, we get $\mathbb{P}[\beta_i = 0] = \mathbb{P}[\beta_i = 1] = 3/8$ and $\mathbb{P}[\beta_i = 2] = 1/4$.

References

1. Brilhante, M. F., Gomes, M. I., and Pestana, D., Extension of Panjer's iterative procedures and multifractals. In C. Skiadas, ed., *Proceedings, 5th Chaotic Modeling and Simulation International Conference*, pages 123–130, 2012.
2. Ervertsz, C. J. G., and Mandelbrot, B. Multifractal Measures. In H.-O. Peitgen, H. Jürgens, and D. Saupe. *Chaos and Fractals: New Frontiers of Science*, pages 921–969, New York, 1993, Springer Verlag.
3. Feller, W. *An Introduction to Probability Theory and its Applications*, vol. II, 2nd ed., New York, 1971, Wiley.
4. Hess, K. Th., Lewald, A., and Schmidt, K. D., An extension of Panjer's recursion, *ASTIN Bulletin* 32:283–297, 2002.
5. Klugman, S. A., Panjer, H. H., and Willmot, G. E., *Loss Models: From Data to Decisions*, Wiley, New York, 1998.
6. Mandelbrot, B. *Multifractals and* $1/f$ *Noise; Wild Self-Affinity in Physics*, New York, 1999, Springer Verlag.
7. Morris, C. N., Natural Exponential Families with Quadratic Variance Functions, *Ann. Statist.* 10:65-80, 1982.
8. Panjer, H. H. Recursive evaluation of a family of compound distributions, *ASTIN Bulletin*, 12:22–26, 1981.
9. Pestana, D., and Velosa, S. Extensions of Katz-Panjer families of discrete distributions, *REVSTAT* 2:145-162, 2004.
10. Rólski, T., Schmidli, H., Schmidt, V., and Teugels, J., *Stochastic Processes for Insurance and Finance*, Wiley, New York, 1999.

FCT *This research has been supported by National Funds through FCT — Fundação para a Ciência e a Tecnologia, project PEst-OE/MAT/UI0006/2011.*

Chaotic Modeling and Simulation (CMSIM) 1: 51–57, 2013

Can the multifractal spectrum be used as a diagnostic tool?

K. P. Harikrishnan[1], R. Misra[2], and G. Ambika[3]

[1] Department of Physics, The Cochin College, Cochin - 682 002, India
(E-mail: *kp_hk2002@yahoo.co.in*)
[2] Inter University Centre for Astronomy and Astrophysics, Pune - 411 007
(E-mail: `rmisra@iucaa.ernet.in`)
[3] Indian Institute of Science Education and Research, Pune - 411 021, India
(E-mail: `g.ambika@iiserpune.ac.in`)

Abstract. We seek the possibility of using multifractal spectrum as a diagnostic tool to differentiate between healthy and pathological time series. The data sets used for the analysis consist of EEG and Heart Rate Variability (HRV) time seres downloaded from Physio Bank archives. We use the automated algorithmic scheme recently proposed by us to compute the multifractal spectrum, which provides a set of parameters to compare different data sets. We show that the set of parameters characterising the multifractal spectrum can distinguish between healthy and pathological states in both EEG and HRV.
Keywords: Time Series Analysis, Physiological Chaos, Multifractal Spectrum.

1 Introduction

Recently, many authors [1,2] have stressed the importance of multifractality in the study of heart rate variability and suggested that it could provide a new observational window into the complexity mechanism of heart rate control. The study also highlights the need for evaluating new nonlinear parameters for a better physiologcal investigation and for finding new clinical applications. The main issues regarding the characterisation of complex physiological signals are discussed in a recent review [3].

Out of the large number of studies done on physiological data, the focus has mainly been on the analysis of EEG and ECG time series data, with the purpose of characterisation and prediction from a dynamical systems point of view. The analysis of EEG data from healthy persons and epiletic patients has lead to a better understanding of various aspects of epileptic seizure activities and the corresponding brain states [4,5], but the question of whether the seizure can be predicted in advance is still an open one [6].

There have been a multitude of studies on ECG data sets recorded from healthy persons as well as during some pathological cases, such as, congestive

Received: 4 March 2012 / Accepted: 30 September 2012

ISSN 2241-0503

heart disorders and ventricular fibrillation [7–9]. Most of these studies have searched for deterministic nonlinearity in the time series from cardiac system [10,11], and the reliability of these results have also been questioned [12–14] due to various reasons, such as, insufficient data, presence of noise, the subjective nature of the computational techniques and so on.

In this paper, we present some preliminary results for the analysis of physiological data, by computing the $f(\alpha)$ spectrum from the time series using an automated algorithmic scheme. The details of the scheme are presented and tested in the next section and it is applied to physiological data in §3. The conclusions are drawn in §4.

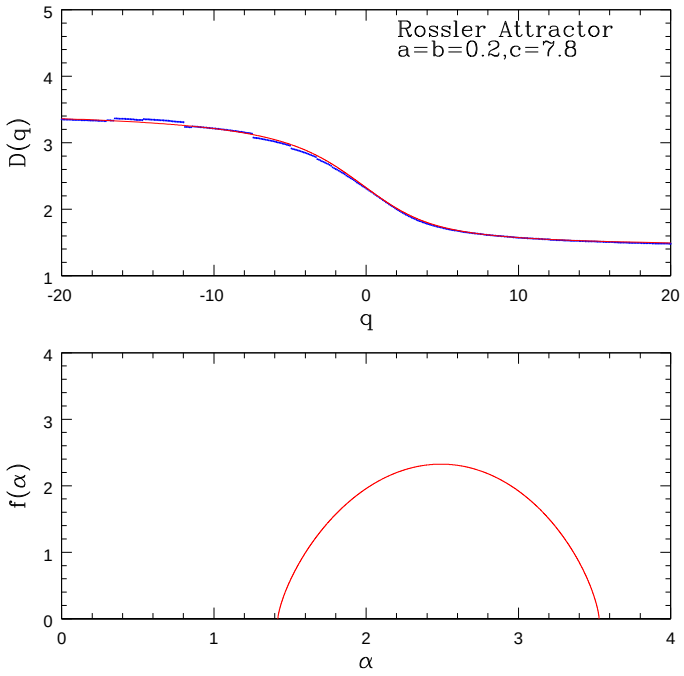

Fig. 1. The D_q spectrum (points) and its best fit curve (continuous line) for the Rossler attractor computed from 10000 data points are shown in the upper panel. The lower panel shows the $f(\alpha)$ spectrum computed from the best fit curve using our scheme.

2 Computing the Multifractal Spectrum

Here we discuss only the salient features of the algorithmic scheme and more mathematical details are presented elsewhere [15], [16]. The scheme provides us with a set of parameters characterising the spectrum which are good quantifiers to compare the changes in the multifractal character as reflected in the time series.

As the first step, the spectrum of generalised dimensions D_q is computed from the time series using the equation

$$D_q \equiv \frac{1}{q-1} \lim_{R\to 0} \frac{\log\ C_q(R)}{\log\ R} \tag{1}$$

where $C_q(R)$ are the generalised correlation sum. This is done by choosing the scaling region algorithmically as discussed earlier [16]. We make the conditions for R_{max} and R_{min} fixed by the algorithm itself so that the comparison between data sets becomes nonsubjective.

We then use an entirely different algorithmic approach for the computation of the smooth profile of the $f(\alpha)$ spectrum. The $f(\alpha)$ function is a single valued function between α_{max} and α_{min} and also has to satisfy several other conditions, such as, it has a single maximum and $f(\alpha_{max}) = f(\alpha_{min}) = 0$. A simple function that can satisfy all the necessary conditions is

$$f(\alpha) = A(\alpha - \alpha_{min})^{\gamma_1}(\alpha_{max} - \alpha)^{\gamma_2} \tag{2}$$

where A, γ_1, γ_2, α_{min} and α_{max} are a set of parameters characterising a particular $f(\alpha)$ curve. It can be shown [16] that only four of these parameters are independent and any general $f(\alpha)$ curve can be fixed by four independent parameters. Moreover, by imposing the conditions on the $f(\alpha)$ curve, it can also be shown that

$$0 < \gamma_1, \gamma_2 < 1 \tag{3}$$

The scheme first takes $\alpha_1(\equiv D_1), \alpha_{min}(\equiv D_\infty)$ and $\alpha_{max}(\equiv D_{-\infty})$ as input parameters from the computed D_q values and choosing an initial value for γ_1 in the range $[0, 1]$, the parameters γ_2 and A are calculated. The $f(\alpha)$ curve is then computed in the range $[\alpha_{min}, \alpha_{max}]$. From this, a smooth D_q versus q curve can be obtained by inverting using the Legendre transformation equations, which is then fitted to the D_q spectrum derived from the time series. The parameter values are changed continuously until the D_q curve matches with the D_q spectrum from the time series and the statistically best fit D_q curve is chosen. From this, the final $f(\alpha)$ curve can be evaluated. An important aspect of the scheme is that it also provides a set of parameters that can completely characterise a given $f(\alpha)$ curve. The parameters can play an important role in the nonsubjective comparison of the multifractal properties of the same system under different conditions, such as, the changes in the chaotic attractor due to parameter variation, changes in the physiological conditions etc.

To illustrate our scheme, we choose the time series from a standard chaotic attractor, namely the Rossler attractor with parameter values $a = 0.2, b = 0.2$ and $c = 7.8$. We use 10000 data points generated with a time step $\Delta t = 0.1$. The D_q spectrum is first computed with embedding dimension $M = 3$, for q values in the range $[-20, +20]$, taking a step width of $\Delta q = 0.1$. Choosing D_{-20}, D_1 and D_{20} as the input values for the $f(\alpha)$ function Eq. (2), the parameters γ_1 and γ_2 are scanned in the range $[0, 1]$ and the statistically best fit D_q curve is chosen. The complete $f(\alpha)$ spectrum is then computed from the best fit D_q curve. The D_q spectrum and the best fit D_q curve are shown in Fig. 1 (top panel). The complete $f(\alpha)$ profile computed from the best fit D_q curve is also shown in Fig. 1 (bottom panel).

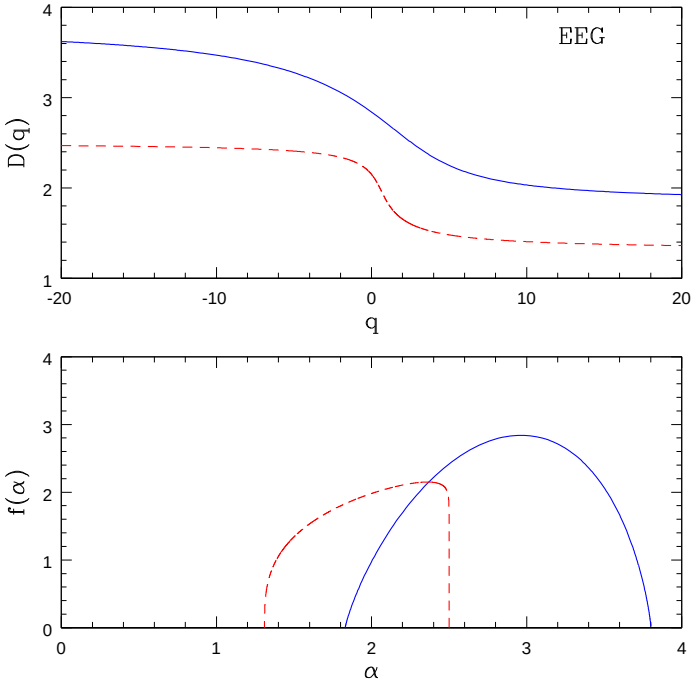

Fig. 2. The top panel shows the D_q spectrum computed using our scheme from representative EEG time series for healthy persons (continuous line) and during epileptic seizure (dashed line). The bottom panel shows the corresponding $f(\alpha)$ spectrum.

3 Application to Physiological Data

Physiological systems are, in general, complex where several nonlinearities are involved. We use physiological data commonly used for this kind of analysis, namely, EEG and HRV. In the case of EEG, we analyse signals from normal state and during epileptic seizure. Four data sets each from both cases are used for the analysis. In the case of HRV, we use three catagories of time series. The first one is from normal healthy persons, while the second and third corresponding to different pathological conditions of the heart, namely, congestive heart failure (CHF) and atrial fibrillation (AF). Four data sets for each of the above mentioned classes of HRV are analysed.

The EEG data were downloaded from the website of the Department of Epileptology, University of Bonn while the ECG data were obtained from http://www.physionet.org/physiobank/archives. The EEG data sets consist of continuous data streams of about 24 secs long and with approximately 5000 data points. The HRV data sets for different catagories consist of continuous data streams of approximately 5400 data points with a time step of 0.04 secs. All computations are done for an embedding dimension $M = 3$ and we show results for representative time series from each class.

The D_q and $f(\alpha)$ spectra for the two classes of EEG signals computed by our scheme are shown in Fig. 2. Similarly, the D_q and $f(\alpha)$ spectra for the three different classes of HRV time series are shown in Fig.3 and Fig. 4 respectively. One result which is clear from the figures is that all these signals show multifractal character. Some earlier studies had suggested that there could be a loss of multfractality for HRV in some pathological states. But we find that there is only a change in the multifractal character from healthy to pathological states.

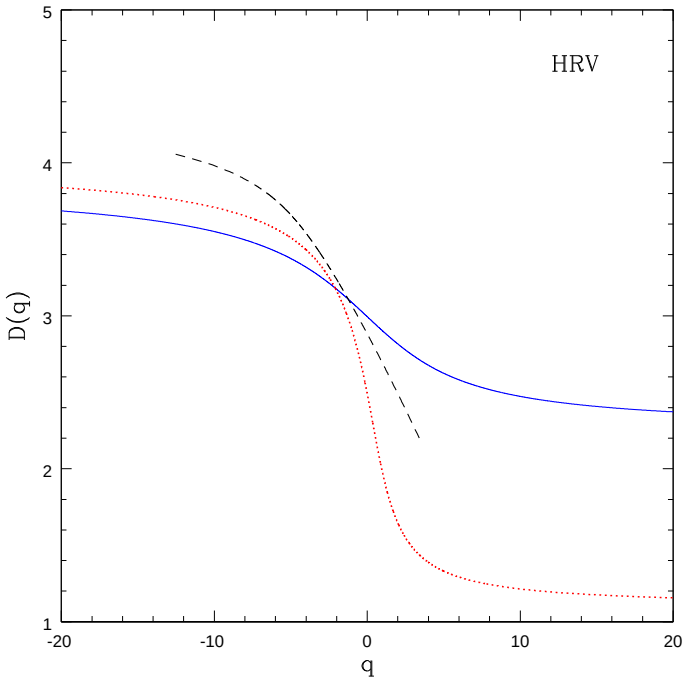

Fig. 3. Typical D_q spectra for HRV signals computed from healthy persons (continuous line), persons with CHF (dotted line) and those with AF (dashed line).

Of course, the difference between healthy and pathological time series is evident even visually, with the healthy signals appearing much like random fluctuations and the pathological ones do have some spiky nature. So we expect that these differences are also reflected in their D_q and $f(\alpha)$ spectra. The question is whether these qualitative changes can be quantified using our algorithmic scheme. It is quite evident from the figures that the nature of the $f(\alpha)$ profile is different for healthy and pathological states, in the case of both EEG and HRV. There is significant change in the profile of the spectrum and the parameter values between healthy and pathological states, for both EEG and HRV.

The range of α values, $|\alpha_{max} - \alpha_{min}|$, generally tend to change from healthy to pathological states in all cases. But the changes in the other three parameter

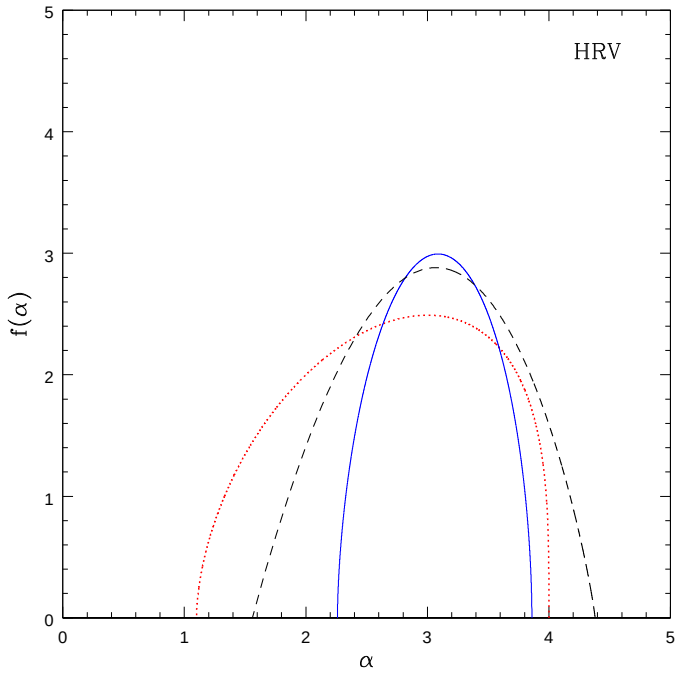

Fig. 4. The $f(\alpha)$ spectrum corresponding to the three cases of HRV signals shown in the previous figure.

values seems to be more significant. The values of γ_1 and γ_2 appear to be more sensitive to the changes in the multifractal character of the time series, especially since the range of γ_1 and γ_2 is limited ($0 < \gamma_1, \gamma_2 < 1$). For example, for the healthy data sets, the values of γ_1 and γ_2 are very close and always $\gamma_1, \gamma_2 > 0.8$. But in the case of pathological states, their values are generally found to be much less, with the difference $|\gamma_1 - \gamma_2|$ increasing. This, in turn, increases the asymmetry between the two branches of the $f(\alpha)$ profile.

Thus our results clearly indicates the importance of computing the multifractal spectrum using an algorithmic scheme and the utility of the associated parameters in differentiating signals from different physiological conditions. But we have used only limited number of data sets for the analysis. Whether all the trends shown by the parameters as discussed above are genuine and whether they can be used as diagnostic tools from a practical point of view will have to be confirmed by a much more comprehensive data analysis.

4 Conclusion

In this paper, we analyse an ensemble of physiological signals generated from different physiological conditions and try to distinguish them based on their multifractal properties. We use the automated algorithmic scheme recently proposed by us to compute the $f(\alpha)$ spectrum from the time series. The scheme

provides a set of parameters to characterise a given $f(\alpha)$ spectrum. The scheme is first tested and illustrated using synthetic time series from standard chaotic systems. It is then applied to two catagories of physiological data, namely, EEG and HRV. The signals from healthy and pathological states in both catagories are analysed. Our analysis indicates that the set of parameters characterising the $f(\alpha)$ spectrum show systematic difference between healthy and pathological states in both catagories. Thus, we find that measures based on multifractal structure can be effectively employed for differentiating signals from healthy and pathological states.

The authors thank the Department of Epileptology, University of Bonn, for making the human brain EEG data available on their website.

KPH and RM acknowledge the financial support from Department of Science and Technology, Govt. of India, through a research grant No. SR/SP/HEP-11/2008.

References

1.R. Sassi, M. G. Signorini and S. Cerutti, *CHAOS*, 19: 028507, 2009.
2.U. Freitas, E. Roulin, Jean-Francois Muir and C. Letellier, *CHAOS*, 19:028505, 2009.
3.L. Glass, *CHAOS*, 19:028501, 2009.
4.N. Pradhan and D. Narayana Dutt, *Comput. Biol. Med.*, 23:425, 1993.
5.W. Latzenberger, H. Preissl and F. Pulvermiller, *Biol. Cybernetics*, 73:477, 1995.
6.M. A. F. Harrison, I. Osorio, M. G. Frei, S. Asuri and Ying-Chang Lai, *CHAOS*, 15:033106, 2005.
7.L. Glass, A. L. Goldberger, M. Courtemanche and A. Shrier, *Proc. R. Soc. Lond. Ser. A*, 413:9, 1987.
8.F. X. Witkowski, K. M. Karnagh, P. A. Penkoske, R. Plonsey, M. L. Spano, W. L. Ditto and D. T. Kaplan, *Phys. Rev. Lett.*, 75:1230, 1995.
9.C. S. Poon and C. K. Merril, *Nature*, 389:492, 1997.
10.F. Ravelli and Anbolin, *Biol. Cybernetics*, 67:57, 1992.
11.R. B. Govindan, K. Narayanan and M. S. Gopinathan, *CHAOS*, 8:495, 1998.
12.L. Glass and P. Hunter, *Physica D*, 43:1, 1990.
13.A. L. Goldberger, *News. Physiol. Sci.*, 6:87, 1991.
14.F. Mitschke and M. Dimming, *Int. J. Bif. Chaos*, 3:693, 1993.
15.K. P. Harikrishnan, R. Misra, G. Ambika and A. K. Kembhavi, *Physica D*, 215:137, 2006.
16.K. P. Harikrishnan, R. Misra, G. Ambika and R. E. Amritkar, *CHAOS*, 19:143129, 2010.

Chaotic Modeling and Simulation (CMSIM) 1: 60–66, 2013

Complex Dynamics of Multiparticle System Governed by Bounded Rationality

Arkady Zgonnikov[1] and Ihor Lubashevsky[2]

[1] University of Aizu, Fukushima, Japan
(E-mail: arkady.zgonnikov@gmail.com)
[2] University of Aizu, Fukushima, Japan
(E-mail: i-lubash@u-aizu.ac.jp)

Abstract. We consider a system of interacting elements that mimic certain properties of human perception, namely, the bounded capacity of ordering events, actions, etc. according to their preference. Previously this feature was described by the notion of dynamical traps, which is modified in the present work in order to take into account the imperfectness of human perception of their own actions. Numerically we demonstrate that the considered system under the presence of dynamical traps of a new type exhibits complex dynamics, including highly irregular motion.
Keywords: Complex dynamics, multiparticle systems, dynamical traps.

1 Introduction

The employment of various physical models in social sciences could be observed during last decades. Among the models that are used widely in studying cooperative phenomena in social systems are multi-particle dynamical models (see, e.g., Helbing and Mólnar[1], Ohnishi[2]). Advances in this field, though, face the fact that human beings indeed differ in their basic properties from the objects of the inanimate world described by Newtonian mechanics. This fact may lead one to the problem of development of new physical notions that should be introduced in addition to the well-studied ones of the modern physics in order to reflect the essential aspects of human behavior in social systems.

Mathematical notion of equilibrium points is one of the cornerstones of the modern physics; it is also widely used in social psychology (see, e.g., Vallacher[3]). However, human as a key acting element of the dynamical systems is often not capable to clearly recognize the desired equilibrium position among a certain set of its neighboring points in the corresponding phase space. This feature of human cognition is referred to as bounded or fuzzy rationality (Dompere[4]). The application of the dynamical traps notion as a mathematical formalism for describing human fuzzy rationality was investigated by Lubashevsky[5]. To briefly review this concept, let us appeal to the car following theory and consider hypothetical dynamical system controlled by an operator

Received: 10 April 2012 / Accepted: 16 October 2012

ISSN 2241-0503

whose purpose is to maintain the system near the equilibrium point set to the origin. The system of equations describing the system dynamics under the control of the operator take the following form

$$\begin{aligned} \dot{x} &= v, \\ \dot{v} &= \Omega(x,v)F(x,v,a_{opt}(x,v)). \end{aligned} \tag{1}$$

Here x and v are the system coordinate and velocity, respectively; a_{opt} is optimal in some sense control strategy chosen by the operator. The cofactor $\Omega(x,v)$ equals unity for all values of (x,v) that are far enough from the equilibrium point and $\Omega(x,v) \ll 1$ in a certain neighborhood $\mathbb{Q}_{tr}$ of the equilibrium point. In order to explain the meaning of the cofactor $\Omega(x,v)$ we consider the behavior of the operator who is approaching desired phase space position $(x=0, v=0)$. Let us assume that if the current position is far from the origin, the operator perfectly follows the optimal control strategy. If the current position is recognized by the operator as "good enough" $((x,y) \in \mathbb{Q}_{tr})$ (though it may be not strictly optimal) due to her fuzzy rationality, she halts active control over the system so that the system dynamics is stagnated in a certain vicinity of the desired position (in case of stable equilibrium). Therefore, $\mathbb{Q}_{tr}$ is called the area of dynamical traps.

Previous studies on the dynamical trap effect in chains of particles governed by equations of form (1) have shown that it may cause complex cooperative phenomena to arise in the systems under the presence of white noise (Lubashevsky *et al.*[6]), as well as in the systems without the influence of stochastic factors (Lubashevsky[5]). However, it should be taken into account that in the real world the operator cannot usually affect the system velocity directly as prescribed by equations (1), e.g., in the car following the operator is not able to directly affect the speed of the car and in fact controls only the acceleration (Lubashevsky[7]).

It should also be noted that the operator perception of her own actions is not perfect, and could also be described in terms of fuzzy rationality. Namely, the value of the actual control effort could be treated as an acceptable by the operator if its deviation from the optimal strategy is of low magnitude. Therefore, in order to take into account the issues discussed above, in present work we introduce the dynamical trap model of a new type. While previously the dynamical trap region was referred to as two-dimensional region in the "coordinate-velocity" phase space, we propose the concept of the dynamical trap in the "space" of behavior strategies as a certain neighborhood of the optimal one.

The purpose of the current paper is to demonstrate that bounded rationality of human cognition in perceiving their own actions could be responsible for intrinsic cooperative phenomena in the systems of interacting elements under the control of human operators.

2 Model

Let us consider the chain of N motivated particles (Fig. 1) moving along parallel vertical axes; the motion of each particle is characterized by its coordinate x_i,

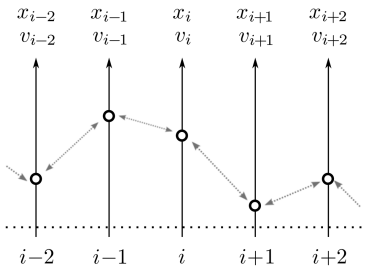

Fig. 1. The chain of N motivated particles moving along parallel axes. Terminal particles $i = 0$ and $i = N + 1$ are fixed at $x = 0$. Dotted arrows indicate the interaction between neighboring particles.

velocity v_i and acceleration a_i. Each particle tends to minimize the absolute values of its relative coordinate and velocity with rescept to its neighbors, namely, $\eta_i = x_i - \frac{1}{2}(x_{i-1} + x_{i+1})$ and $\vartheta_i = v_i - \frac{1}{2}(v_{i-1} + v_{i+1})$. Two terminal particles are assumed to be fixed: $x_0(t) \equiv x_{N+1}(t) \equiv 0$. The dynamics of such system could be described by the following equations

$$\begin{aligned} \dot{x}_i &= v_i, \\ \dot{v}_i &= a_i, \\ \dot{a}_i &= \Omega_a(a_i, a_{opt}\big(\eta_i, \vartheta_i, v_i)\big)\big(a_{opt}(\eta_i, \vartheta_i, v_i) - a_i\big), \end{aligned} \tag{2}$$

for $i = \overline{1, N}$. Here

$$a_{opt}(\eta, \vartheta, v) = -\Omega_\vartheta(\vartheta)(\eta + \sigma\vartheta + \sigma_0 v) \tag{3}$$

is the optimal strategy of the operator behavior which is considered to depend mainly on the current values of the relative position η and velocity ϑ. σ could be treated as a relative weight of the velocity variations as a stimulus causing operator actions (with respect to the first stimulus η_i); $\sigma_0 v_i$ stands for the friction force which characterizes the physical properties of the environment where the system is placed ($\sigma_0 \ll 1$). The dynamical trap effect in system (2), (3) is modelled by cofactors Ω_ϑ and Ω_a defined as follows

$$\begin{aligned} \Omega_\vartheta(\vartheta) &= \frac{\Delta_\vartheta + \vartheta^2}{1 + \vartheta^2}, \\ \Omega_a(a, a_{opt}) &= \frac{\Delta_a + (a_{opt} - a)^2}{1 + (a_{opt} - a)^2}, \end{aligned} \tag{4}$$

where parameters $0 \le \Delta_\vartheta, \Delta_a \le 1$ determine the intensity of dynamical traps: the less these parameters, the stronger the effect of corresponding dynamical traps.

It should be pointed out that we assume the former dynamical trap cofactor Ω_ϑ not to depend on particle coordinate; it could be explained in such a manner that the control over system relative velocity ϑ is of prior importance for the operator comparing to the control over position η. Thus, if the relative velocity becomes sufficiently small, the operator prefers to retard the correction of the

coordinate in order not to make the velocity variations take undesirably large values (Lubashevsky[5]).

The cofactor Ω_a in (2) stands for the dynamical trap effect of a new type which was not studied previously. Assuming $\Omega_a = 1$, one could easily see that the last equation in (2) in fact implies the equality $a_i = a_{opt}()$. However, we consider that the operator, first, is hardly able to precisely implement the strategy a_{opt} defined by (3), and, second, cannot distinguish between the strategies that are close in some sense to the optimal one. Therefore, one may think of a certain neighborhood of the optimal strategy in the space of all possible strategies, such that each strategy from this region is treated as the optimal one by the operator. So in case the operator feels that current control regime is optimal, she just keeps maintaining the current value of the control effort constant so that $\dot{a} \approx 0$. When the operator realizes that the current strategy is far from the optimal one, she starts adjusting it to the desired value which means that $\dot{a} \sim (a_{opt} - a)$.

These speculations led us to the system (2)–(4) as a model that may reflect some of mentioned properties of human bounded rationality. The rest of the paper is devoted to the analysis of anomalous cooperative phenomena that could be observed in such system for various values of system parameters.

3 Numerical simulation

In the current work we present the results of the preliminary analysis of system (2)–(4). The scope of the future work should comprise certain extensions of the proposed model; to be specific, the characteristic time scale of the system dynamics should be taken into account, as well as the thresholds of the velocity and acceleration perception. Here we consider all these parameters to take values equal to unity.

We analyze numerically the collective behavior of the particle chain by solving equations (2)–(4) using the standard $(4, 5)$-Runge-Kutta algorithm. Due to the fact that the behavior of the studied system significantly varies depending on the number of interacting particles, the below analysis is divided into three parts according to the cases 1)$N = 1, 2$; 2)$N = 3$; 3)$N \geq 4$. We should specify that all of the following results were obtained for small values of parameters Δ_ϑ and Δ_a, namely 0.001, which correspond to the strong effect of dynamical trap. Below all phase space portraits depict projections of 3-dimensional phase trajectories on the "coordinate-velocity" plane generated by the system motion during the time interval of $T = 10^4$ given small randomly assigned initial disturbances. In case of multi-particle chains the middle particles trajectories are represented; particle motion structure is similar for all particles in the given ensemble, however, particles in the center of the chain have slightly larger fluctuations amplitude.

The numerical simulation of the single particle oscillating between its two fixed neighbors ($N = 1$) figures out that the combination of two dynamical traps causes the limit cycle to arise in the system phase space, while without the dynamical trap effect the system has single stable fixed point ($x = 0, v = 0, a = 0$). Also it is notable that the previous studies discovered the stable

behavior of the single oscillator under the presence of the single dynamical trap characterizing the fuzzy rationality in perceiving the velocity variations (Lubashevsky[5]).

First let us consider the case of the single particle oscillating between two fixed neighbors. The phase portrait and phase variables distributions of the system motion are depicted on Fig.2*a-c*. The chain of two interacting particles exhibits the similar behavior patterns (see Fig.2*d-i*), except for the phase trajectories assymetry caused by the introduction of the second oscillator. In both cases the structure of the limit cycles is stable with respect to variations of the system parameters. Namely, the found pattern remains for the following values of system parameters: $\sigma = 1,\ 3$; $\sigma_0 = 0,\ 0.01,\ 0.1$.

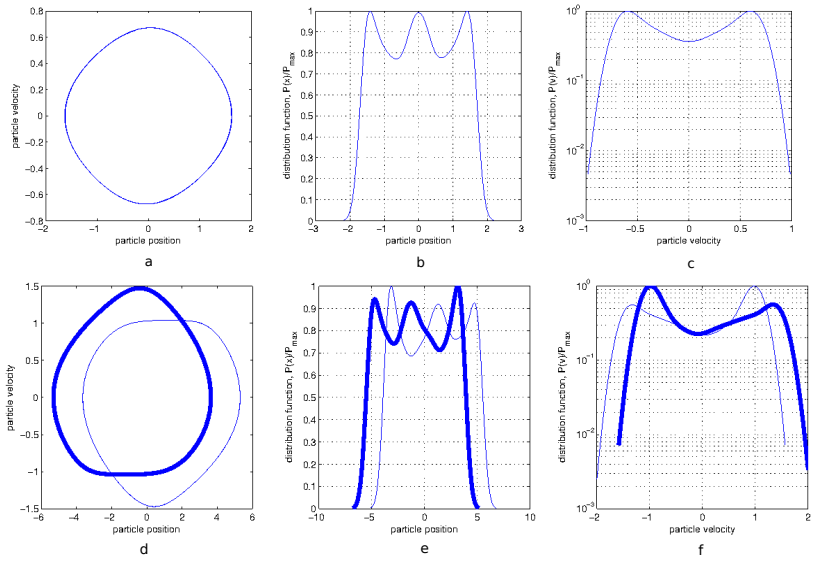

Fig. 2. The phase trajectory projections of system (2)–(4) for $N = 1$ (a) and $N = 2$ (d) on the "coordinate-velocity" plane. The right four frames show corresponding phase variables distributions. On figures (d)–(f) thin and thick lines are introduced in order for one to distinguish between two moving particles. Parameters used for simulation are $\sigma = 1$, $\sigma_0 = 0.01$.

From Fig.2 it could be seen that the dynamical trap effect causes the instability of the single particle motion; the limit cycle emerges. The similar phenomena could be observed in almost the same form for each particle in the pair of coupled oscillators. The situation dramatically changes when the ensemble of three particle is taken into consideration. Adding just one more oscillator to the system causes the anomalous cooperative phenomena to emerge, particularly, complex 3-dimensional attractor arises in the system phase space (see Fig.3*a-c*).

Notably, unlike the previous cases ($N = 1, 2$), introducing the external friction force ($\sigma_0 \neq 0$) causes the attractor to become significantly blurred (see

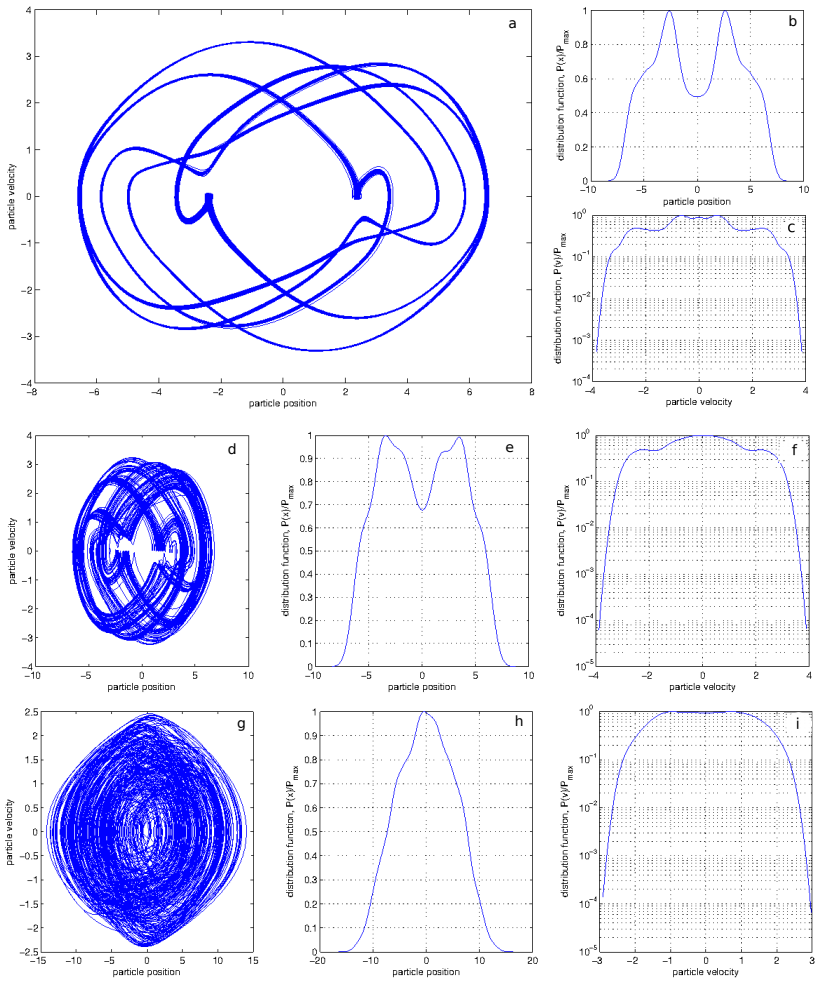

Fig. 3. The phase trajectory projections of the middle particle from the ensemble (2)–(4) and corresponding phase variables distributions for $N = 3$. Frames *a-c* illustrate the case $\sigma = 1, \sigma_0 = 0$, frames *d-f* depict the case $\sigma = 1, \sigma_0 = 0.01$, frames *g-i* are for the values of parameters $\sigma = 3, \sigma_0 = 0$

Fig.3*d-f*), while increasing the relative weight of the particle velocity as the stimulus for the operator actions makes the particle dynamics to take form of chaotic oscillations (Fig.3*g-i*).

In case of the relatively large number of interacting elements the system dynamics becomes highly irregular. The chain of four particles demonstrate the oscillatory behavior as could be seen on Fig.4*a-c*. It is worth underlining that the well-defined attractor (Fig.3*a*) could be destructed just by adding one particle to the ensemble (Fig.4*a*) without changing any of the system parameters.

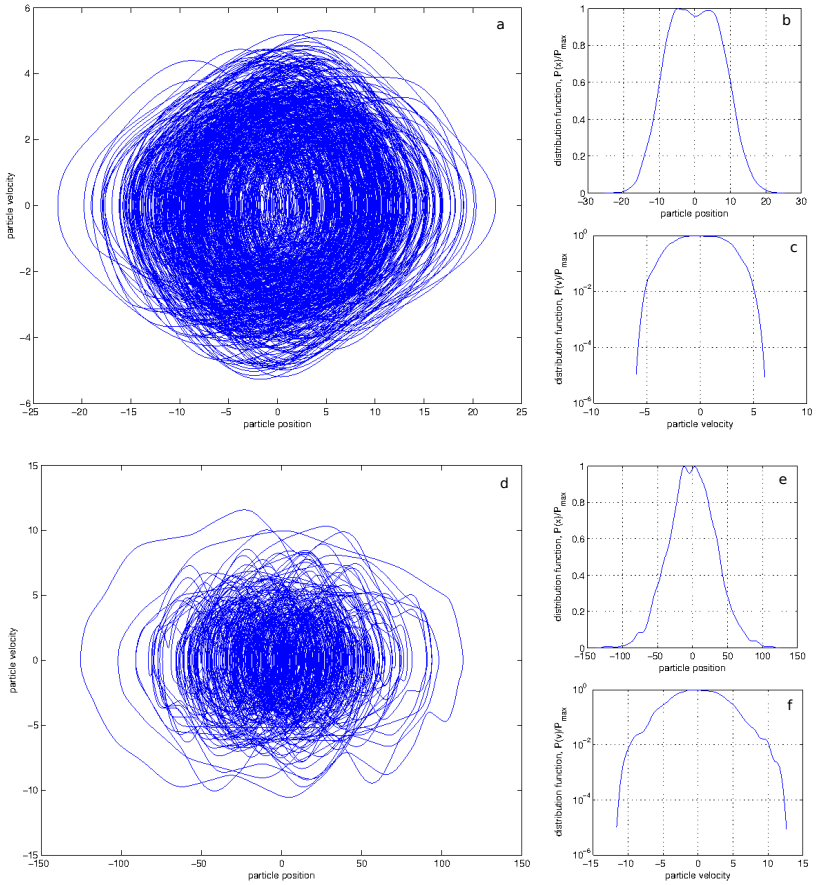

Fig. 4. The phase trajectory projections and phase variables distributions of the middle particle from the chain (2)–(4) for $N = 4$ (figures a-c) and $N = 15$ (figures d-f). Parameters used for simulation are $\sigma = 1$, $\sigma_0 = 0$.

The system motion trajectories for $N = 15$ (Fig.4d-e) are of even greater irregularity due to the increased number of particles and corresponding cooperative effect. For larger N the system motion exhibits the patterns of similar structure, but the amplitude of the fluctuations increases with N).

4 Conclusion

In the present paper we discuss the new type of the dynamical trap – a model describing human bounded rationality. The standard "coordinate-velocity" phase space inherited from the Newtonian mechanics is proposed to be extended by the acceleration variable. By analyzing the behavior of the motivated particles chain governed by bounded rationality we demonstrate that the multi-particle system under the presence of the dynamical trap of a new type exhibits intrinsic

cooperative behavior. The various complex patterns of the system motion are shown to arise depending on the system parameters. First, it is demonstrated that the dynamical trap effect of a new type can cause the instability in the single oscillator dynamics which was not observed in the previous studies on the dynamical traps model. Second, the system dynamics patterns are shown to take the complex 3-dimensional structure in case of three-particle ensemble. Third, we demonstrate that with the increasing number of elements the system motion becomes significantly irregular, for large N exhibiting chaotic oscillations. The obtained results confirm that the system under consideration could exhibit anomalous behavior; however, the proposed model require more detailed analysis.

Acknoledgements: The work was supported in part by the JSPS "Grants-in-Aid for Scientific Research" Program, Grant №245404100001.

References

1.D. Helbing, P. Molnar. Social force model for pedestrian dynamics. *Phys. Rev. E*, 51:4282–4286, 1995.
2.T. Ohnishi. A multi-particle model applicable to social issues—time-evolution of Japanese public opinion on nuclear energy. *Annals of Nuclear Energy*, 29:15, 1747–1764, 2002.
3.R.R. Vallacher. Applications of Complexity to Social Psychology, in *Encyclopedia of Complexity and Systems Science*, ed. R.A. Meyers (Springer Science+Business Media, LLC., New York, 2009), pp.8420–8435.
4.K.K. Dompere. Fuzzy Rationality. Springer-Verlag, Berlin, 2009.
5.I. Lubashevsky. Dynamical traps caused by fuzzy rationality as a new emergence mechanism. *Advances in Complex Systems*, in press, 2012.
6.I.A. Lubashevsky, R. Mahnke, M. Hajimahmoodzadeh, and A. Katsnelson. Long-lived states of oscillator chains with dynamical traps. *Eur. Phys. J. B*, 44, 63–70, 2005.
7.I.A. Lubashevsky, P. Wagner, R. Mahnke. Rational-driver approximation car-following theory. *Phys. Rev. E*, 68, 056109, 2003.

Chaotic Modeling and Simulation (CMSIM) 1: 67-74 , 2013

Application of planning artificial neural networks in solver of tasks of intellectual self-organizing automatic-control systems

Michail F. Stepanov, Andrew M. Stepanov

Saratov State Technical University, Saratov, Russia
E-mail: mfs@sstu.ru

Abstract: Expansion of orbs of application (appendix) of automatic control has caused development of intellectualization of control systems. One of the important directions are intelligent self-organizing system of automatic-control (ISSAC). They are capable to supply required capabilities of the purpose of control with change of environments and/or their parameters). It is attained by automatic synthesis of the law of control, the most adequate a current situation. For this purpose the intelligent system of synthesis is used.
The planning subsystem creates (in the elementary case selects from already known) the most adequate procedure of synthesis. However existing approaches to planning actions have no property of mass parallelism. It do not allow to apply them in control systems owing to the big costs of time for a solution of task. It is offered to use planning artificial neural networks (PANN) within the planning subsystem of tasks solver. Features of planning of tasks solvings with use PANN are considered. Outcomes of simulation of control by a population of plants with use ISSAC are represented.
Keywords: planning artificial neural networks, simulation of intellectual control systems.

1. Introduction

Increasing thickening of objects of control in a combination with toughening requests to accuracy and quality of control has reduced to an inconsistency with traditional approaches to construction of control systems. Modern control systems, as a rule, are working (function) in interacting with other systems which can influence on their behavior. The problem is complicated that, those conditions of functioning of control systems are changing during their work. It concerns not only the change of controlled plants and environments of their functioning, but also and the purposes of control. Necessity of organization of interacting of a set of the control systems a population of probably interconnected controlled plants essentially complicates a task of control.

2. Intelligent self-organizing control systems

It is expedient to apply the approach based on usage of intellectual systems of synthesis of the law of control to a solution of the indicated problem [1]. Such systems for a solution of a specific task of synthesis of the law of control in the

Received: 28 March 2012 / Accepted: 30 September 2012

ISSN 2241-0503

beginning create a program of a solution of the task as ordered population of elementary operations and executing them make the required law of control. The amount of the elementary operations used for task solving of synthesis of the law of control, is not big, as they represent procedural definition of concepts of the theory of automatic control (TAC) [2]. Creating of the program a solution of the task is carried out based on knowledge of methods of task solving of the theory of automatic control. For this purpose are traditionally used a tools of automatic theorem proving. It is known, that tasks of scheduling of operations or automatic theorem proving are difficultly for deciding and them referred to category of NP-challenge. For such tasks of an expenditure of resources by searching of a solution will increase under the exponential law with growth of complexity of the task. Thus the most perspective are multilevel systems in which at the expense of introduction of hierarchically interconnected spaces are narrowed down of area for searching a solution of the task. Intelligent self-organizing control systems are understood as systems of automatic control, capable to self-organizing by means of a modification of the law of the control, using methods of an artificial intelligence [3].

Structure of an intelligent self-organizing system of automatic control (see fig. 1): the measuring subsystem, the executive mechanisms, the calculator of control action, the subsystem of identification of models of plant of control and environment based on the data of a measuring subsystem, the block of shaping of the purpose of control on the basis of the own purposes of behavior and an emotional state of an intelligent self-organizing control system, the intellectual subsystem of synthesis of the law of control, the block of a self-estimation realizing an evaluation of a quantitative equivalent of quality estimate ("emotion") of behavior of this intellectual self-organizing system of automatic control, formed on the basis of a self-estimation and the estimations obtained from higher hierarchy levels of control systems.

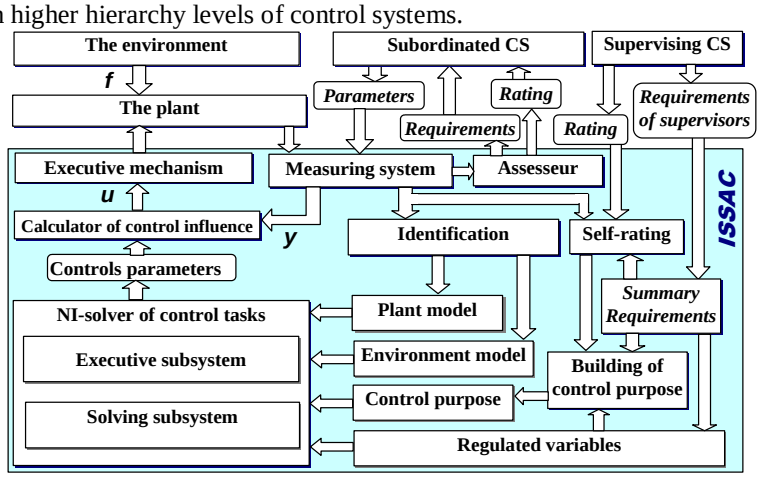

Fig. 1. Structure of an intelligent self-organizing system of automatic control

Setting of the task of synthesis of the new law of control includes exposition of known components of a control system, an environment and the purpose of control, not specifying of a method (procedure) of a solution of the task, i.e. *none procedurally*. The set of methods of synthesis and the analysis of control systems are more not very important yet. More important becomes are availability of capabilities of tools by automatically definition are methods, relevant to the current task.

The problem of an automatic solution non procedural tasks in view demands engaging intelligent tools, understanding under a word "intelligent" ability to decide new tasks [4]. Therefore, the subsystem of automatic synthesis of the law of control of a self-organizing control system should represent the intelligent system of automatic synthesis using methods of an artificial intelligence for preliminary construction of the schedule of a solution of a specific target of synthesis. The new law of control is formed as a result of execution of the constructed plan of action. Thus, most a gorge is the mechanism of scheduling of operations. It is stipulated by that methods used now have no property of mass parallelism, and, therefore, «*the damnation of dimension*» is inherent in them, not permitting to solve tasks of practical complexity.

The complex solution of the indicated problems is known on the basis of the methodology *of automatic* problem solving the theory of automatic control including [2], [3]: 1) *formalizing* knowledge of methods of problem solving of synthesis and analysis control systems as multilevel model of a set of formalized tasks (MMSFT) TAC [2]; 2) construction *of a planning* subsystem as the system of automatic theorem proving representing the application system of calculus of sequent [4], [5] and called as the multilevel axiomatic theory of automatic solutions of formalized tasks (MATASFT) TAC [2], [3]; 3) usage *of planning artificial neural networks* (PANN) [2], [3], [6] as a search engine of output in formal axiomatic systems; 4) Result of the planning (schedule) of a solution of the task is the program on the problem oriented language "Instrument - OP", which supporting a paradigm «rules IF-THEN» [2]; 5) construction *of the executive* subsystem as the application package controlled by the interpreter of the language "Instrument - OP".

Multilevel model of a set of formalized tasks of TAC is $M_O =< \Pi, Д, O >$, were $\Pi = \{\text{П}_i \mid \text{П}_i =< P_i, H_i, \Psi_i, Q_i >,\ P_i \subseteq \wp, H_i \subseteq \aleph, \Psi_i \subseteq \Im, Q_i \subseteq \Pi\}$ – set of the formalized generalizations of control system components called as *subjects* and possessing: *properties* $p_j \in P_i \subseteq \wp = \{\rho \mid \rho = \{true \mid false\}\}$; *characteristics* $h_j \in H_i \subseteq \aleph = \{\chi_k \mid \chi_k \in \mathbf{C}^{n_k}, n_k \in \mathbf{N}\}$, **C**, **N** – sets complex and natural numbers accordingly; *forms* of mathematical models $m_j \in \Psi_i \subseteq \Im = \{\mu_1, ..., \mu_\tau\}$; *components* $q_j \in Q_i \subseteq \Pi$; $Д = \{\text{Д}_i \mid \text{Д}_i : \wp \cup \aleph \cup \Im \to \wp \cup \aleph \cup \Im \cup O\}$ – set of operations for processing attributes of subjects; $O = \{o_i \mid o_i : \wp \cup \aleph \cup \Im \to \{true \mid false\}\}$ – set of the predicates defined on attributes of subjects. *Actions*

$Д_i = \langle c_i, d_i, r_i, g_i \rangle \in Д$ and *relations* $o_i = \langle c_i, d_i \rangle \in O$ are uniquely identified by the attributes $c_i \in \wp \cup O$ – conditions of applicability, $d_i \in \wp \cup \aleph \cup \Im$ – source data, $r_i \in \wp \cup \aleph \cup \Im \cup O$ – results of an action, $g_i \in O$ – requirements to results of an action. With a view of a raise of effectiveness multilevel representation of knowledge as a three-rank system of submodels is used, each of which has three-level representation of knowledge: $M = \langle M^1, M^2, M^3 \rangle$, $M^1 = \langle M_1^1, ..., M_m^1 \rangle$, $M^2 = \langle M_1^2, ..., M_n^2 \rangle$, $M^3 = \langle M_1^3 \rangle$, $M_i^r = \langle M_{0,i}^r, M_{1,i}^r, M_{2,i}^r \rangle$, $M_{k,i}^r = \langle П_{k,i}^r, Д_{k,i}^r, O_{k,i}^r \rangle$, were M^r - model of r-th rank; M_i^r - i-th submodel of r-th rang; $M_{k,i}^r$ - i-th submodel of k-th level of r-th rank; $П_{k,i}^r$ – set of subjects, $Д_{k,i}^r$ – set of actions, $O_{k,i}^r$ – set of relations of submodel $M_{k,i}^r$. The multilevel model *of M* is created by the scientists on the basis of model M_O by means of multistep generalizations of knowledge [2], [4]. The planning subsystem is the formal logical system representing the application system of calculus of sequents [4], [5], called *as the multilevel axiomatic theory of automatic solutions of formalized tasks (MATASFT)* TAC [2]: $T = \langle T_1^1, ..., T_m^1, T_1^2, ..., T_n^2, T_1^3 \rangle$, $T_i^r = \langle T_{0,i}^r, T_{10,i}^r, T_{1,i}^r, T_{21,i}^r, T_{2,i}^r \rangle$, were T_i^r – *i*-th three-level theory of solutions *r-th* rank; $T_{0,i}^r, T_{1,i}^r, T_{2,i}^r$ – *i*-th single-level theories of solutions 0-th, 1-th, 2-th levels *r*-th rank; $T_{10,i}^r, T_{21,i}^r$ – the translational theories linking 1-th and 0-th, 2-th and 1-th levels of *r*-th rank. Theory *T* is automatically generated [4] on the basis of multilevel model *of M* under the following scheme: subjects of models $\mathrm{M}_{\mathrm{k,i}}^{\mathrm{r}}$ will be converted to variable theories of solutions $\mathrm{T}_{\mathrm{k,i}}^{\mathrm{r}}$, actions – in axioms, a sheaf between subjects – in axioms of translational theories $\mathrm{T}_{\mathrm{kk\text{-}1,i}}^{\mathrm{r}}$. Specificity of data domain TAU has stipulated presence in theories of solutions $\mathrm{T}_{\mathrm{k,i}}^{\mathrm{r}}$ of the own axioms with source data, a required results, conditions for applicability, but also the requirements to results. Therefore production rules of theories of solutions $\mathrm{T}_{\mathrm{k,i}}^{\mathrm{r}}$, in addition to rules systems G4 [2], include the special production rules, which making (playing) a main role during scheduling of solving of task [3].

Scheduling of problem solving of synthesis of control system is complicated that at a stage of scheduling the values of many parameters of models of components of control system are unknown, they will defined only during executing of the scheduled program of a solution of the task. Therefore the

developed schedule should include all alternate paths of a solution, choice of the most approaching from which is carried out immediately already at executing of the scheduled program of a solution of the task. Therefore, for example, it is obvious, that before realization of any operation having conditions of applicability, values of appropriate logical expressions should be checked. On the other hand, after realization of operations with requirements to outcome it is necessary to check realization of the indicated requirements. Therefore, in the schedule of a solution of the task, in addition to the operations forming required outcome, should switch on as well the operations computing values of appropriate relations. Thus if requirements to required outcome appear outstanding then actions for elimination of a discordance should be undertaken. A common guideline on this score does not exist, as specificity of problem area here should be taken into account. In our case it reduces in include (appearance) in theories of solutions of axioms for which in conditions of applicability are indicated negation of requirements to outcome. Thus, the operation that was defined by such axiom should be applied to support of realization of requirements to outcome if it became known, that these requirements are not fulfilled. Bypass of "the damnation of dimension" can realize the *planning artificial neural networks* (PANN) [2], [3], [6] which possessing property of mass parallelism. Structurally PANN consist of *resolving artificial neural networks* (RANN) and *archive artificial neural networks* (AANN). The device of synchronization (see fig. 2) coordinates their operation. RANN is representing a three-layer network. She fulfills an inverse method of search of a solution of the task in a formalism of used fragment MATASFT TAC. The constructed schedule of a solution of the task is saved in AANN. RANN is a dynamic artificial neural network. Values on the output are varying with the constant signals on inputs. The initial state of all neurons RANN is not active.

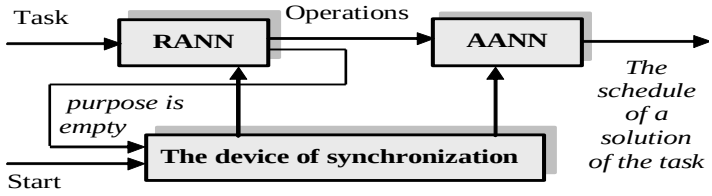

Figure 2. Structure of a planning artificial neural web, where: RANN -resolvelly artificial neural network (ANN), AANN - an archival artificial neural network

For the tasks having a solution, the separate neurons of an outputs layer of RANN short-term are going to an active (excited) state, which then is remembered in AANN for the subsequent inclusion in the schedule of a solution of the task. Values of outputs of neurons of one of interior layers of neurons of RANN is interpreted as values of the searching's purposes of a solution of the current task. Passage of these neurons in a non-active state reduces to appearance (generation) of signal, «the purpose is empty». It means that the solution of a task was obtained. Otherwise, on expiration of the solution time assigned on searching (an amount of pitches), the refusal to search a solution will be made. PANN allows solving simultaneously all subtasks of the source

task, forming a united plan of a solution. On paths of usage of neural networks always, it is necessary to solve two problems: preliminary tutoring of a web and interpretation of the obtained outcomes. In PANN both problems are solved by virtue of design features. Basic difference of the given approach is *automatic* generation MATASFT TAC, and after her and PANN on the basis of assigned MMSFT TAC. Instead of traditional tutoring of the neural network, the procedure of automatic creation (result) of the PANN is used based on the appropriate fragment MATASFT TAC, which is called as the single-level theory of solutions. The main idea of the procedure of creation of the PANN consists in shaping a neural network which stratums are compared with units of the single-level theory of solutions. Implementation on basis PANN of a planning subsystem of an intellectual system of automatic task solving of TAC was called as Naturally - Intellectual Solver (NI-solver) of tasks of TAC [2].

3. Research of intellectual self-organizing systems of automatic control

The offered concept of automatic task solving of TAC based on planning artificial neural networks has served as methodological base for creation of a system of simulation of intellectual self-organizing systems of automatic control. The task of simulation of intelligent self-organizing systems of automatic control refer to category rather complicated, because includes not only immediate control of the set plant, but also simulation of the intelligent behavior used for the purposes of self-organizing. Therefore, usage of universal software for simulation of such systems in full appeared unacceptable.

Such specialized resource is MISACS - a system of Modeling of Intelligent Self-organizing Automatic Control Systems [3]. MISACS it is intended for research of processes of control by a population probably interconnected and cooperating plants, controlled by the intelligent self-organizing systems of automatic control (ISSAC) organized in hierarchically connected structure.

MISACS gives the user the following possibilities in a graphics interactive regime: 1) To set an amount of levels of hierarchy of population ISSAC, an amount of plants of control and ISSAC in each level; 2) To install connections between plants of control and assigned for them ISSAC; 3) To set criteria of a self-estimation of behavior ISSAC (engineering, analytical); 4) To define MATASFT TAC for everyone ISSAC separately.

We research possibilities ISSAC for control of non-stationary plant (see fig. 3). Let the plant of control is described by the following equations:

$$\dot{x} = (A + \Delta A)x + u^* + Mf,\ x \in R^n,\ u \in R^n,\ f \in R^\mu,\ n = 3,\ \mu = 1,$$

$$\Delta A = [0]_n,\ 0 \le t < t_0,\ \Delta A = dA \times \sin(\omega \times (t - t_0)),\ \forall t \ge t_0$$

$$A = \begin{bmatrix} 0 & 1 & 0 \\ 0 & -300 & 1000 \\ 0 & -3 & -1 \end{bmatrix},\ M = \begin{bmatrix} 0 \\ 0 \\ 1 \end{bmatrix},\ dA = \begin{bmatrix} 0 & 0{,}1 & 0 \\ 0 & 250 & -700 \\ 0 & 2{,}5 & 0{,}7 \end{bmatrix},$$

$$f = \begin{cases} f_0, & 0 \le t < t_s \\ f_0 + f_m \times \sin(\omega_f \times (t - t_s)), & \forall t \ge t_s \end{cases},$$

were $t_0 = 4$ – the moment of the beginning of a modification of model of plant of control; ω – frequency of a modification of model of plant of control; $f_0 = 1{,}0$ – magnitude of stepping component exterior perturbation; $f_m = 0{,}25$ – amplitude of sine waves of the exterior perturbation; ω_f – frequency of sine wave of the exterior perturbation; $t_s = 5$ – the moment of inclusion of sine wave of the exterior perturbation; $[0]_n$ – zero matrix $n \times n$.

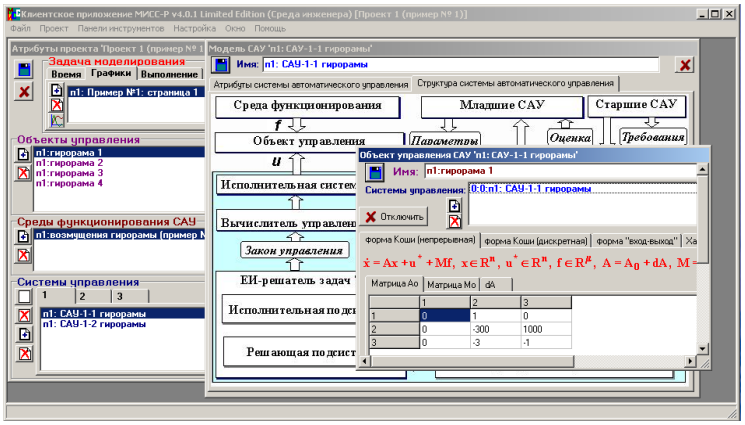

Fig. 3. Attributes of the project of simulation

The purpose of control is set as requirements on the statically errors of controlled variables:

$$\theta = Nx, \theta \in R^{\chi}, N = \begin{bmatrix} 1 & 0 & 0 \end{bmatrix}, \qquad \left|\theta_{\text{уст}_i}\right| \le \theta^*_{\text{уст}_i}, \ \theta^*_{\text{уст}}, \theta_{\text{уст}} \in R^{\chi},$$

$\theta^*_{\text{уст}_1} = 0{,}5$ at presence of stepping exterior perturbations $f_0 = 0{,}5$.

The initial law of control was synthesized counting upon stepping exterior perturbation $f_0 = 0{,}5$. Therefore with perturbation $f_0 = 1{,}0$ of the requirement to exactitude of regulating at the disconnected self-organizing are not fulfilled even for stationary plant (a curve 1 on fig. 4). Inclusion of self-organizing in an instant $t_c = 10{,}0$ with periodicity in 1 second and with a velocity of self-organizing **0,17** eliminates a problem, ensuring a required exactitude of regulating (a curve 2 on fig. 4). The transient for non-stationary plant of control at the disconnected self-organizing is mirrored with a curve 3 on fig. 4. Inclusion of self-organizing with the same parameters ensures a required exactitude of regulating and for non-stationary plant (a curve 4 on fig. 4).

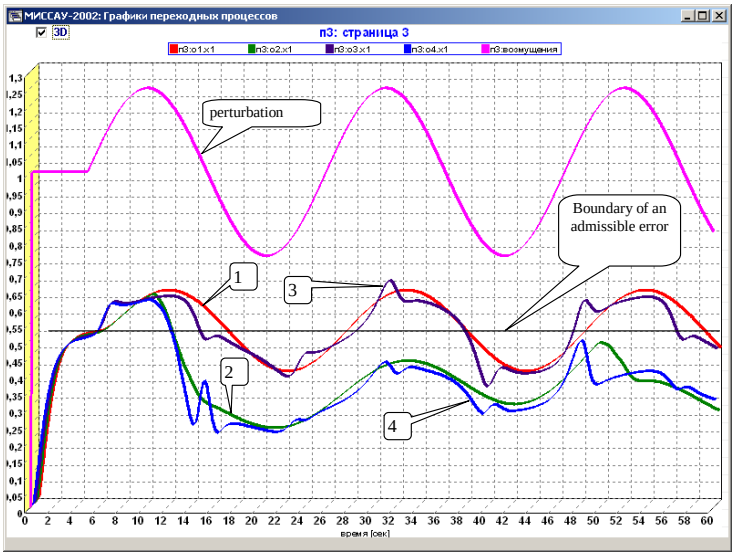

Fig. 4. Control of non-stationary plant

3. Conclusions

Tools of self-organizing ISSAC successfully compensate modifications of plant of control and an environment by means of use of new more exact law of control with the help of an intellectual system of automatic synthesis of the law of the control, based on (having) used neural computing organization based on planning artificial neural networks.

References

1. M. F. Stepanov. Intelligent self-organizing systems of automatic control - a triad "the theory of automatic control - information process engineering - an artificial intelligence" // Information process engineering. Moscow, 2001. № 11.
2. M. F. Stepanov. Automatic solution of the formalized tasks (problems) of the theory of automatic control. Saratov state technical university. Saratov, 2000.
3. M. F. Stepanov. Intelligent self-organizing automatic-control systems. Saratov state technical university. Saratov, 2002.
4. E. I. Efimov. The solvers of intellectual tasks. Science, Moscow, 1982.
5. G. Genzen. Researches of logical inferences // The mathematical theory of the logical inference. - Science. Moscow, 1967.
6. M. F. Stepanov. Problem solving of the theory of automatic control on the basis of planning artificial neural networks // Neurocomputers: design and applications, 2003. № 3-4. Pp. 27 – 44.

Chaotic Modeling and Simulation (CMSIM) 1: 75-81 , 2013

Chaotic Trend Possibility in the Gold Market

Nilufer Alan[†], Ilknur Kusbeyzi Aybar[*], O. Ozgur Aybar[†▪], Avadis S. Hacinliyan[†‡]

[†]Yeditepe University, Department of Information Systems and Technologies, Istanbul, Turkey
[‡]Yeditepe University, Department of Physics, Istanbul, Turkey
[*]Yeditepe University, Department of Computer Education and Instructional Technology, Istanbul, Turkey
[▪]Gebze Institute of Technology, Department of Mathematics, Kocaeli, Turkey

E-mail: oaybar@yeditepe.edu.tr
E-mail: ahacinliyan@yeditepe.edu.tr
E-mail: ikusbeyzi@yeditepe.edu.tr
E-mail: nlfr_alan@hotmail.com

Abstract: In this study, the International market gold prices over the last 31 years were analyzed for trends by five different methods, linear trend analysis, ARMA analysis, Rescaled range analysis, attractor reconstruction and maximal Lyapunov Exponent, detrended fluctuation analysis. Unfortunately not all methods give consistent results. The linear analysis reveals three regions with different trends. This is not supported by the rescaled range or detrended fluctuation analysis results. The maximal Lyapunov exponent calculation reveals chaotic behavior. The detrended fluctuation analysis reveals behavior close to brown noise. This is not corroborated by the rescaled range analysis, which indicates anti persistent behavior. The ARMA model implies first differencing that indicates a strong underlying linear trend.
Combining these results, one probable explanation is that the strong linear trend, (also corroborated by ARMA analysis) affects the rescaled range calculation, because of its dependence on extreme values. The detrended fluctuation analysis removes this trend and reveals brown noise. This is consistent with a maximal positive Lyapunov exponent. Hence, we have a linear trend plus brown noise and neither of these two effects is dominant.

Keywords: Dynamical systems, Gold Markets, Lyapunov exponents, Nonlinear Time Series Analysis.

1. Introduction

The goal of this paper is to provide a practical and accessible example for linear and nonlinear time series modeling. As a case study Gold prices in International markets between January 2, 1973 and March 31, 2011 is chosen. This field of study has been chosen for two main reasons. First, up-to-date data are available and it is free to download from international agencies. Second, Gold prices had

Received: 30 May 2012 / Accepted: 28 September 2012

ISSN 2241-0503

important effects on international monetary system which is explained in Section two. In section three, time series definition and its key features are explained such as trend, seasonality. In section four, one dimensional time series analysis of ARIMA and its components are explained. Section five is arranged for non linear time series analysis methods and linear and non linear time series analysis results are given. Gold has been the foundation of monetary systems for centuries. To illustrate the importance of Gold in monetary systems over the last century, one could start with the end of the British Gold Standard in 1914 to permit inflationary financing of World War I. As with all monetary inflations, it resulted in a buildup of debt as the public borrowed in order to spend money before loss of its purchasing power, with a view to repaying borrowings with currency after relative loss of its purchasing power. The end of monetary inflation in 1921 brought a return to stability for the UK and US. In 1929, collapse of overpriced equity markets resulted in deflation of consumer demand and depression. The cure for this came in 1935 by devaluing the paper money thus raising the paper money price of Gold. To restore stability and to avoid giving a message in favor of possible further inflation of the World Monetary Base, Foreign Exchange Rates were then fixed against Gold and the US Dollar was made convertible into Gold at a set price. The 1935 was ratified at Bretton Woods in 1944. Integrity of the US Dollar was guaranteed by the right of non-US Central Banks to convert their US Dollars to Gold if they feared that the purchasing power of the Dollar could be devalued through excess creation of money. However, in 1968 this arrangement was informally, and in 1971 formally, ended. The World Monetary system came off the US Gold Standard to permit inflationary financing which led directly to the Great Inflation of the 1970's and which, as usual, touched off a resurgence in debt. The 1970's Great Inflation of money ended in 1981, resulting in falling interest rates and strengthening bond and equity prices[1,2].

2. Nonlinear Time Series Analysis

Chaos occurs from the nonlinear evolution of systems. Chaotic dynamical systems are ubiquitous in nature such as the tornado, stock market, turbulence, and weather. Firstly, phase space reconstruction is necessary to understand that whether time series has chaotic behaviors or not[3,4,5].

The most striking feature of chaos is the limit of unpredictability of its future. This feature is usually called as the "sensitive dependence on initial conditions" or referring to the Lorenz models behavior, "butterfly effect. In this section, we will look at the details of nonlinear time series analysis by using mutual information, embedding dimension, maximal Lyapunov exponents, detrended fluctuation analysis and rescaled range analysis[6,7].

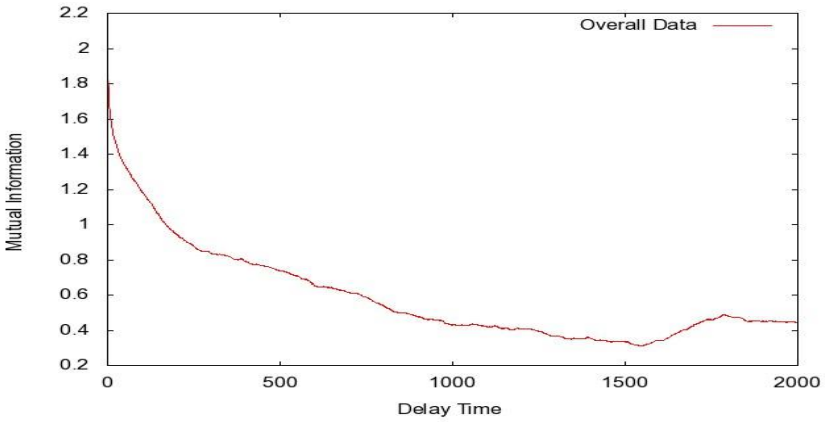

Fig. 1. Mutual Information of Overall Data

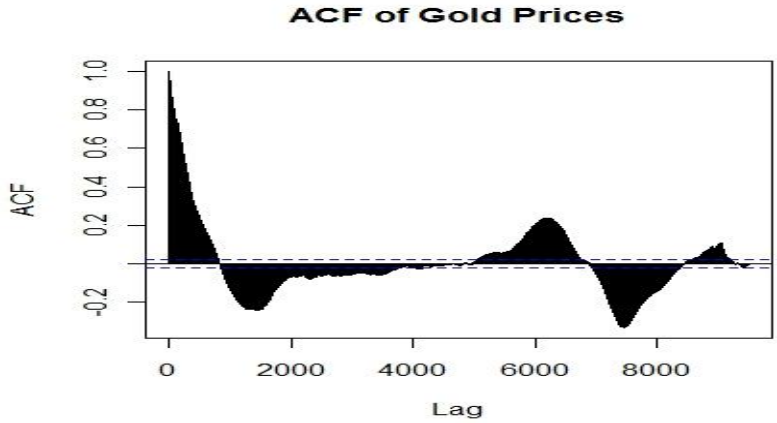

Fig. 2. Autocorrelation function of Gold prices (ACF vs. Lag)

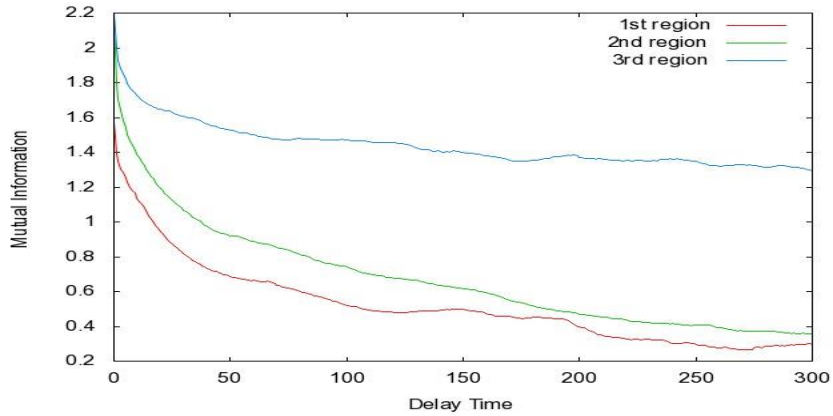

Fig. 3. Mutual Information of Each Region and Overall Data

In order to reconstruct phase space delay time should be found and to find delay time there are basically two methods which are mutual information and autocorrelation function.
As implied in Figure delay time of overall data is nearly 1500. Delay time is expected to be small as far as possible. As second method the calculation of autocorrelation functions were made with R Project statistics package program and also figures were drawn with this program. Figure shows autocorrelation ACF vs. lag and in this figure from first value to nearly 1000th value the ACF rapidly decreases and reaches zero. According to this figure delay time is nearly 1000. After that value it fluctuates between -0.2 and 0.2.The lags do not fall within their standard errors for this reason it is not white noise[8,9].
In each method delay times are too high to evaluate data as a whole. For this reason each region's mutual information was drawn one by one. Delay time chosen from average mutual information is more reliable because it also takes into account possible nonlinearity. For this reason as shown in Figure delay time of each region are calculated and plotted with mutual information method only. Moreover, they are found different from each other. First region's delay time is 100. For second delay time is calculated as 300 and for third region 60.

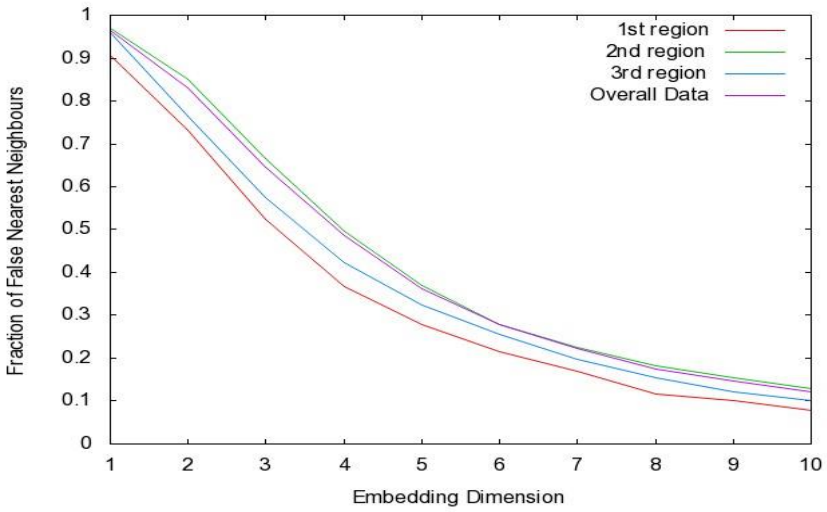

Fig. 4. FNN vs. Embedding Dimension of Each Region and Overall Data

After determining delay times embedding dimensions should be found. To find a satisfactory value for the embedding dimension, false nearest neighbors' method provides a good estimate. After finding delay time for overall data and for each region the fraction of false nearest neighbors are calculated. In Figure14 and the fraction of false nearest neighbors versus embedding dimension are plotted.
Although each regions delay times and trend behaviors' are different from each other, their embedding dimensions are nearly same. All regions embedding dimension graphs' are stabilizing after 8 dimensions.

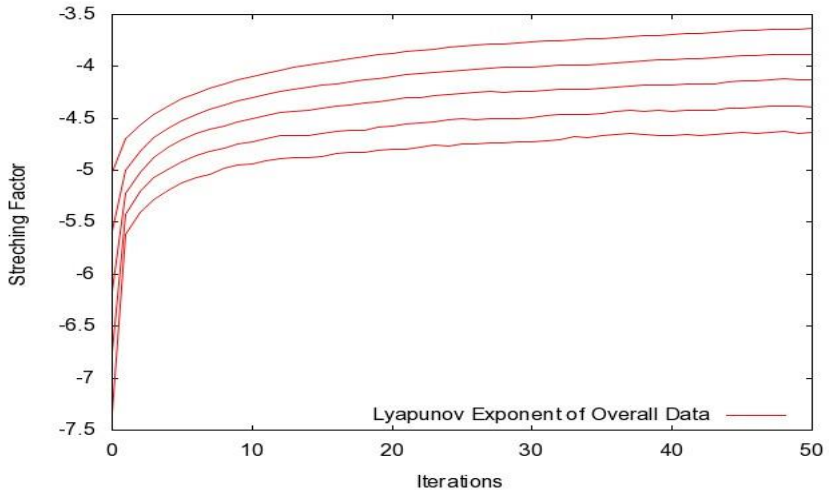

Fig. 6. Lyapunov exponents of Overall Data

The Lyapunov exponents are invariants of the dynamics. The maximal Lyapunov exponents are estimated with the use of TISEAN package and coded as the lyap_k routine. With the fit function of Gnuplot each region's slopes are calculated.1st region's Lyapunov exponent is 0.0308149, in 2nd is 0.0308149, in 3rd is 0.0255495 and Lyapunov exponent of overall data is 0.0175337.As a conclusion a positive Lyapunov exponent is indicated from Gold prices. All Lyapunov exponents are positive on this account they are not stable fixed points .Moreover, they are not equal to ∞. Consequently, they do not indicate random noise. However, they are positive and this shows that this time series is chaotic with a predictibility horizon of approximately 30.

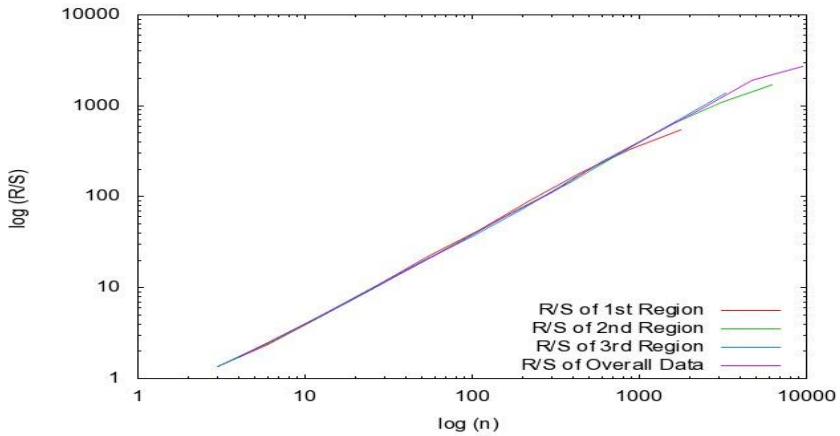

Fig. 7. R/S Analysis of Overall Data and Three Regions

In order to calculate Hurst exponent for each region and overall data Gnuplot and its fit function were used. For each region the Hurst exponent is calculated

and the exponents are found to be very close to each other. In the graph below, 1st region's R/S slope is 0.315411 and for 2nd region is 0.285779, for 3rd is 0.285779 and for overall data is 0.305127. If R/S slope was 0.5 it will be random series but it is positive and less than 0.5. Therefore, we consistently observe anti persistent behavior. There is a linear overall trend, as indicated by the first differencing plus noise. The positive Lyapunov exponent indicates that the noise is broadband.

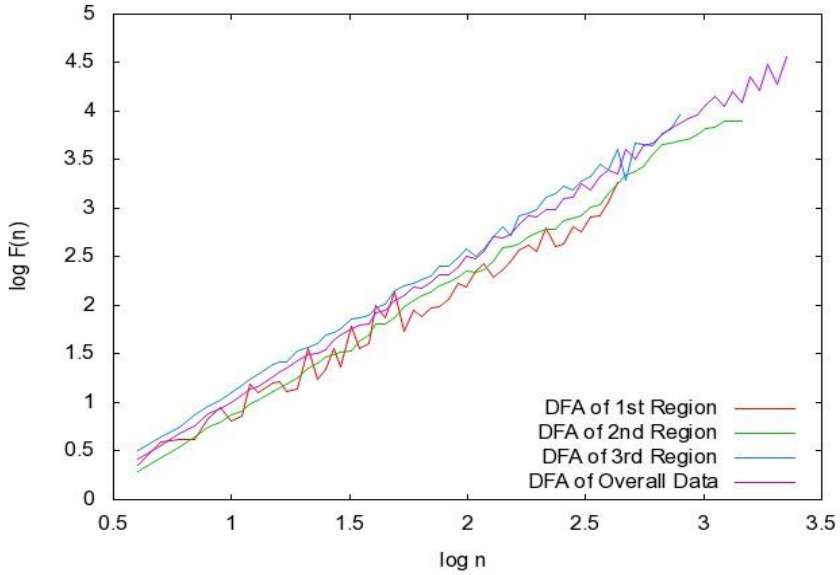

Fig. 8. Log n of Overall Data and Three Regions

As shown in Figure each regions' DFA behavior is very similar to the others .Slopes are calculated with Gnuplot' s fit function and they are found as that 1st region is 1.3136, for 2nd region is 1.45522, 3rd region is 1.46538 and for overall data is 1.4911. As explained in chapter 5 if the slope of DFA is 1.5 it is shows random walk model. All regions especially DFA slope of overall data is nearly 1.5 and it shows random walk model.

3. Conclusions

In this study, the International market gold prices over the last 31 years were analyzed for trends by five different methods, linear trend analysis, ARMA analysis, Rescaled range analysis, attractor reconstruction and maximal Lyapunov Exponent, Detrended fluctuation analysis. Unfortunately not all methods give consistent results. The linear analysis reveals three regions with different trends. This is not supported by the rescaled range or detrended fluctuation analysis results. The maximal Lyapunov exponent calculation reveals chaotic behavior. The detrended fluctuation analysis reveals behavior close to brown noise. This is not corroborated by the rescaled range analysis,

which indicates anti persistent behavior. The ARMA model implies first differencing.

Combining these results, one probable explanation is the strong linear trend, (also corroborated by ARMA analysis) which affects the rescaled range calculation, because of its dependence on extreme values. The detrended fluctuation analysis removes this trend and reveals brown noise. This is consistent with a maximal positive Lyapunov exponent. Hence, we have a linear trend plus brown noise and neither of these two effects is dominant[7,8,9].

References

1. S. Boker. Linear and Nonlinear Dynamical Systems Data Analytic Techniques and an Application to Development Data, A Dissertation Presented to the Graduate Faculty of the University of Virginia in Candidacy f or the Degree of Doctor of Philosophy, 39, 1996.
2. M. Bolgorian, Z. Gharlı. A Multifractal Detrended Fluctuation Analysis Of Gold Price Fluctuations , *Acta Physica Polonica B* , vol. 42, 2011.
3. K. Clayton, F. Vaio. Basic Concepts in Nonlinear Dynamics and Chaos, A Workshop presentation at Society of Chaos Theory in Psychology and the Life Sciences meeting, 1997.
4. C. H. Skiadas. Two simple models for the early and middle stage prediction of innovation diffusion. *IEEE Trans Eng Manage* 34:79–84, 1987.
5. C. H. Skiadas and C. Skiadas. *Chaotic Modeling and Simulation: Analysis of Chaotic Models, Attractors and Forms*, Taylor and Francis/CRC, London, 2009.
6. P. Franses, *Time Series Models for Business and Economic Forecasting*, Cambridge University Press, 9, 1998.
7. H. Kantz, T. Schreiber, *Nonlinear Time Series Analysis*, Cambridge University Press, 2nd Edition, 86, 2004.
8. D. Kugiumtzis, B. Lillekjendlie, N. Christophersen, Chaotic time series: Estimation of invariant properies in state space, *Modeling, Identification, and Control*, vol. 15, 4: 205-224, 1994.
9. O. Cakar, O. O. Aybar, A. S. Hacinliyan, I. Kusbeyzi, Chaoticity in the Time Evolution of Foreign Currency Exchange Rates in Turkey, *CHAOS 2010 3rd Chaotic Modeling and Simulation International Conference*, Greece (2010).